University of Alberta

Opto-biochips for Microcytometry

by

Sanket Goel ©

A thesis submitted to the Faculty of Graduate Studies and Research in partial fulfillment of the requirements for the degree of *Doctor of Philosophy*

Department of Electrical and Computer Engineering

Edmonton, Alberta
Spring 2006

Library and
Archives Canada

Published Heritage
Branch

395 Wellington Street
Ottawa ON K1A 0N4
Canada

Bibliothèque et
Archives Canada

Direction du
Patrimoine de l'édition

395, rue Wellington
Ottawa ON K1A 0N4
Canada

Your file Votre référence
ISBN: 0-494-13978-1
Our file Notre référence
ISBN: 0-494-13978-1

NOTICE:
The author has granted a non-exclusive license allowing Library and Archives Canada to reproduce, publish, archive, preserve, conserve, communicate to the public by telecommunication or on the Internet, loan, distribute and sell theses worldwide, for commercial or non-commercial purposes, in microform, paper, electronic and/or any other formats.

The author retains copyright ownership and moral rights in this thesis. Neither the thesis nor substantial extracts from it may be printed or otherwise reproduced without the author's permission.

AVIS:
L'auteur a accordé une licence non exclusive permettant à la Bibliothèque et Archives Canada de reproduire, publier, archiver, sauvegarder, conserver, transmettre au public par télécommunication ou par l'Internet, prêter, distribuer et vendre des thèses partout dans le monde, à des fins commerciales ou autres, sur support microforme, papier, électronique et/ou autres formats.

L'auteur conserve la propriété du droit d'auteur et des droits moraux qui protège cette thèse. Ni la thèse ni des extraits substantiels de celle-ci ne doivent être imprimés ou autrement reproduits sans son autorisation.

In compliance with the Canadian Privacy Act some supporting forms may have been removed from this thesis.

While these forms may be included in the document page count, their removal does not represent any loss of content from the thesis.

Conformément à la loi canadienne sur la protection de la vie privée, quelques formulaires secondaires ont été enlevés de cette thèse.

Bien que ces formulaires aient inclus dans la pagination, il n'y aura aucun contenu manquant.

Canada

प्रिय बहिन प्रतीक[*]
को
सादर सहृदय समर्पित

Dedicated to
lovely sister Prateek[*]
with heartfelt respect and ineffable affection

---

[*] Author's elder sister, Prateek passed away at the age of 15 in 1992.

Abstract

Microscale fluorescence activated cell-sorting (μFACS) by switching of continuous flows in microsystems is a new technology being developed to identify and separate cells. Different elements of the μFACS, fabrication of opto-biochips, particle detection and velocity measurement, and flow switching, are studied in the present work.

Different techniques to fabricate biochips are presented. Masters with inverse patterns of biochips were fabricated by direct laser-writing, and by lithography and dry etching. Biochips were fabricated by casting polydimethylsiloxane (PDMS) on the masters. In a different approach, biochips with integrated waveguides and microchannels were fabricated photolithographically on glass substrates using a negative photoresist, SU-8. The system includes multimode waveguides with combiners and splitters for utilizing lasers of different wavelengths for the identification of different particle types.

Detection of particles in commercial biochips and micropipettes using a custom plastic optical fiber launch-and-detect tip is described. The velocity of the microparticles has been measured by the spatial response of the tip and the dynamic response of the moving microparticles. In a glass biochip with etched microchannels and ion-exchange waveguides, the double peak signal from moving microparticles at the intersection of microchannel and waveguide was used to determine the velocity of the microparticles in an electroosmotic flow. Microparticle flow switching has been realized in PDMS biochips.

In the SU-8 opto-biochips, two excitation waveguides carrying two different wavelengths intersect the microchannel at two points separated by a known distance.

One large output waveguide carry fluorescence signals to a single filtered detector. The loss in SU-8 waveguides was measured for two different wavelengths. The velocities of the microparticles were determined by the captured fluorescence from the double peak. Simulations based on beam propagation method were used to predict the performance of the SU-8 waveguides and the intensity at the two intersections has been compared with the experimental results.

Acknowledgements

Reflecting back, the last four years have been a very fulfilling experience; in terms of what I have learnt, the friends I have made and the fun I have had. Wheatear it was playing Badminton, driving to Canadian Rockies, working in lab, cooking in the evening or even having chat over a cup of coffee, this has been the best period of my life so far. In the end, the doctoral thesis is supposed to signify the achievements of a person during an important phase in his career. But it would be presumptuous that my thesis came together without the motivation, support and assistance of numerous individuals in my life.

First and foremost I would like to express my utmost gratitude to my advisor, Professor Jim McMullin for his constant support, encouragement, constructive criticism and immensely valuable suggestions throughout my graduate studies. This thesis would not have seen the light of the day without his invaluable ideas and creative intellectual support. My association with him has also taught me to appreciate the value of persistent tolerance in the development of healthy scientific environment.

I take this opportunity to thank my committee members, Professors Ray DeCorby, Steven Evoy, Jed Harrison and Clifton Johnston for their helpful suggestions, advice and generous contributions of their time. I owe a heartfelt thanks to Professors Robert Fedosejevs and Ying Tsui for help and insightful discussions during the course work and research. My sincere thanks to Dr. Gunter and Marli Schmidt-Weinmar and Angeela Antoniu for their consistent encouragement and tirelessly listening to my ideas and suggestions. I am indebted to my colleagues from Micro-Optical Systems lab and NanoFab, Hong Qiao, Hue Nguyen, Nan Xie, Dean Spicer, Danny Pulikkaseril, Franćois Kuate, and Hooman Hosseinkhannazer for generously helping me with my research.

I would like to acknowledge the Canadian Institute for Photonic Innovations (CIPI), the

Natural Science and Engineering Research Council of Canada (NSERC), and Micralyne Inc. of Edmonton for the financial support. My sincere thanks to the staff of NanoFab and Machine Shop for their contribution to this thesis.

I would like to acknowledge friends from local Indian community, Indian Students Association (ISA) and Society for the promotion of Indian Classical Music and Culture amongst Youths (SPIC MACAY). Due to my association with these organizations, I have been privileged to be a part of the fraternity and the city of Edmonton has always been a home away from home.

I am indebted to Dr. Prabhat Dwivedi for his kind support as an elder brother. Our unending and invaluable personal and academic discussion over coffee, lunch and walk towards Saskatchewan river will always be in my memories. I am grateful for the friendship of Shaine Joseph, Aravind V., Arvind Prasad, Rohit Malik, Ashish George, Sushil Rana, Mahesh Pai, Sunil Bandaru, Naveen Srivastav, Biswaroop Palit, Yogesh Godwal and Jayson for their support both on personal and professional levels.

As all good acknowledgements go, I must especially thank my parents, Mrs. Pushplata Goel and Dr. Satish Goel. I have been blessed with unlimited support and encouragement over the years. There is no way I could have gotten where I am, professionally or personally, without my parents pushing and prodding and most of all reminding me that, “Everyone worships the rising Sun”. I would like to thank everyone in my joint family, especially my uncle Mr. Girish Goel, for having confidence in me and being proud at what I was at each and every moment of my life. I gratefully acknowledge my sister and my best friend Anjali for always standing besides me and her invaluable support and advice.

Finally the last mention goes to the most important person in my life after my PhD, my fiancée Pooja. I again thank my family to give me this most precious gift of lifetime. Although we have met for just two weeks, her support and dedication to seeing me achieve this goal has been ineffable. I can only begin to thank Pooja for providing me the most beautiful days of my life. Starting next month I look forward to a lifetime of growing together with her.

Contents

1 Introduction 1

1.1 Flow Cytometry (FCM) 1

1.1.1 Fluorescence Activated Cell-Sorter (FACS) 2

1.1.2 Principle of the FACS in the Present Work 3

1.2 Microscale Fluorescence Activated Cell-Sorting (μFACS) 4

1.3 Current State of the Research on Opto-Biochips 6

1.3.1 Biochips 6

1.3.2 Optical Integration in Biochips 7

1.3.3 Previous Research in Micro-Optical Systems Lab 9

1.4 Scope and Goals of the Thesis 12

2 General Principles of Microfluidics and Integrated Optics **13**

2.1 Microfluidics Overview 13

2.1.1 Microfluidics Flow Properties 13

2.1.2 Flow Velocity in Laminar Flow 17

2.1.3 Comparing Pressure Driven Flow and Electroosmotic Flow 21

2.2 Integrated Optics Overview 23

2.2.1 Waveguiding Principle 23

2.2.2 Structure of a Waveguide 24

2.2.3 Requirement for Integrated Optics 25

3 Fabrication Techniques for OptoBiochips **27**

3.1 Material Selection Criteria 27

3.2 Different Fabrication Approaches in the Present Research. 28

3.2.1 Direct Device Fabrication by Laser-Writing 29
3.2.2 Master Fabrication 33
3.2.3 Device Fabrication Using Polymers 36
3.2.4 Direct Device Fabrication on SU-8 39

4 Optical Detection I - Microcapillary, Ion-exchanged and PDMS biochips 45
4.1 Optical Detection in Glass Capillary by Plastic Optical Fiber 46
4.1.1 Launch and Detect Tip using Plastic Optical Fiber 46
4.1.2 Application to Velocity Measurement of Microparticles 48
4.2 Microparticle Detection in Ion-Exchanged Opto-Biochips 51
4.2.1 Fluorescence from Dye in the Microchannel 51
4.2.2 Anomalous Etching of the Ion-Exchanged Glass 52
4.2.3 Electroosmotic flow, Microparticle Detection and Velocity Measurement 54
4.3 PDMS Biochips 60
4.3.1 Electroosmotic Flow 61
4.3.2 Electroosmotic Flow Switching 67

5 Optical Detection II - SU-8 Opto-Biochips 69
5.1 Design Motivation 70
5.2 Propagation Loss Measurements 72
5.2.1 Loss Measurement at 635 nm 74
5.2.2 Loss Measurement at 530 nm 75
5.3 Optical Detection and Velocity Measurement of Microparticles 77
5.3.1 Detection with Plastic Fiber Below the Intersection 78
5.3.2 Collecting Fluorescence from the SU-8 Output Waveguide 82
5.4 BPM Simulation 88
5.4.1 Flux Flow 90

6 Conclusion 96
6.1 Summary of the Results 96

6.2 Recommendations for Future Work 98

Bibliography **101**

A Material Properties **113**

B Procedure for Fabricating Master by Lithography (Positive photoresist) **115**

C PDMS Casting and Bonding **119**

D Procedure for Fabricating Biochips by Lithography (SU-8, Negative Photoresist) **122**

List of Tables

2.1 List of physical parameters affecting electroosmotic and pressure-driven flows 22

5.1 Velocity measurement in SU-8 biochips with the PMT fiber under the intersection points. The distance between the intersection points is 200 μm. 82

5.2 Velocity measurement in SU-8 biochips. The PMT fiber is butt-coupled with the output waveguide. The distance between the intersection points is 600 μm. 87

A.1 Properties of different materials used in the present work 114

List of Figures

1.1 *Schematic diagrams of (a) Flow cytometry, and (b) Fluorescence-activated cell-sorting in flow cytometry [1].* 2
1.2 *Schematic diagram of cell-sorting experiment.* 3
1.3 *Different components of a flow cytometer.* 5
1.4 *Two different biochips fabricated on glass and PDMS.* 7
1.5 *A commercially available microfluidic toolkit sold by Micralyne Inc. of Edmonton, Alberta.* 8
1.6 *Laser-written biochip.* 9
1.7 *Biochip with ion-exchanged waveguides.* 10
1.8 *Two-level biochip with integrated optics* 11

2.1 *Pressure driven flow and electroosmotic flow in a microchannel* 14
2.2 *A schematic of the effect of hydrodynamic pressure.* 18
2.3 *Dimensionless velocity profile due to pressure driven flow* 19
2.4 *Dimensions of the microchannel with one particles inside it.* 19
2.5 *Dimensionless velocity profile due to electroosmotic flow for different* κh *values.* 20
2.6 *Snell's law and Total Internal Reflection.* 24
2.7 *Light propagation in a waveguide due to total internal reflection.* 25

3.1 *Different approaches to fabricate biochips used in the present research.* 29
3.2 *Schematic of the Laser writing setup* 30
3.3 *Screen-shot of the Labview interface of motor controlled board.* 31

3.4 *Different parts of biochip with Y-shape microchannel fabricated by NOA. The pictures A, B and C are the parts joining the microchannel with three reservoirs respectively. The picture D is the Y-shape part of the microchannel and picture E shows the NOA waveguides joining with the walls of the microchannel.* 32

3.5 *A NOA chip with microchannels and waveguides (Figure 3.4 (E)). NOA ridges work as the core of the waveguide and the walls of the microchannel. Light is propagating through the waveguide and shining light at a point on the microchannel. The white spots are due to scattered light from imperfections in the walls.* 32

3.6 *Different designed generated on glass slide by laser writing process, work as masters.* 34

3.7 *(a) Depth measurement of the microchannel by the contact profilometer (this case shows the depth of left T shown in the mask layout in Figure B.1), and (b): SEM result of the side view of a cross on wafer.* 35

3.8 *(a) Optical Profilometer picture to find the height of the microchannel (53.11 μm), and (b) Optical profilometer pictures to find the roughness of the top surface of the microchannel.* 36

3.9 *Two PDMS chip with microchannels and reservoirs. The master was fabricated by the direct laser-writing.* 37

3.10 *Schematic of the Hot Embossing process after fabricating the master.* 38

3.11 *(a) The master after hot embossing is performed. In this case, the silicon master was bonded on pyrex by anodic bonding, (b) PMMA plate after hot embossing is performed. In this case, the silicon master was bonded on pyrex by anodic bonding before hot embossing. Several parts of the silicon masters were remaining on the plate.* 39

3.12 *Different chip designs on the mask (a) Y-shape channel and intersecting waveguides, (b) straight channel and intersecting waveguides, (c) for continuous electroosmotic flow, and (d) t-shape channel and intersecting waveguides.* 41

3.13 *Different parts of Biochip fabricated by SU-8 on glass as described in the text below and represented on the chip in Figure 3.12.* 42

3.14 *Picture showing the scan taken by a contact profilometer on glass substrate with SU-8.* 43

3.15 *Picture showing the scan taken by a contact profilometer of two input waveguides in SU-8 with air cladding.* 43

4.1 *(a) Schematic of the launch-and-detect plastic optical fibers head, and (b) Incoming and outgoing light from a launch-and-detect tip.* 46

4.2 *Particle inside a biochip.* 47

4.3 *Spatial response of the POF with stationary particle in the biochip.* 48

4.4 *Schematic of experiment to detect microparticles in flow through a micropipette.* 49

4.5 *Full PMT scan over 30 seconds for moving fluorescent microparticles in the micropipette. Each value shown is the average of 200 raw samples taken at 10 000 samples per second. There are 16 particles with various velocities observed in this window.* 50

4.6 *Detail of the different particles (not on scale).* 50

4.7 *Propagation of light through the waveguide splitter and PMT signal scattered from microchannel.* 52

4.8 *(a) SEM image before bonding of the glass cover plate, and (b) Two-dimensional beam propagation simulation showing the split of waveguide light into two distinct beams in the microchannel.* 53

4.9 *Schematic of experiment to move and detect microparticles by electroosmotic flow inside biochip* 54

4.10 *18 frames showing movement of one fluorescent microsphere in a electroosmotic flow at 50V. Frames in this picture are 1/3 s apart. Laser light from the waveguide on the left illuminates the microchannel. The fluorescence is brightest in frames 6 and 14.* 56

4.11 *Detection of two particles in two direction at different voltages passing through microchannel-waveguide intersection.* 57

4.12 *Scan through the PMT at 200V showing movement of two particles.* 58

4.13 *Graphs showing the variation of two particles velocity with applied voltage (a) by video frames (b) by PMT scan.* 59

4.14 *Graph showing the variation of velocity with applied voltage. Here, velocity is the average of the velocities of two particles measured by the two different methods.* 59

4.15 *Experimental setup for observing the electroosmotic flow (between reservoirs A and B) in the PDMS biochip.* 61

4.16 *24 frames showing movement of one fluorescent microsphere in a electroosmotic flow at 200 V. Each frame is 1/3 s apart. The particle position is indicated by a circle.* 62

4.17 *15 frames showing movement of one fluorescent microsphere in a electroosmotic flow at 500 V. Each frame is 1/3 s apart. The particle position is indicated by a circle.* 63

4.18 *12 frames showing movement of one fluorescent microsphere in a electroosmotic flow at 1000 V. Each frame is 1/3 s apart. The particle position is indicated by a circle.* 64

4.19 *Different frames showing movement of one fluorescent microsphere in a electroosmotic flow for different voltages around the corner. The bead position is indicated by a circle.* 65

4.20 *Graph showing the variation of velocity with applied voltage in PDMS biochip.* 66

4.21 *Experimental setup for observing the switching of the electroosmotic flow in PDMS biochip.* 67

4.22 *9 frames showing the switching of fluorescent microsphere in a electroosmotic flow at 500 V. Each frame is 2 s apart. The bead position is indicated by a circle.* 68

5.1 *Two SU-8 waveguide designs.* 71

5.2 *Dimensions of different points of the waveguide microchannel combination. The white region is the core (SU-8) and the dark region is the cladding of the waveguides. (a) Start region, (b) Intersection region, where the two waveguides shine light on two points of the microchannel, (c) Middle region, where the two waveguides join together and again split into two waveguides.* 72

5.3 *Schematic diagram of the experimental set-up to measure loss in SU-8 biochip.* 73

5.4 *Plot of the measurement of the scattered light at 635 nm from different points of the SU-8 waveguide. Two plots correspond to the launching of input light from two waveguide entrances. Different points on this graph are discussed in Figure 5.5* 73

5.5 *Measurement of loss at 635 nm from between points C, D, H and I of the two SU-8 waveguides. The loss was found to be 3.1 dB/cm and 2.5 dB/cm corresponding to the launching of input light from two waveguides.* 75

5.6 *Plot of the measurement of scattered light at 530 nm from different points of SU-8 waveguide. Two plots correspond to the launching of input light from two waveguide entrances. Different points on this graph are discussed in Figure 5.7* 76

5.7 *Measurement of loss at 530 nm from between points C, D, H and I of the two SU-8 waveguides. The loss was found to be 5.2 dB/cm and 6.1 dB/cm corresponding to the launching of input light from two waveguides.* 76

5.8 *The schematic of the experimental setup used for fluorescence detection of microparticles in SU-8 biochip. The syringe tip is used to control the flow of microparticles.* 78

5.9 *An image of the experimental set-up used for optical detection of microparticles in SU-8 biochip. The laser light is launched from the multimode fiber connecter at the far side and the PMT fiber is underneath the chip.* 79

5.10 *12 frames showing movement of one fluorescent microsphere in a pressure-driven flow. The frames in this picture are 1/6 s apart. The bead position is indicated by a circle.* 80

5.11 *(a) Plot of 10, 000 points over 100 s PMT signal, and (b) PMT response (mV) from 6 particles as a function of the time (seconds).* 81

5.12 *The picture of the experimental setup as shown in Figure 5.8(b)* 83

5.13 *Plot of 10, 000 points over 100 s PMT signal. There are more than 60 peaks within the span of 100 s, indicating the movement of more than 30 particles in 100 s. Eight particles represented here are shown in Figure 5.14.* 84

5.14 *The PMT scan between 7th and 49th second showing the movement of 8 particles.* 85

5.15 *Details of the PMT signal corresponding to eight particles as shown in Figure 5.14.* 86

5.16 *Details of the PMT signal corresponding to four particles. From the relative size of the plots as described in Figure 5.15, the peaks related to these four particles are recognized.* 87

5.17 *Dimension of a structure with waveguide and microchannel as shown in Figure 5.1 (A). All the numbers are in micrometers. The core of the waveguide is of index 1.59, the index of the the microchannel is 1.33 and remaining part is considered with index 1.5 due to the limitation in BPM simulations.* 89

5.18 *Laser beam propagating into the waveguide consisting of straight sections and S-bends.* 91

5.19 *Laser beam propagating into the waveguide consisting of straight sections and S-bends from a different angle.* 92

5.20 *Variation of the power of laser beam in the microchannel. The graphs show that the power at the two intersections is distributed almost equally even after changing the entry point of the incident laser light.* 93

5.21 *Picture of the two waveguide-microchannel intersections when the entry point of the incident light is changed.* 93

5.22 *Intensity profile using inside a microchannel as shown in Figure 5.21, all values are in μm.* 94

6.1 *A schematic of a proposed device after laser-writing. The white part is air where laser-writing will takes place and rest part will have photoresist.* . . 99

B.1 *(a) LEdit design to make the mask, and (b) actual mask after developing.* . . 116

B.2 *Process steps for fabricating silicon master with positive photoresist and deep reactive-ion etching.* 118

D.1 *Process steps involved to fabricate opto-biochips with SU-8.* 123

List of Symbols

^{o}C	degree Celsius
ε	permittivity
ε_r	relative permittivity
η	viscosity
κ	inverse Debye length
μ_r	relative susceptibility
ϕ, ψ	electric potential
ρ_f	charge density
ζ	zeta potential
c	speed of light
C	Coulomb
D	laser spot-size
E	electric field
g	Gravitational acceleration
h	microchannel half-width
k_B	Boltzmann constant
L	length of the microchannel
M	molarity
N_A	Avagardo's number
n	index of refraction
n_∞	ionic number concentration
z	valance
p_x	pressure-gradient
R_e	Reynolds number

List of Abbreviations

μTAS	micro-total-analysis-system
μFACS	microscale fluorescence activated cell-sorting
BOE	buffered-oxide etching
BPM	beam-propagation method
CCD	charged coupled device
DAQ	data acquisition
dB	decibel
DI	de-ionized
EDL	electric double layer
EOF	electroosmotic flow
FACS	fluorescence activated cell-sorter
FCM	flow cytometry
ICPRIE	inductance-coupled reactive-ion etching
IPA	isopropyl alcohol
LOC	lab-on-a-chip
MEMS	micro-electro-mechanical system
MOS	micro-optical system
MST	microsystem technology
min	minute
mm	millimeter
mV	millivolt
NanoFab	University of Alberta, Micromachining and Nanofabrication Facility
NOA	Norland optical adhesive

nm	nanometer
PC	polycarbonate
PDF	pressure-driven flow
PDMS	polydimethylsiloxane
PETG	poly-ethylene ere-phthalate glycol
PMMA	polymethymethacrylate
PMT	photomultiplier tube
POF	plastic optical fiber
PP	polypropylene
RMS	room-mean square
SEM	scanning electron microscope
UV	ultraviolet
V	volt
VI	virtual instrument
WG	waveguide

Chapter 1

Introduction

1.1 Flow Cytometry (FCM)

Cells are the basic structural and functional unit of all living organisms, sometimes called the “building blocks of life.” Flow cytometry (FCM) is a technology that simultaneously measures and analyzes the properties of cells or, in general, any specimen that needs to be analyzed. The basic principle of flow cytometry is to individually detect the optical signal from each moving particle in a fluid stream as it moves past a source of light. The optical signal is in the form of fluorescence, which is the absorption of a photon of short wavelength and subsequent emission of a photon of longer wavelength [1, 2]. The first flow cytometer, able to analyze single cells was reported in 1965 [3], when the cells were analyzed at a rate of 500 per second. The commercialization of the flow cytometers was started in the 1980s after the availability of fast computers [4]. At present, flow cytometers can analyze samples at a very high rate (up to 100,000 cells per second [5]).

Figure 1.1(a) shows a basic structure of a typical flow cytometer where the sample detection takes place [1]. The three main units of a flow cytometer are the fluidics system, the optical system, and the electronics system. The fluidics system consists of a flow chamber where the cells are injected into the core of a sheath flow. The optics system has a laser source and a detector. The cells capture the light from the laser and the detector collects the fluorescence or scattered light. The electronics system consists of a detector and data-analysis system. The detector converts the optical signal to an electronic signal, which is processed by the computer using data-analysis system.

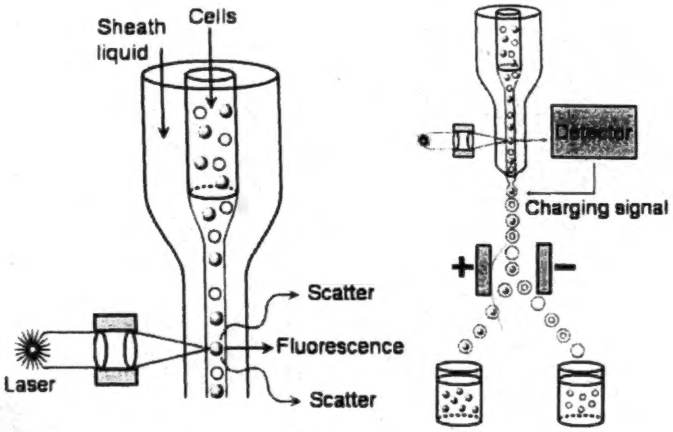

(a) (b)

Figure 1.1: *Schematic diagrams of (a) Flow cytometry, and (b) Fluorescence-activated cell-sorting in flow cytometry [1].*

Comprehensive reviews on current status of flow cytometry have been presented in [1, 5, 6]. Some of the applications of flow cytometry are in the field of cell biology [7], disease diagnostics [8], environment monitoring [9] and genetics [10].

1.1.1 Fluorescence Activated Cell-Sorter (FACS)

In most of the flow cytometer applications, the flow of the particles is directed towards the exit of the flow chamber. Cell-sorting in flow cytometry allows the separation and isolation of the cells of interest from mixed population at the exit of the flow chamber for further analysis [1, 5].

Figure 1.1(b) shows a jet-in-air system, which is the most commonly used method for cell-sorting. In this system, the nozzle assembly vibrates at a high frequency and the liquid stream of cells is converted into droplets containing single cells. As the droplet intercepts the laser beam, the detector collects the fluorescence signal from the cell and identifies it. Then, the droplets are electrically charged accordingly, and deflected by a strong electric field into the collecting containers. Using this method, a commercial cell-sorter at present can sort up to 25,000 cells per second [11], compared to the earlier systems developed in

1977 (500 cells per seconds) [2], and in 1985 (20,000 cells per seconds) [12].

1.1.2 Principle of the FACS in the Present Work

As discussed above, the commercial cell-sorters are widely used for different cell-sorting applications [11] and have a very high rate. However, they are still far away from the reach of the common user because they are very costly ($250,000 [13]) and they work on a very delicate mechanism. Some of the limitations include perturbations in droplet formation and difficulty in generating identically charged droplets [13]. Different methods have been used to achieve FACS during the past several years [14].

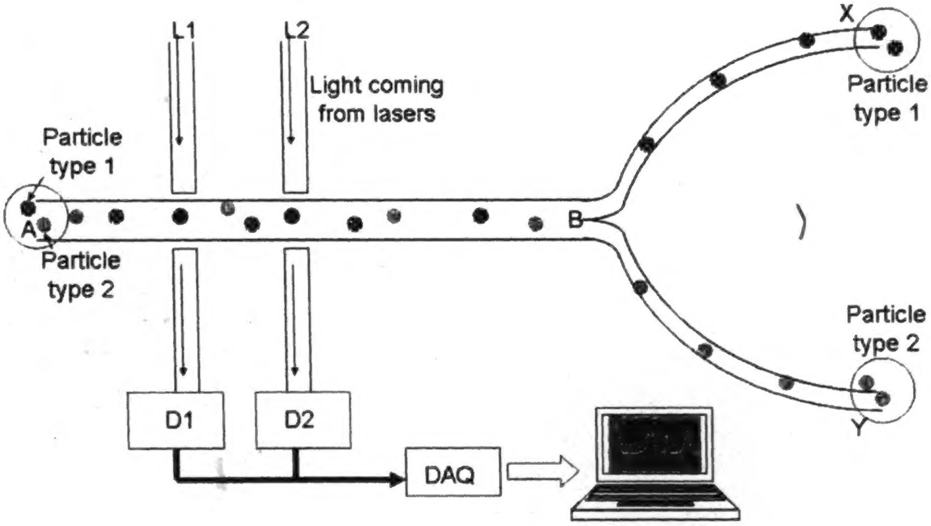

Figure 1.2: *Schematic diagram of cell-sorting experiment.*

Contrary to the method of electronically deflecting charged droplets containing single cells, an alternate method based on switching continuous flow by changing the direction of the flow electro-mechanically can be used as shown schematically in Figure 1.2. In this method, first the cells are recognized and then their flow is switched at the moment they arrive at the switching point B.

If two types of cells must be sorted, the fluidic system should have two output reservoirs (X and Y) to collect different kinds of cells. As the identification of the cells is required, the cytometer may need to allow two different wavelengths of light to be delivered to the fluidics system. After the cytometer identifies the cell of interest, they can be separated using an upgraded electronics system to initiate sorting decisions and switch the flow accordingly.

Two different types of cells flowing in the fluidics chamber are shown in the Figure 1.2. Light from two lasers, L1 and L2 illuminates the two points in the chamber and the two detectors D1 and D2, capture the fluorescence from the cells. These detectors D1 and D2 have filters corresponding to the spectra of the two different cells.

When a cell of type 1 arrives at the intersection of L1 and the chamber, the detector D1 gives a signal to the data-acquisition unit (DAQ) and a computer records the exact time when the particle arrives at the intersection. If the velocity of this cell can be determined, the time t_1 taken by this cell to reach the point B can be calculated. At point B the flow of this cell can be switched towards reservoirs X using switching electronics. In a similar way, the detector D2 captures the fluorescence from the second type of cells. By measuring their velocity, the time t_2 taken by one of these cells to reach the point B can be found and they can be deflected to move to output reservoir Y. This way, each type of cell can be collected at their respective output reservoir. In principle, many different types of cells could be collected at many different reservoirs using this method.

1.2 Microscale Fluorescence Activated Cell-Sorting (μFACS)

In contrast with FACS, a μFACS has number of advantages over conventional FACS. μFACS are portable in size, more economical, and do not require rigorous training for sample tagging and instrument operation [13, 15]. One of the major advantages to realizing a μFACS is the possibility of integrating the different parts on one platform. Some work has already been carried out to achieve μFACS and is discussed in references [13, 16].

A schematic of a micro-flow cytometer system having different operating units is described in Figure 1.3(a). In place of a flow chamber in conventional flow cytometers (Figure 1.1(b)), the fluidics part consists of a Y-shaped microchannel to sort two types of microparticles. Figure 1.3(b) describes the integration of both the fluidic system and

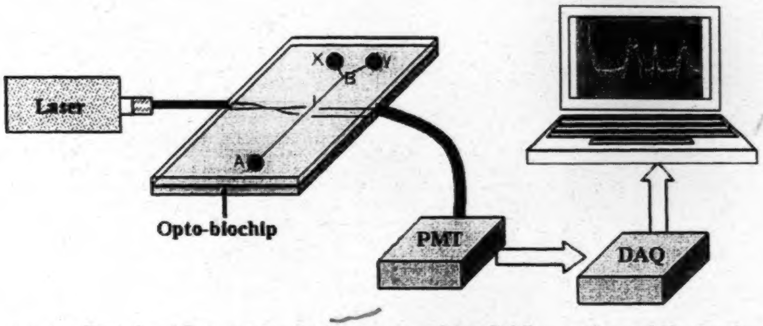

(a) A schematic of flow cytometer system comprising fluidics, optics and electronics.

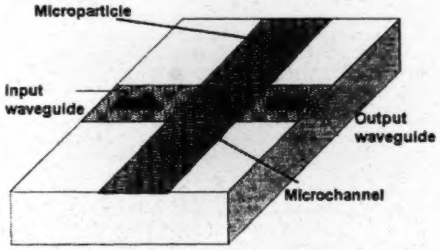

(b)
Flow of moving microparticles in an opto-biochip. The output waveguide captures fluorescence from microparticles illuminated by incoming light.

Figure 1.3: *Different components of a flow cytometer.*

the optical system on the same platform [17]. The intersecting input waveguides guide the laser light to the particles at the intersection, I, and the output waveguide captures the fluorescence from the microparticle, which is collected by the photomultiplier tube (PMT). If the input waveguide splits into two as indicated in Figure 1.3(a), then light of two different wavelengths can be delivered to two points in the microchannel. The output waveguide can capture the signals from both these points at the same time.

We refer to such a system as a biochip with integrated optics or an *opto-biochip*. The principle of cell-sorting is similar to the one described in Section 1.1.2. From the above discussion, some of the important elements to demonstrate the μFACS are listed below:

- An opto-biochip having microchannels and waveguides
- Photomultiplier tube (PMT) detection system

- Mechanisms to observe the flow in the microchannel
- Velocity measurement
- Software to collect data recorded by the PMT
- Flow switching

A review of opto-biochips and current state of the ongoing research is discussed in the following section.

1.3 Current State of the Research on Opto-Biochips

A microsystem is defined as an "intelligent miniaturized system comprising sensing, processing and/or actuating functions" [18]. MicroSystem Technology (MST), the science of producing miniaturized systems, allows for device miniaturization and at the same time, better performance, lower cost and higher reliability. Some of the different research fields in Microsystems technologies are Micro-Electro-Mechanical Systems (MEMS) [19, 20], Very Large Scale Integrated (VLSI) circuits [21], Opto-Electronics [22, 23] and Microfluidics [24, 25]. MST's have most important and promising applications in the area of Medicine [26] and Biology [27].

Research to combine many necessary components and functionality on a small chip leads to integrated microsystems [28]. Micro total analysis systems (μTAS) [29, 30], originated in 1983 [31], are the combination of MEMS and fluidic microsystems [19]. The development of μTAS was continued by Manz and Harrison in the 1990s [32, 33] by scaling down for better separation performance and analytical ease [29, 30]. Later, it was realized that these devices can be used in different applications ranging from medical and chemical analysis [34, 35] to astrophysics [36].

1.3.1 Biochips

One type of μTAS are called "labs-on-a-chip (LOC)" or "biochips" [37]. Biochip is a device fabricated on different materials (glass [38], silicon [39] and polymers [40]) with embedded micron-sized microchannels. Research of microfluidic biochips has accelerated the last decade driving due to their ever-increasing applications in biomedical diagnostics and chemical analyses. In 1998, "Booms in Biochips" recognized biochips as one of the discoveries transforming ideas about the natural world and also offering significant benefits to the society [41]. The growth in biochip research can be correlated with the total biochip market size, which was about \$2.0 billion in 2004 and is projected to grow to about \$5.1 billion in 2009 with a compound annual growth rate of 20.2% [42]. The number of publications in the field of microfluidics in terms of manuscripts have also grown rapidly rising from just 77 publications in over 43 different journals in 1999, to 581 publications in 165 journals in 2003 [43].

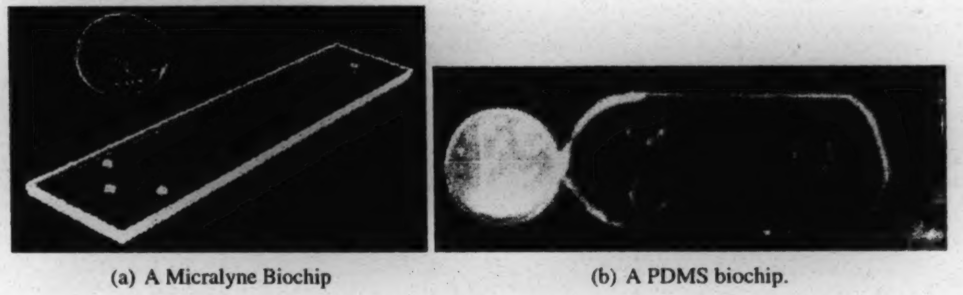

(a) A Micralyne Biochip

(b) A PDMS biochip.

Figure 1.4: *Two different biochips fabricated on glass and PDMS.*

A commercial biochip by Micralyne Inc., Edmonton, Canada is shown in Figure 1.4(a). These biochips are made by fusing together two pieces of glass, the lower one of which has etched grooves that become the channels. Polymers have been used to bring down the cost, and reduce the fabrication time. Hot embossing on polymethacrylate (PMMA) [44] and rapid prototyping in polydimethylsiloxane (PDMS) [45, 46] are two methods used extensively to fabricate biochips in polymer. These two methods are a part of the present research and are discussed in Section 3.2.3. Figure 1.4(b) shows one such biochip fabricated in PDMS and sealed on glass.

1.3.2 Optical Integration in Biochips

A cell or any chemical species can be identified by detection methods in microsystems. Fluorescence sensing is the most widely used methodology in biochip technology [47, 48].

Fluorescence detection offers sensitivity and compatibility with standard biochemical reactions [39, 49]. There has been a requirement for a high-performance fluorescence detection system due to the many functions being implemented on a small platform [50].

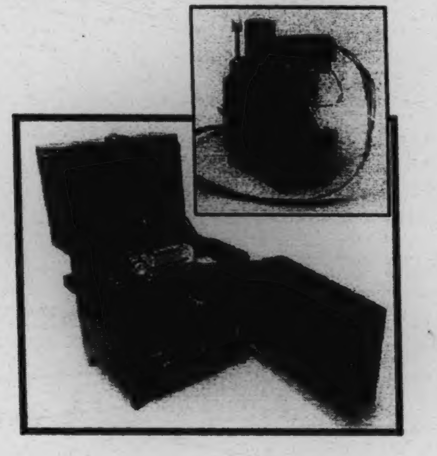

Figure 1.5: *A commercially available microfluidic toolkit sold by Micralyne Inc. of Edmonton, Alberta.*

Traditional fluorescence detectors use bulky and discrete elements which are expensive and require precise alignment [51]. The advantages of integrated biological analysis systems are reduced when these systems rely upon large and fragile optical sensing equipment. The microfluidic toolkit (Figure 1.5) sold by Micralyne has such a bulk-optical system. This toolkit costs tens of thousands of dollars and utilizes a Micralyne chip (as shown in Figure 1.4(a)) which itself costs several hundred dollars.

An integrated detection system should be chosen based on factors like sensitivity, sample volumes and scalability to dimension comparable to the microchips, for miniaturization of the whole device [52, 53]. The requirement of optical detection in biochips leads to opto-biochips.

One of the goals of the present research is to eliminate the bulky optics used in the microfluidic toolkits and use waveguides to shine light on and capture fluorescence from moving microparticles and deliver it directly to a photomultiplier tube controlled by LabVIEW running on a computer. The optical detection system has been integrated in polymer biochips[54, 55]. Different detection techniques are summarized in the review papers [23, 56].

In recent years, biochips were fabricated in our lab by different methods which are discussed in the following section.

1.3.3 Previous Research in Micro-Optical Systems Lab

In the Micro-Optical Systems (MOS) lab, the theme of the research is to integrate microfluidic biochips with integrated optics. This way, the whole system can be miniaturized and can enhance the capabilities of a biochip analysis system. Three different methods of fabricating microfluidic devices with integrated waveguides have already been developed in our lab and are discussed below.

Laser-Written Microchannels and Waveguides

In this research, microchannel walls and waveguides were written in UV-curable Norland optical adhesives (NOAs - index of refraction 1.53) on glass substrates [57] (Figure 1.6(a)). After washing away the uncured adhesive, the channels were sealed with a thin microscope slide cover. This way, channel walls with intersecting waveguides were created. The total fabrication time for such systems is about an hour. A completed biochip fabricated by this method is shown in Figure 1.6(b).

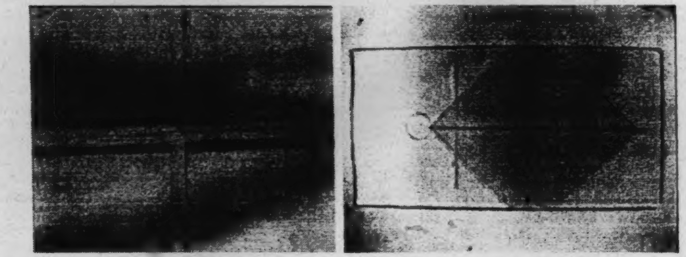

(a) Laser-written channel walls and intersecting waveguide.

(b) Laser-written crossed channel system with glass lid. Circle at left is a reservoir for introducing fluid samples.

Figure 1.6: *Laser-written biochip.*

In this approach, the fabrication time is short and the system has been successfully tested for microparticle detection [57]. A drawback is that the polymer structures are not very robust and a very delicate handling is needed while supplying fluid through the reservoir.

Microfluidic Biochip with Ion-Exchanged Waveguides

In the second method, waveguides in biochips were developed through a silver ion-exchange method in the same glass substrate that holds the microchannels [58, 59]. In this approach, multimode waveguides were integrated with conventionally etched microchannels in glass biochips. These biochips were fabricated by fusing together two pieces of glass, the lower one of which has etched grooves that become the channels. Figure 1.7(a) and Figure 1.7(b) show the propagation of the light along a straight and a circular-shaped ion-exchanges waveguides respectively [60].

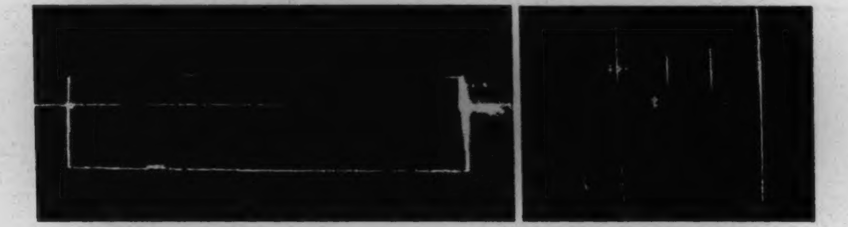

(a) Light propagation inside a biochip with ion-exchanged waveguide.

(b) Light propagation and bending inside a biochip with ion-exchanged waveguide.

Figure 1.7: *Biochip with ion-exchanged waveguides.*

This work presents a method to realize a device having microchannels and waveguides on the same platform. It has some drawbacks due to anomalous etching of microchannels [61] and a long and multi-step fabrication process. These biochips have been used to detect fluorescence from microparticles and to measure their velocities, which is a part of the present research and discussed in Chapter 4.

Two-level Biochip with Integrated Optics

In place of having fluidics and optics functionalities on the same level, biochips were fabricated with two layers, one for the fluidics and one for the optics. In a two-level biochip, the lower layer of the chip is made of silicon and provides the light guiding regions, while the upper PDMS/glass layer contains microfluidic channels [62] (Figure 1.8(a)). The light was guided and collected through metallized silicon v-groove hollow waveguides. Figure 1.8(b) is the picture of the complete device.

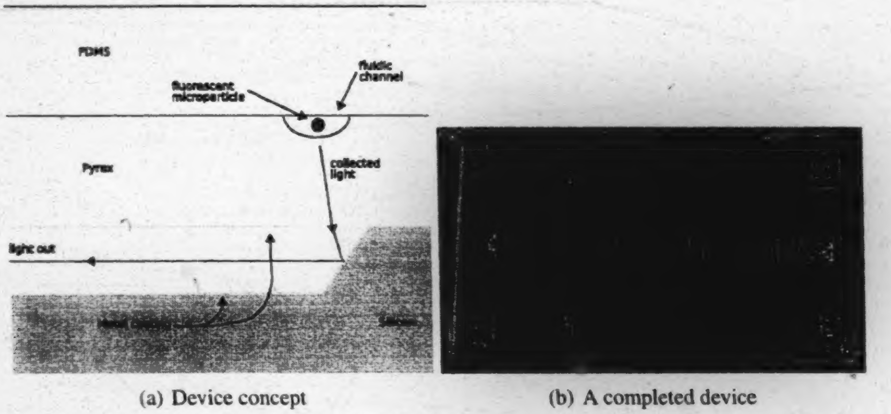

(a) Device concept

(b) A completed device

Figure 1.8: *Two-level biochip with integrated optics*

The two-level biochips chips were used successfully to shine light onto moving microparticles and to capture fluorescence from them. They have disadvantages such as complicated multi-level fabrication process and the difficulty in measuring the particle velocity.

Electronics and Data Analysis System

A critical component of a flow cytometry system is a sensitive light detection system using a photomultiplier tube (PMT). A fibre-fed system housed in a box in which the PMT, high-voltage socket, collimating optics (ball lens) and thin film filters are contained has been constructed [63]. The light enters the box via a pick-up fiber, and is collimated by a ball lens and filtered by two narrow bandpass 10 nm filters. The whole setup has been calibrated and fluorescence detection from microparticles, flowing through micropipette and microchannel, has been demonstrated. The details can be found in [64].

1.4 Scope and Goals of the Thesis

The emphasis in this thesis is on developing elements for microflow cytometer and to generate capabilities to use it as a cell-sorter. Based on the requirements to use the flow cytometer as a cell-sorter, there are two major goals of this thesis. The first is to fabricate an opto-biochip. The second major goal is the development of the flow system in an integrated biochip and the measurement of the velocity of moving microparticles . This was carried out by optical detection. In addition to the design and operation of the chip itself, the operation of the waveguide and sensitivity of the detection system were other important aspects and are summarized herein.

In later chapters, the following topics are described in detail:

- The overview of general principles of microfluidics and integrated optics is provided. Comparison between pressure-driven and electrokinetic flow and their behaviors, and requirement of integrated optics (Chapter 2).
- Fabrication techniques for opto-biochips by laser writing, lithography and a rapid prototyping on polymer. A direct and single step fabrication of microchannels with integrated waveguides in a single material, SU-8. (Chapter 3).
- Optical detection and velocity measurement in a microcapillary, ion-exchanged opto-biochips and rapidly prototyped biochips (Chapter 4).
- The development of techniques for optical detection, velocity measurement and waveguide loss measurement in SU-8 opto-biochips (Chapter 5).
- The summary of results and suggestions for future work (Chapter 6).

Chapter 2

General Principles of Microfluidics and Integrated Optics

2.1 Microfluidics Overview

2.1.1 Microfluidics Flow Properties

Microfluidics refers to the science of manipulation of very small reagent volumes, and the fabrication and formulation of devices and processes to handle such reagents. The dimensions of microfluidic devices range from millimeters down to micrometers [65, 66]. Microparticles suspended in the fluid or particle of fluid become comparable in size with the device itself. Due to this, different forces become dominant and certain physical phenomenan change at the microscale. Some of the physical phenomena, which are very important to study at the microscale, are Reynolds number, laminar flow, diffusion, and surface tension [24]. Some of these parameters are defined in the following section.

Laminar and Newtonian Flow

Laminar flow is a flow regime in which fluid motion is smooth and orderly, and in which adjacent layers or laminas slip past each other with little mixing between them. For most flows in microchannels, the flow is laminar and the familiar turbulent mixing of macroscopic devices vanishes. A Newtonian flow is a type of flow in which shear stress is linearly proportional to the velocity gradient in the direction perpendicular to the plane of shear. The constant of proportionality is known as the viscosity.

Compressible fluid

A fluid is called compressible if changes in the density of the fluid have significant effects on the solution. If the density changes have negligible effects on the solution, they are ignored and the problem is called incompressible. In reality, all fluids are compressible to some extent. In fluid mechanics, an incompressible fluid is a fluid whose density ρ is constant, and it does not change through time. The water based systems in the present work can be considered as incompressible.

Reynolds number and Laminar flow

The most striking feature of microfluidic devices is the dominant role of viscosity in mass transport phenomena. The Reynolds number is a measure of the ratio or the relative importance of the inertia force on an element of fluid to the viscous force of an element. When the Reynolds number is less than approximately 1000, the flow will be laminar [67]. For a microscale flow the Reynolds number, R_e is given by

$$R_e = \frac{\rho v(2h)}{\eta} \tag{2.1}$$

where ρ is the density, v is the velocity and 2h is the width or depth of the microchannel. In the present work, $\rho = 10^3$ Kg/m^3 for water, $2h \leq 100\mu m$ is the channel width, $\eta = 10^{-3} N.s/m^2$ and a typical velocity is $<$ 1 cm/s. This leads to $R_e < 1$ implying laminar flow.

Electric Double Layer (EDL)

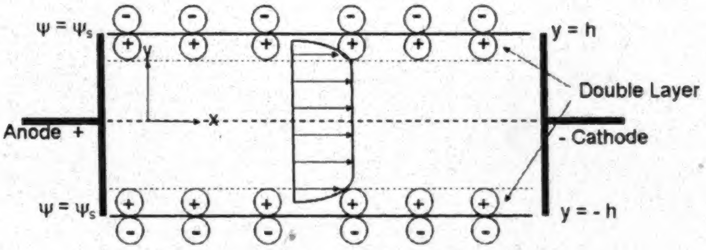

Figure 2.1: *Pressure driven flow and electroosmotic flow in a microchannel*

Consider a horizontal microchannel formed by two parallel plates made of glass, as shown in Figure 2.1. Like many solid surfaces, the walls of the microchannel carry electrostatic charges (negative for glass). When an aqueous solution (generally electrical neutral) flows in the microchannel, the counter ions (positive for glass) from the bulk liquid are attracted towards the wall. Due to this, the counter-ion concentration near the solid surface becomes higher (and co-ion concentration becomes lower) than that in the bulk liquid far away from the wall. There is a net charge in the vicinity of the walls due to the excess counter-ions, which balances the charge at the wall. The layer between the charge wall and the layer of the aqueous solution containing the balancing charges is called the electrical double layer (EDL). The charge density of counter-ions decreases from the wall to the edge of the EDL in the liquid.

When an external field E_x is applied, the counter-ions will move towards the cathode and drag surrounding liquid with them due to viscosity. This ion drag results in a net flow of bulk liquid along the wall, which is called electroosmotic flow.

The electric potential $\phi(x, y)$, is the algebraic sum of the potential due to the external electric field E_x and the potential due to the electric double layer $\psi(y)$, is given by,

$$\phi(x, y) = (\phi_0 - xE_x) + \psi(y) \tag{2.2}$$

where ϕ_0 is imposed potential at x=0.

Poisson-Boltzmann equation

The Poisson-Boltzmann equation defines the potential distribution in the EDL. The EDL potential $\psi(y)$ can be derived as [68],

$$\frac{\partial^2\psi(y)}{\partial y^2} = \frac{2zen_\infty}{\varepsilon} \sinh\left(\frac{ze\psi}{k_B T}\right) \tag{2.3}$$

where z is the absolute value of ionic valance of the electrolyte, ε is the permittivity of the medium, k_B is the Boltzmann constant and T is absolute temperature. The ionic number concentration, n_∞ (unit, m^{-3}) in the bulk electrolyte, can be expressed as,

$$n_\infty = 1000 \times M \times N_A \tag{2.4}$$

where M is the molarity (mol/L) and N_A is the Avogadro number ($6.022 \times 10^{23} mol^{-1}$).

Double layer thickness

The double layer thickness is a very important quantity in electroosmotic flow and depends explicitly on the liquid density and the wall-liquid interface. Using the Debye-Huckel approximation, z=1 and ψ = 25 mV, the zeta potential for water [69]. and applying boundary conditions in the microchannel, the solution of equation 2.3 is,

$$\phi(x,y) = [\phi_0 - xE_x] + \zeta\frac{\cosh(\kappa y)}{\cosh(\kappa h)} \tag{2.5}$$

where ζ is a surface potential, called zeta potential [69] and κ is the inverse double layer thickness or Debye-Huckel parameter, which can be expressed as,

$$\kappa = \left(\frac{2n_\infty z^2 e^2}{\varepsilon k_B T}\right)^{1/2} \tag{2.6}$$

This parameter depends strongly on molarity (because of n_∞, as shown in equation 2.4) and type (because of factor z) of the electrolyte. For a symmetric 1:1 (z=1) electrolyte, the permittivity of water $6.96\times10^{-10}\ C^2N^{-1}m^{-2}$ and at room temperature, the inverse double layer thickness can be written as (equation 2.6),

$$\kappa = 3310\sqrt{M}\mu\text{m}^{-1}. \tag{2.7}$$

In the present work (Section 4.2.3 and Section 4.3), a 10^{-4} molar solution was used. So the inverse Debye length is 33.10 μm^{-1} corresponding to EDL of 0.03 μm.

Navier-Stokes Equation

The Navier-Stokes equation describes the flow of fluids in any system. For the present case of flow of microfluids, these equations can be deduced by combining all the forces per unit volume on the fluid, and balancing forces on a fluid element. Newton's law for fluids can be written as:

$$\rho\frac{d\overrightarrow{v}}{dt} = \text{F} = \text{F}_{\text{viscous}} + \text{F}_{\text{pressure}} + \text{F}_{\text{electric}} + \text{F}_{\text{body}} \tag{2.8}$$

or,

$$\rho\frac{\partial\vec{v}}{\partial t} + \rho(\vec{v}.\vec{\nabla})\vec{v} = \eta\nabla^2\vec{v} - \vec{\nabla}P + \rho_f\frac{\partial\phi}{\partial x} + \rho\vec{g}. \tag{2.9}$$

Equation 2.9 represents the Navier-Stokes equation where g is the acceleration due to gravity. Here, ρ_f is the net charge density of free ions. For steady-state conditions in a channel of constant cross-section with laminar flow, the Navier-Stokes equation will take the following form

$$\eta\nabla^2\vec{v} = \vec{\nabla}P - \rho_f\frac{\partial\phi}{\partial x} - \rho\vec{g}. \tag{2.10}$$

2.1.2 Flow Velocity in Laminar Flow

When there is a fully developed flow in the microchannel, the velocity in the y-direction (v_y) can be taken as zero. Also, for one-dimensional continuous flow, $\partial v_x/\partial x$=0, and so the velocity v_x is solely a function of y. For a horizontal microchannel ($g_x = 0$), and there is no pressure gradient in y-direction (along microchannel width). So the Navier-Stokes equation for the x-direction becomes,

$$\eta\frac{d^2v_x}{dy^2} = \frac{\partial P}{\partial x} + \rho_f\frac{\partial\phi}{\partial x} \tag{2.11}$$

where v_x is the velocities and g_x is the acceleration due to gravity in x- direction.

For a fully developed flow, the pressure gradient $\partial P/\partial x$ is negative and a constant quantity, which can be represented as,

$$p_x = -\frac{\partial P}{\partial x}. \tag{2.12}$$

Using the boundary conditions (at $y = h, v_x = 0$, and at $y = 0, dv_x/dy = 0$), the solution of equation 2.11 is given by [68]

$$v_x(y) = v_x = \frac{h^2p_x}{2\eta}\left[1 - \left(\frac{y}{h}\right)^2\right] + \frac{|\varepsilon|E_x\varsigma}{\eta}\left[1 - \frac{\cosh(\kappa y)}{\cosh(\kappa h)}\right]. \tag{2.13}$$

Equation 2.13 gives an expression of variation of velocity across the microchannel due to both electroosmotic flow and pressure driven flow.

Velocity due to Pressure Driven Flow (PDF)

The first term in equation 2.13 is the flow velocity due to applied pressure gradient p_x only. Pressure driven flow is also called Poiseuille Flow. The velocity due to pressure driven flow can be expressed as,

$$v_p = \frac{h^2 p_x}{2\eta}\left[1 - \left(\frac{y}{h}\right)^2\right] \tag{2.14}$$

and the maximum velocity at the center of the microchannel ($y = 0$) is,

$$v_{p,\max} = \frac{h^2 p_x}{2\eta} = \frac{h^2}{2\eta}\left(\frac{\rho d g}{L}\right). \tag{2.15}$$

where ρ is the density of the liquid, d is the height of the liquid and L is the length of the microchannel (Figure 2.2).

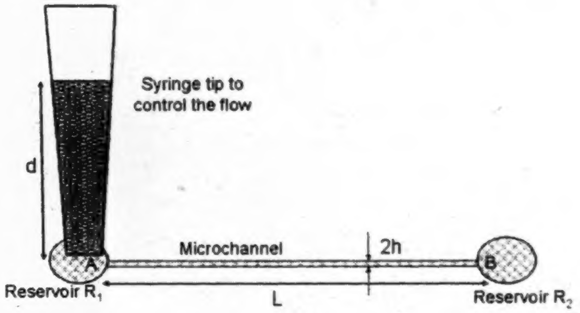

Figure 2.2: *A schematic of the effect of hydrodynamic pressure.*

The velocity due to pressure driven flow has a parabolic profile when plotted against y/h, and depends very much on channel width $2h$ for given pressure gradient and the fluid viscosity. Figure 2.3 shows the variation of dimensionless flow velocity ($v_p/v_{p,max}$) across the channel due to pressure driven flow.

For a water density of $10^3\ Kg/m^3$, $g = 9.81 m/s^2$ and the viscosity $10^{-3}\ Ns/m^2$ the maximum velocity at the center of the microchannel can be represented as,

$$v_{p,\max} = 4.9 \times 10^{-3} \frac{d(cm) \times (h(\mu m))^2}{L(cm)} mm/\sec \tag{2.16}$$

which can be calculated for hydrodynamic pressure height, microchannel length and microchannel half width (Figure 2.2).

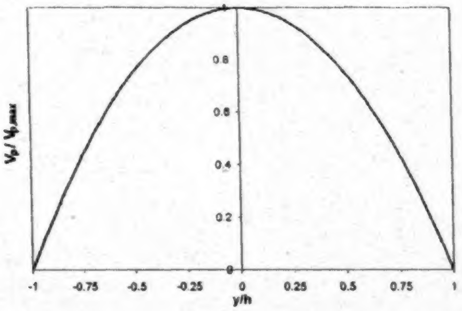

Figure 2.3: *Dimensionless velocity profile due to pressure driven flow*

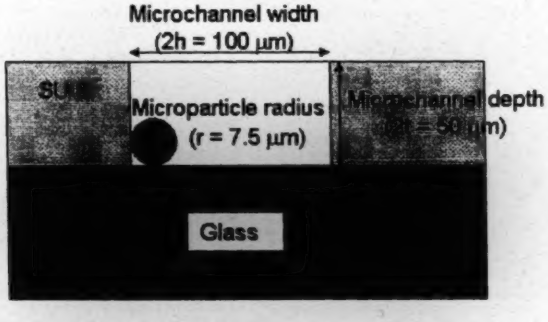

Figure 2.4: *Dimensions of the microchannel with one particles inside it.*

For the experiment discussed in Section 5.3, the values of $t = 25\mu m$, d = 2 cm and L = 3 cm, give a maximum velocity due to pressure-driven flow of approximately 2 mm/sec. The dimensions of the microchannel are shown in Figure 2.4. The calculated velocity is higher than the maximum velocity, seen in the microflow experiment, as desribed in Section 5.3. This can be explained by considering the position, size and density of the microparticles. The diameter and density of the microparticles in the present research are 15 μm and $1.05 \times 10^3 Kg/m^3$ respectively [70]. Due to the size of the particle, the velocity at the edge of the particle will be different from the velocity at the center of the particle. Figure 2.4 shows one such microparticle residing in the microchannel. From equation 2.14 and figure 2.3 it is clear that the position of the microparticle effects the velocity of the microparticle. Due to the density of the particle, it may sink to the bottom of the microchanel. The velocity of the microparticles decreases by more than 50 % (from 2 mm/s to 1 mm/s) if the particle flows at the bottom of the microchannel. Surface roughness [71] and friction [72] from the walls also affect the velocity of the microparticles.

Velocity due to Electroosmotic Flow (EOF)

The second term in equation 2.13 represents the flow velocity due to electroosmotic flow (EOF). The velocity as a consequence of imposed electric field E_x can be represented as,

$$v_e = \frac{|\varepsilon|E_x\varsigma}{\eta}\left[1 - \frac{\cosh(\kappa y)}{\cosh(\kappa h)}\right] \tag{2.17}$$

The maximum velocity due to electroosmotic flow (for $y = h$)will be,

$$v_{e,\max} = \frac{|\varepsilon|\ E_x\varsigma}{\eta} = \frac{|\varepsilon|\ V_x\varsigma}{\eta L} \tag{2.18}$$

where V_x is the applied voltage across the microchannel and L is the length of the microchannel.

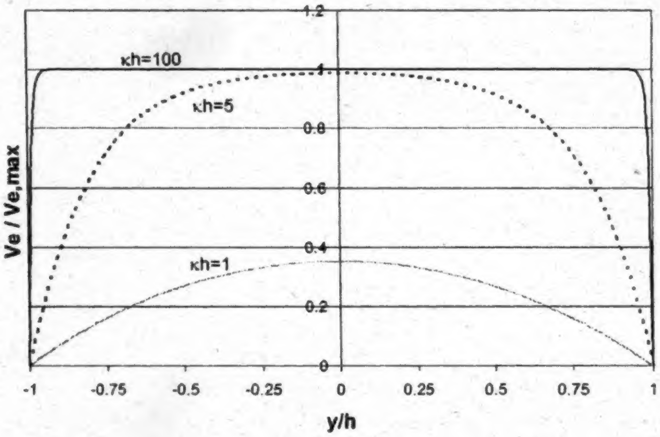

Figure 2.5: *Dimensionless velocity profile due to electroosmotic flow for different κh values.*

Equation 2.17 shows that the electroosmotic velocity (v_e) depends on the electric double layer thickness κ^{-1} and the channel width $2h$. For the permittivity of water, 6.96×10^{-10} $C^2N^{-1}m^{-2}$, and zeta potential near wall of 25 mV [69], the velocity due to electroosmotic flow can be represented as,

$$v_{e,\max} = 1.74\frac{V(volts)}{L(cm)}\mu m/\sec \tag{2.19}$$

for an applied voltage of 200 V, and 2 cm long microchannel (Section 4.2.3), the calculated velocity is 174 $\mu m/sec$ and for a 3 cm microchannel (Section 4.3), the velocity is 110 $\mu m/sec$. At 200 V the velocity was measured to be 400 $\mu m/sec$ in glass biochips with ion-exchanged waveguides (Section 4.2.3) which is quite differnet from the theoretical value. In PDMS biochips, the velocity was 115 $\mu m/sec$ at 200 V. The difference between theoretical and experimental values of velocities may be due to a pressure effect as discussed in Section 4.2.3.

Figure 2.5 shows the variation of dimensionless flow velocity due to the electroosmotic flow at different κh values. It is clear that the velocity due to electroosmotic flow is plug-like for high κh values (more than 100). For a 10^{-4} molar solution, the inverse Debye length is 33.10 μm^{-1} (from equation 2.7). For the ion-exchanged opto-biochip (Section 4.2.3) with 157 μm wide microchannel, the κh value is approximately 2598. Similarly, for the PDMS biochip (Section 4.3), with 100 μm wide microchannel, the κh value is approximately 1655. The κh values will give a fairly flat velocity profile throughout the channel for electroosmotic flow during experiments.

2.1.3 Comparing Pressure Driven Flow and Electroosmotic Flow

The velocity distributions due to pure pressure driven flow and electroosmotic flow are shown in Figure 2.3 and Figure 2.5. It is clear from equation 2.14 that for a given pressure gradient p_x and viscosity μ, the velocity due to pressure-driven flow varies parabolically and the maximum velocity is proportional to h^2. The pressure driven flow becomes impractical for very small channel width. Contrary to this, electroosmotic flow velocity is a strong function of electric double layer thickness κ^{-1} for a given electrolyte and applied electric field.

Also for small channel widths, the velocity profile due to electroosmotic flow can be made to be flat by incorporating a fluid with higher molarity, which is directly proportional to the inverse double layer thickness. So, for narrow channels, the electroosmotic flow is more effective than pressure driven flow for $\kappa h \gg 1$. This is a unique property of electroosmotic flow over pressure driven flow for very small channels.

Table 2.1: List of physical parameters affecting electroosmotic and pressure-driven flows

Physical Property	**General consequence**	**Pressure Driven Flow**	**Electroosmotic Flow**
Material selection	Wall property changes because of charge distrubution	No effect (should be rigid)	Wall property changes double layer thickness and in turn EOF changes.
Electric Field	Changes flow of ions	No effect	Decreasing electric field results in decrement of efficiency and resolution and increasing electric field resuts Joule heating.
Ionic Concentration	Inversely proportional to surface potential and EDL thickness and generates high currents.	No effect	Decreasing ion concentration results may result in sample adsorption. Increasing ion concentration results in Joule heating.
Buffer pH value	Changes charge and solute structure.	No effect	EOF decreased at low pH, increased at high pH.
Organic Modifier	Changes zeta potential and viscosity.	No effect	EOF is usually decreased.

The advantages of EOF are a flat velocity profile that is independent of the microchannel width. So, electroosmotic flow plays an important role for microflows. Table 2.1 presents list of physical parameters affecting these two laminar flows.

Although the EOF gives a very homogeneous flow and can be used for small microchannels, it has many drawbacks mostly due to the applied electric field and properties of electrolyte. Researchers have used different methods to control EOF flow. However, in many cases such as in Joule heating [73] it is very diffult to control EOF. The poor resolution time is detrimental while using EOF for separation methods [74]. For not-so-small microchannels, pressure driven flow gives a significant value of velocity and one does not need to worry about understanding the effects of different chemicals used in the experiments. Pressure driven flow can be achieved in microchannels by applying a hydrostatic pressure in the microchannels. This method has been used in observing flow in capillaries with 200 μm diameter [64] and integrated SU-8 microchannels with dimensions of 50 $\mu m \times 100\ \mu m$ in the present research (Chapter 5). However the variation of velocity with position leads to a spread of particle velocities and pressure driven flow is more difficult to switch.

2.2 Integrated Optics Overview

Optics describes the behavior and properties of light and the interaction of light with matter. As light is an electromagnetic wave, optics can thus be regarded as a sub-field of electromagnetism [75]. We can find optical science a part of many related disciplines including electrical engineering, physics, medicine, and others. Integrated optics [76] refers to the implementation of different optical elements on a chip [77].

2.2.1 Waveguiding Principle

A waveguide is a structured inhomogeneous material medium. The central region of the waveguide is the core, where a propagating electromagnetic wave is confined and guided. The phase velocity of electromagnetic radiation (v) in a material is slowed relative to vacuum (c) by a factor which is defined as the index of refraction of that material.

$$n = \sqrt{\varepsilon_r \mu_r} = \frac{c}{v} \tag{2.20}$$

where ε_r is the relative permittivity, μ_r is the relative permeability of the material.

Light bends at the interface between two media of different index of refraction, and may be curved in a medium in which the refractive index is a function of position. The index of refraction determines the amount of refraction between the two different media. Snell's law defines the refraction and bending of light when traveling between two media of differing index of refraction as shown in Figure 2.6(a). In mathematical form, this law can be written as,

$$n_1 \sin\theta_1 = n_2 \sin\theta_2 \tag{2.21}$$

In the above case, light travels from a denser (high refractive index) medium with to

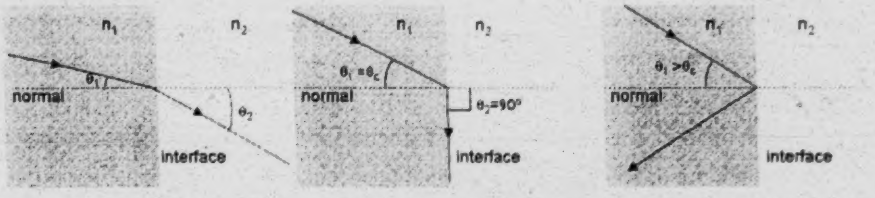

(a) Snell's Law (b) Critical angle in refraction (c) Total Internal reflection

Figure 2.6: *Snell's law and Total Internal Reflection.*

rarer (low refractive index) medium, so the angle of refracted light, θ_2 is bigger than the angle of the incidence θ_1. Now, at a certain critical angle, the angle of refraction is 90^o to the normal. This incidance angle is called the critical angle (Figure 2.6(b)) and can be written as,

$$\theta_c = \sin^{-1}\left(\frac{n_2}{n_1}\right) \tag{2.22}$$

For any incident angle more than the critical angle ($\theta_1 > \theta_c$), no refracted ray appears, and the incident ray undergoes total internal reflection from the interface. This is shown in (Figure 2.6(c))

2.2.2 Structure of a Waveguide

A dielectric waveguide consists of a dielectric material surrounded by another dielectric material with a lower refractive index. These two materials are called the core and cladding respectively. Propagation of light in a dielectric waveguide occurs due to total internal reflection. Light propagation in a waveguide is shown in Figure 2.7 where n_1 and n_2 are the index of refraction of core and cladding regions and θ_1 is the incidence angle from air. An example of a waveguide with a cylindrical core is the optical fiber, which is widely used as a low loss transmission system for long distance communication [78].

A mode in a dielectric waveguide is a particular electromagnetic field pattern that propagates along a uniform waveguide without changing its shape. These modes occur because of boundary conditions imposed on the wave by the waveguide. Only a certain discrete number of modes are capable of propagating along the waveguide [78].

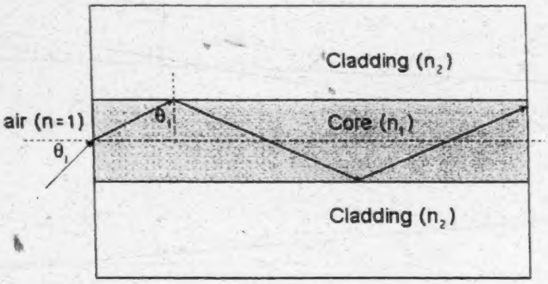

Figure 2.7: *Light propagation in a waveguide due to total internal reflection.*

In a single-mode waveguide only the lowest order bound mode can propagate at the wavelength of interest. Single mode fibers are best at having very low losses over longer distances. In multi-mode waveguides, many modes can propagate at the same time and each mode propagates with a slightly different velocity and so the modes in a given optical pulse arrive at the waveguide end at slightly different times. Thus, there is pulse spreading in multimode waveguide which is not present in the case of singlemode waveguides. Typically, multimode silica fibers have core diameter of 50 to 300 μm while singlemode fibers have core diameter of 8-12 μm [78].

Multimode waveguides have several advantages over single mode waveguides. First, the large core size makes it is easy to launch light into the waveguide and to connect similar waveguides. Light can be launched into multimode waveguides using a light-emitting-diode, whereas laser diodes are typically used to launch light into singlemode fibers.

2.2.3 Requirement for Integrated Optics

As discussed in Section 1.1.1, the detection unit is a crucial component for a flow cytometer. Optical detection, and in particular fluorescence detection is the most common among the integrated detection methods in the present biochemical systems [47, 56]. Traditionally, bulk optical equipments, such as lenses and microscope objectives have been used for fluorescence detection [33, 51]. Also, different types of optical fibers have been used to launch and capture light on to a sample in a chip [79, 80]. These methods of detection require precise mechanical alignment and suffer from instabilities due to vibrations and thermal gradients.

Since the 1960s, researchers have been combining different electrical and optical components, such as diffraction gratings, beam splitters, modulators on the same dielectric layer on a substrate. This field of optics is called Integrated Optics [76]. Integrated optic devices are rugged and performance is theoretically much better, since all the components lie on a common platform and are self-aligned . Integrated optics based on waveguides can be fabricated on same substrate to match the microfluidic channels and can guide the beam in the plane of the chip [49, 81].

The monolithic integration of diverse optical elements with electronic devices is a great challenge. This is because each optical function typically requires a unique material system. So material compatibility is a major issue to monolithically integrate different photonic and electronic component on same platform. For our research, the main motivation to use integrated optics is to fabricate waveguides and microchannel on same substrate. The aim of our research is to investigate a material which can work as a core region of waveguide and at the same time can be compatible to microfluidics (Section 2.2.2). SU-8 is one such material, which is widely used to fabricate mirofluidic devices [82, 83]. SU-8 can be used as the core of a waveguide (glass as a substrate material) due to its excellent optical properties and a higher index of refraction (1.59) than glass (1.50).

2

Chapter 3

Fabrication Techniques for OptoBiochips

3.1 Material Selection Criteria

Fabricating and packaging microfluidic devices depends on careful material selection to match mechanical, electrical, and other properties to functionality. Proper materials must be chosen for the device substrate, the electrode layer, the fluid flow layer, any necessary gasket or sealing material, and the packaging (in all its components) [40]. Some basic criteria when choosing materials are as follows:

- Easy and fast (1 day or less) to fabricate or machine.
- Fabrication procedures are available in-house or from literature.
- Inexpensive and readily available.
- Non-toxic or (even better) bio-compatible.
- Rigid (for the substrate, packaging, and possibly flow layer) or flexible as necessary.
- Reproducibility is possible.

Other material selection criteria, of course, exist specific to each subsystem. In most cases, the simplest routes have been taken where more complicated materials might be more suitable in the long term.

5

Fabrication of biochips started with silicon [32, 84, 85], glass [33, 86] and quartz [87, 88] as substrate materials, with a set of microchannels etched into the surface. This was primarily driven by the fact that fabrication methods were well established by the semiconductor industry and several material properties of these materials make them very attractive materials for use in microfluidic systems [39, 53, 89]. Companies like Micralyne sell glass biochips, used extensively for biochip research [38]. There are limitations of using microfluidic systems in glass, quartz and silicon for the rapid production of devices and testing new applications [40]. A clean-room facility is required and the materials are fragile.

During the past few years, people have started making microfluidic systems and biochips from low-cost polymers such as PDMS (polydimethsilloxane), PMMA (polymethymethacrylate), and PETG (poly-ethylene tere-phthalate glycol) [40]. One of the main reasons to use these polymers for microfluidic applications is because their cost is very low and they are less fragile than glass and silicon [90]. Many polymer materials have good optical transparency and low electrical conductivity for high voltage applications such as electro-osmotic flow. With polymers, the manufacturing process is simplified compared to glass and silicon, and mass production of biochips is possible with polymers. Also, a wide range of plastic material is available, which allows the manufacturer to choose properties of the material suitable for their specific application [91, 92].

3.2 Different Fabrication Approaches in the Present Research.

Different approaches to fabricating biochips used in the present research are shown in Figure 3.1. A UV laser-writing system is used to fabricate complete devices in spun-on UV-curable Norland-curable adhesives [93] on glass substrates (Section 3.2.1). A master (defined in Section 3.2.2) is fabricated using either the laser-writing system (Section 3.2.2) or lithography (Section 3.2.2). The master is used to fabricate biochips by PDMS casting (Section 3.2.3) or hot embossing (Section 3.2.3) in PMMA. Biochips with integrated waveguides are fabricated on glass in a single-step process by using a negative photoresist SU-8 (Section 3.2.4). Properties of the materials considered for each subsystem in the

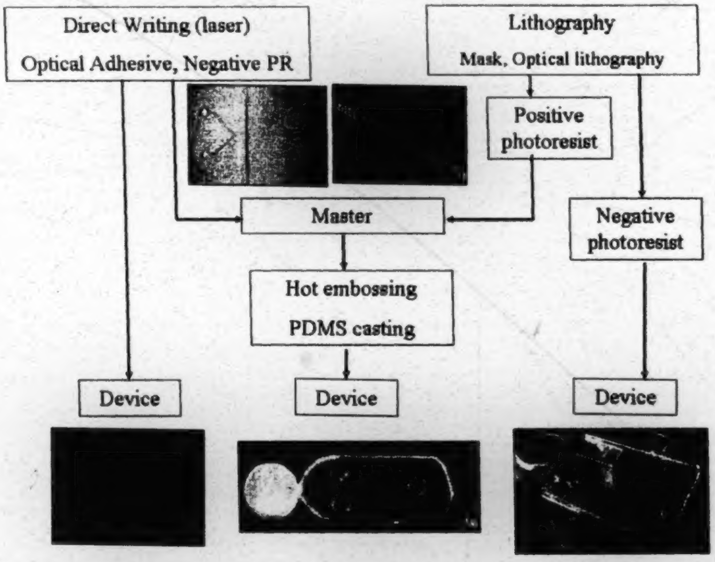
Direct Writing (laser)
Optical Adhesive, Negative PR
Lithography
Mask, Optical lithography
Positive photoresist
Master
Negative photoresist
Hot embossing
PDMS casting
Device
Device
Device

Figure 3.1: *Different approaches to fabricate biochips used in the present research.*

present work are given in Appendix A.

3.2.1 Direct Device Fabrication by Laser-Writing

Laser-writing was used to fabricate waveguides and microchannels in one step. As the NOA has a higher index of refraction than air and glass, the NOA ridges work as the core of the waveguide where as the air work functions as cladding.

Laser-Writing Process

A He-Cd UV laser (325 nm from LiCONIX) writes ridges in spun-on UV-curable Norland optical adhesives (NOAs) [93] on glass substrates. The uncured adhesive is washed away. The total fabrication time for fabricating a device or a master is a few hours. Figure 3.2 shows a schematic of the laser writing setup.

The following method has been used to calculate the required speed v of the movement of the stages where the substrate with NOA is placed. If the total energy required to cure NOA is 4.5 joule/cm^2 [93] then,

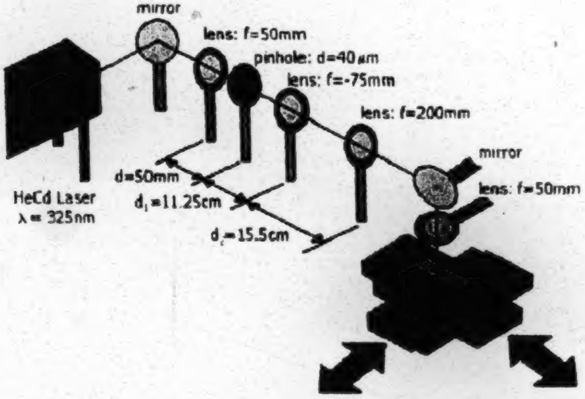

Figure 3.2: *Schematic of the Laser writing setup*

$$4.5\mathrm{joules/cm^2} = \frac{\mathrm{Energy}}{\mathrm{Area}} = \frac{\mathrm{Time} \times \mathrm{Power}}{\mathrm{SpotArea}} = \frac{(\mathrm{D/v})\,\mathrm{W}}{(\pi \mathrm{D}^2/4)} = \frac{4\mathrm{W}}{\pi \mathrm{vD}} \tag{3.1}$$

where W is the laser output power and D is the diameter of laser spot. Therefore,

$$\mathrm{v} = \frac{4\mathrm{W(watts)}}{4.5\mathrm{D(cm)}}\mathrm{cm/sec} \tag{3.2}$$

For a spot size of 0.1 mm and output power of 0.1 mW, the motor speed can be calculated from Equation 3.2 to be approximately 0.1 mm/sec.

The output power is a critical factor in determining the quality of the final shape of epoxy. High power generates a size larger than the beam diameter due to thermal curing of the polymer beyond the beam diameter. Low power results in partially cured shapes which are often washed away during the rinsing process.

Pattern generation

A motor drive (Klinger, MD4) was used to move the stages. The motor control board interface programmed in *Labview*^{TM} by Dean Spicer (M.Sc. 2005) is shown in Figure 3.3. The controls for the stage are in the top left part. The controls for creating commands

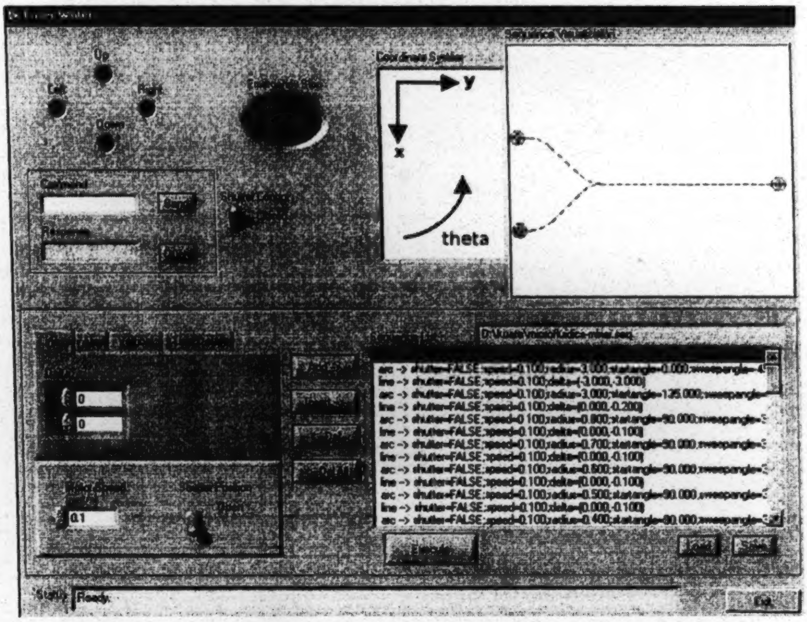

```
D:\Users\microfluidics-chip.seq
arc -> shutter=FALSE;speed=0.100;radius=3.000;startangle=0.000;sweepangle=4
line -> shutter=FALSE;speed=0.100;delta=(-3.000,-3.000)
arc -> shutter=FALSE;speed=0.100;radius=3.000;startangle=135.000;sweepangle=
line -> shutter=FALSE;speed=0.100;delta=(0.000,-0.200)
arc -> shutter=FALSE;speed=0.100;radius=0.800;startangle=90.000;sweepangle=
line -> shutter=FALSE;speed=0.100;delta=(0.000,-0.100)
arc -> shutter=FALSE;speed=0.100;radius=0.700;startangle=90.000;sweepangle=
line -> shutter=FALSE;speed=0.100;delta=(0.000,-0.100)
arc -> shutter=FALSE;speed=0.100;radius=0.600;startangle=90.000;sweepangle=
line -> shutter=FALSE;speed=0.100;delta=(0.000,-0.100)
arc -> shutter=FALSE;speed=0.100;radius=0.500;startangle=90.000;sweepangle=
line -> shutter=FALSE;speed=0.100;delta=(0.000,-0.100)
arc -> shutter=FALSE;speed=0.100;radius=0.400;startangle=90.000;sweepangle=
```

Figure 3.3: *Screen-shot of the Labview interface of motor controlled board.*

for the movement of axis are in bottom left part, queue for all these commands are in the bottom right box. The design was first drawn in this software, the graphical result of one design is shown in top right side of this figure. Laser fabricated patterns are shown in Figure 3.6

Figure 3.4 shows different parts of the microfluidic chip fabricated by direct laser writing. The pictures A, B and C are the parts joining the microchannel with three reservoirs respectively. The picture D is the Y-shape part of the microchannel and picture E shows the NOA waveguides joining with the walls of the microchannel. Figure 3.5 shows the propagation of light along NOA ridge.

In this method, there was no need to design and fabricate a relatively expensive and time consuming mask but it could not be used as a microfluidic device due to some limitations. As only a few tiny epoxy ridges of NOA hold the chip, it was difficult to find a suitable way to cap these chips to realize a robust microfluidic channel. An improvement to fabricate a complete device by laser writing using different material is proposed in Section 6.2.

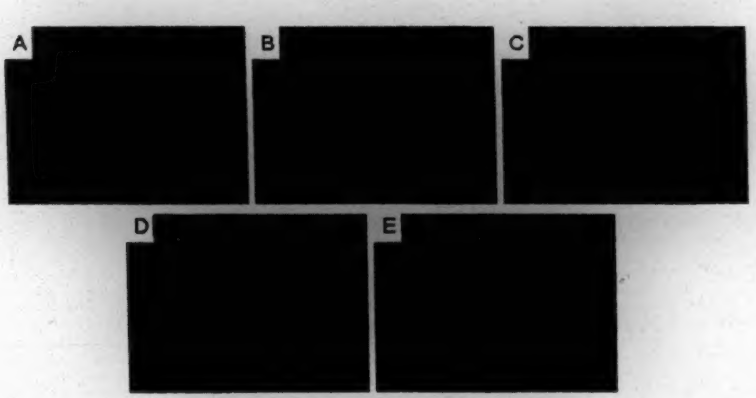

Figure 3.4: *Different parts of biochip with Y-shape microchannel fabricated by NOA. The pictures A, B and C are the parts joining the microchannel with three reservoirs respectively. The picture D is the Y-shape part of the microchannel and picture E shows the NOA waveguides joining with the walls of the microchannel.*

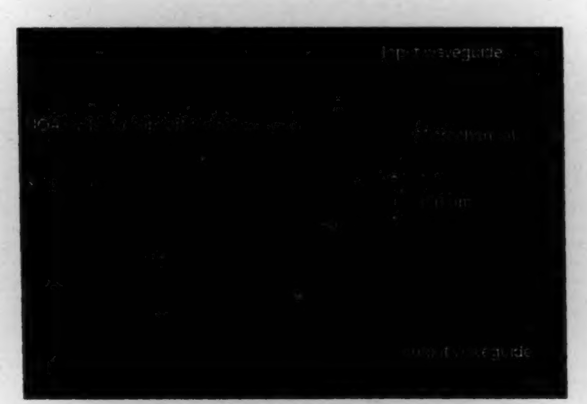

Figure 3.5: *A NOA chip with microchannels and waveguides (Figure 3.4 (E)). NOA ridges work as the core of the waveguide and the walls of the microchannel. Light is propagating through the waveguide and shining light at a point on the microchannel. The white spots are due to scattered light from imperfections in the walls.*

3.2.2 Master Fabrication

In order to fabricate biochips in polymers [40], fabrication of an inverse pattern is required to replicate in the polymer [45]. These inverse patterns are called masters and this approach is known as Soft Lithography. Soft lithography allows the rapid reproduction of features as small as 80 nm, creating a soft and inexpensive negative of the original master (Section 3.2.2) [94]. This technique has found diverse applications, including patterned surface deposition, photonics and microfluidic device fabrication [94, 95, 96].

There are several methods of master production in use today. One of the most popular methods is using thick photoresist (SU-8) to create ridges of microchannels [45]. Two methods were used during this project to fabricate masters with inverse patterns of microchannels. The first was direct laser writing without producing a mask and the second was using lithography and deep reactive ion etching to produce a master of the desired depth.

Glass Masters by Laser- Writing

A similar method, discussed in Section 3.2.2, was used to fabricate masters using laser-writing process. The fabricated patterns are shown in Figure 3.6 which were then used as masters to cast PDMS chips (Section 3.2.3) with opposite features. The PDMS casting process is shown in Appendix C. The chips fabricated by laser-written masters are inexpensive because the the expensive mask fabrication process is avoided in laser-writing system.

The masters fabricated with the laser writing process are significantly inferior to other methods. Because the polymer structures are not very robust they do not stand up to rough handling. The final cleaning of uncured epoxy by acetone leaves behind some residues. Ideally, the whole process should be completed in a clean room facility to produce much cleaner microchannels.

Silicon Masters by Lithography and Dry Etching

The project to fabricate silicon masters was carried out at the Nanofabrication Lab at the University of Alberta. The fabrication process is described in Appendix B. The masters

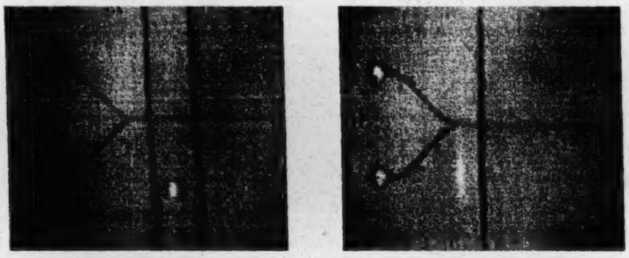
(a) (b)

Figure 3.6: *Different designed generated on glass slide by laser writing process, work as masters.*

fabricated by this method were used to prototype biochips by soft lithography in PDMS and hot embossing in PMMA (Section 3.2.3).

Mask design and fabrication

The first step is to make a mask that can be used to fabricate masters in silica/glass. This whole process is depicted in Appendix B. Later, the design was exported to the pattern generator, which transformed this design to a glass substrate, by a laser writing process. After this, the mask was developed on positive quartz and a chromium layer was patterned. The final mask is shown in Figure B.1 (b).

Silicon dioxide deposition

Silicon dioxide is a high-quality electrical insulator and should be used as a barrier material during different processes where shortcircuiting to the chip needs to be avoided. In the present process, SiO_2 was used as a etch mask for dry etching as described later in this section. The oxidation on clean silicon wafer was done in a MiniBrute furnace. For 0.5 μm of oxide thinkness, the wafer were kept in the oven for 6 hours at 1050°C.

Lithography

The optical lithography process was used to achieve exact structure as on the mask on silicon wafers. This process is shown schematically in Figure B and described in Appendix B.

Wet Etching of SiO_2

Usually etching processes are subdivided in two categories: wet and dry etching. After

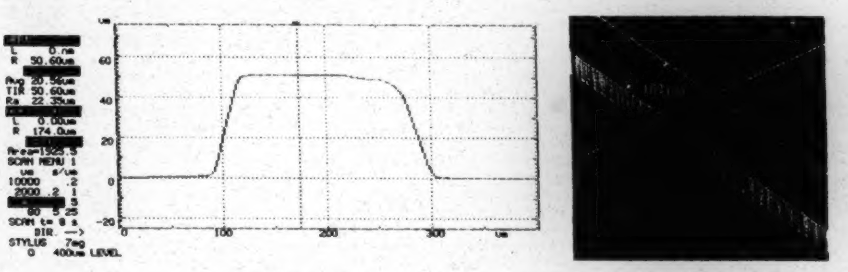

(a)

(b)

Figure 3.7: *(a) Depth measurement of the microchannel by the contact profilometer (this case shows the depth of left T shown in the mask layout in Figure B.1), and (b): SEM result of the side view of a cross on wafer.*

developing the photoresist, it is used as an etch mask that delineates the pattern geometry and protects the underlying film. Wet etching can be simply described as the dissolution of the material in the appropriate etchant. The resist must be resistant to the etchant in order to provide a good protection throughout the patterning process. Silicon dioxide is etched in a buffered oxide acid solution (BOE) at room temperature. BOE consists of 10 parts of Al_2F_3 and 1 part of H_2SO_4 and has typical etching values in the order of 800 Å/min.

Dry Etching of Silicon

After the lithography process, ICPRIE (inductance coupled plasma reactive ion etching) was used to achieve a desired depth in the range of 50 μm. This dry processing technique permits the fabrication of high aspect ratio silicon structures without limitation in geometry.

The results from the contact profilometer show (Figure 3.7(a)) the depth of the reverse pattern of the channel after ICPRIE was about 50 μm. The SEM results (Figure 3.7 (b)) also show the walls of the channel. The outside top surface was found to be smooth. The optical profilometer shows a depth of 53 μm for same channel (Figure 3.8 (a)). The roughness was found to be just 0.001% of the height (Figure 3.8 (b)). Using this process, the masters were found to have very smooth walls which should result in polymer biochips with smooth channel walls.

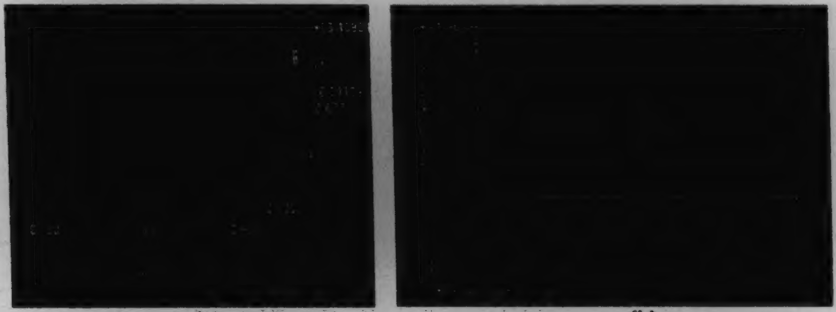

(a) (b)

Figure 3.8: *(a) Optical Profilometer picture to find the height of the microchannel (53.11 μm), and (b) Optical profilometer pictures to find the roughness of the top surface of the microchannel.*

3.2.3 Device Fabrication Using Polymers

Device Fabrication by PDMS Casting

The method of fabricating biochips using polydimethylsiloxane (PDMS) is discussed in Appendix C. PDMS is a stable, high-resolution elastometer, which can be used to make very accurate impressions of microstructures. PDMS can be used to rapidly prototype complex devices even at room temperature. Fabrication time from idea to chip completion can be less than 12 hrs. PDMS is a flexible rubber which protects against mechanical shock and thermal cycling stress and has excellent dielectric properties [45, 97]. PDMS is optically transparent in the visible range, so laser induced fluorescence detection can be facilitated [54, 55].

After making the PDMS mixture and casting it in a vessel containing the master, the vessel is kept in the vacuum oven at 80°C. The PDMS replica with negative relief channels and reservoirs in the PDMS was peeled off from the vessel and placed either on a precleaned microscopic slide or on another flat peice of PDMS.

The PDMS replica can be sealed ~~with glass~~ in two different ways. Reversible sealing (PDMS/Glass Chip) was performed by heating the slide on a hot plate and then bringing the two surfaces into contact with one another. Irreversible sealing (PDMS/Glass or PDMS/PDMS) was performed by first oxidizing the two pieces in the low temperature

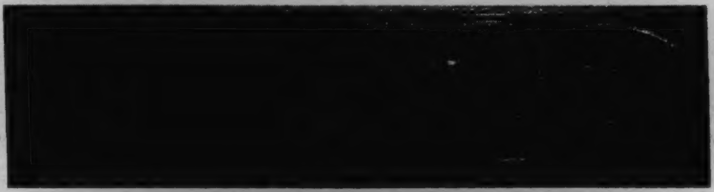

(a) PDMS bonded on glass

(b) PDMS bonded on PDMS

Figure 3.9: *Two PDMS chip with microchannels and reservoirs. The master was fabricated by the direct laser-writing.*

plasma and then immediately joining them together after removal from the RIE. After PDMS surface oxidization, the walls of the channels present a layer of silanol (SiOH) groups to an aqueous solution in contact with them. These surfaces are charged (SiO-) when the solution is neutral or basic, and so the channels support EOF toward the cathode. Plasma oxidation enhances the adhesion of PDMS with low surface energies, with a hydrophilic surface. One such PDMS microchip, with Y-shape microchannel and reservoirs (by irreversible sealing), is shown in Figure 3.9(a). Figure 3.9(a) shows a PDMS biochip fabricated by bonding two pieces of PDMS (the top one has a T-shape microchannel) by irreversible sealing. In both PDMS biochips, the master was fabricated by direct laser-writing (Section 3.2.2). In the present work, PDMS has also been used to cap SU-8 biochips (Section 3.2.4).

Hot Embossing

Hot embossing is a technique to replicate microfluidic devices using a silicon master on a polymer plate that can be used for mass production of biochips. Hot embossing is stamping of a pattern into a polymer softened by raising the temperature of the polymer just above its glass transition temperature [44]. First, the master used to define the pattern in the polymer is made by microfabrication on silicon. Then it is bonded to thick pyrex by using anodic bonding or a layer of epoxy so as to give a good support during the embossing process. Several types of polymers have been used for this process, including polycarbonate (PC), polypropylene (PP) and PMMA. After making the master, it is placed on top of the polymer blank with the pattern towards the polymer (Figure 3.2.3).

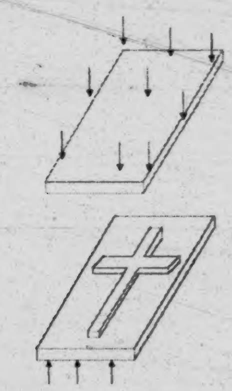

Figure 3.10: *Schematic of the Hot Embossing process after fabricating the master.*

A hot embossing machine is used to apply uniform pressure and temperature above the transition temperature of polymer. While applying the force, the master-polymer set is cooled down to just below transition temperature to stabilize the polymer microstructure. Another polymer plate can be bonded on top of the polymer plate with open microchannels.

We used the silicon masters and PMMA as the polymer. During the embossing process, the substrate-PMMA sandwich was heated to the PMMA glass transition temperature (105°C) and a pressure of 10^6 N/m^2 was applied. The system was cooled down below 105°C.

In the first process, the master was bonded to the pyrex with anodic bonding [98]. After the hot embossing process, the master and PMMA could not be separated easily so we tried to remove it by applying extra force. This caused the master to shatter. The remains of the master and the PMMA plate are shown in Figure 3.11(a) and Figure 3.11(b) respectively. In the second process, the master was bonded to a pyrex plate by epoxy and the hot embossing

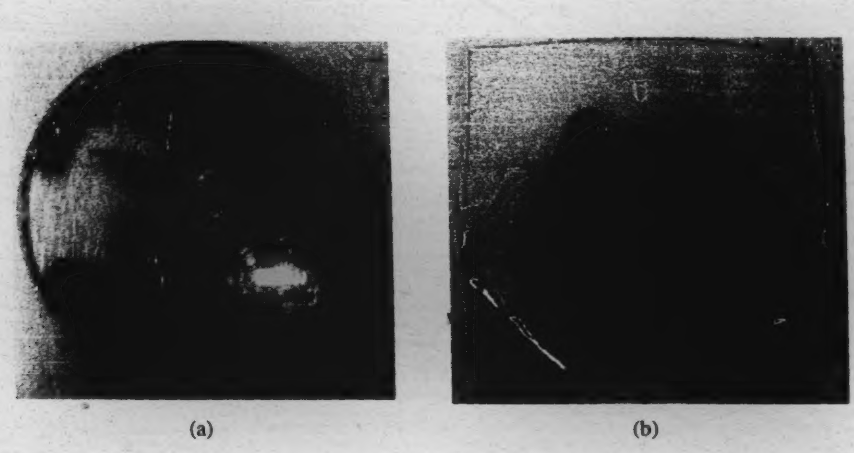
(a) (b)

Figure 3.11: *(a) The master after hot embossing is performed. In this case, the silicon master was bonded on pyrex by anodic bonding, (b) PMMA plate after hot embossing is performed. In this case, the silicon master was bonded on pyrex by anodic bonding before hot embossing. Several parts of the silicon masters were remaining on the plate.*

process was repeated. This time the master and the PMMA plate were separated easily but while removing them the PMMA plate was broken. In both processes, the PMMA plate was bent and the pattern of the nuts and bolts holding the silicon master and PMMA were on the plate. In the second process, the channels were embossed but, due to the bending and breakage of the plate, it could not be used.

Some improvements are necessary to realize good devices from PMMA by hot embossing. There is a need to improve the hardware system which holds the master as well as the PMMA plate. Also, the process steps during hot embossing are need be characterized for optimum results. The masters can be fabricated by less fragile materials such as nickel [44].

3.2.4 Direct Device Fabrication on SU-8

The photoresist , SU-8 ([99]), is a negative, thick, epoxy based, high aspect ratio resist. It finds application in several MEMS areas, including microfluidics for SU-8 microchannels and rapid prototyping with PDMS. SU-8 is a UV sensitive resist which can be spin coated in a conventional spinner in thicknesses ranging from 1 μm to 300μm. SU-8 has been used in different microfluidics processes due to its high sensitivity, fairly good adhesion properties, and relatively simple processing [83, 100].

SU-8 has very suitable properties of thickness and chemical stability, and has some good mechanical and optical properties. However, despite all these advantages, the SU-8 photoresist suffers from some disadvantages, namely adhesion selectivity, stress, use of solvent-based developer and resist stripping [82].

SU-8 has quite low molecular weight and thus when non-crosslinked can easily be dissolved by a number of solvents. SU-8 is patterned using a mask that blocks light in locations that should have SU-8 removed (such as microchannels). The process steps involved in fabricating SU-8 opto-biochips is discussed in Appendix D.

Mask design

In the present research, the SU-8 was used to fabricate opto-biochips on soda-lime glass. A picture of the mask with different chip designs are shown in Figure 3.12. As the index of refraction is 1.59, it can be used as a waveguiding material where the index of refraction of the surrounding material is less than 1.59. Here the dark part is chrome in the mask, so the corresponding region of SU-8 will be washed away after developing. Each chip consists of several sets of incoming and outgoing waveguide designs. The design motivation is discussed in Section 5.1. Points A to E in Figure 3.12(a) and points F to H in Figure 3.12(c) are discussed next.

Fabrication results

Figure 3.13 shows the microscope picture of different points of the SU-8 chip design as shown in Figure 3.12(a) and Figure 3.12(c). In this figure, pictures A to E are different parts of the Y-shaped biochip which are identified in Figure 3.12(a). The picture A shows the Y-junction of the biochip and B is the point joining the reservoir to the main channel. Picture C shows the circular shape of the reservoir. Picture D gives a clear view of the waveguide and microchannel intersection. A picture of the waveguide splitting and mixing region is shown in E. Images F, G and H in Figure 3.13 represent different parts on biochip fabricated for circulating electroosmotic flow (Figure 3.12(c)).

Figure 3.14(a) shows a contact profilometer scan across the microchannel of SU-8 on glass substrate, which shows the depth of the microchannel to be approximately 42 μm.

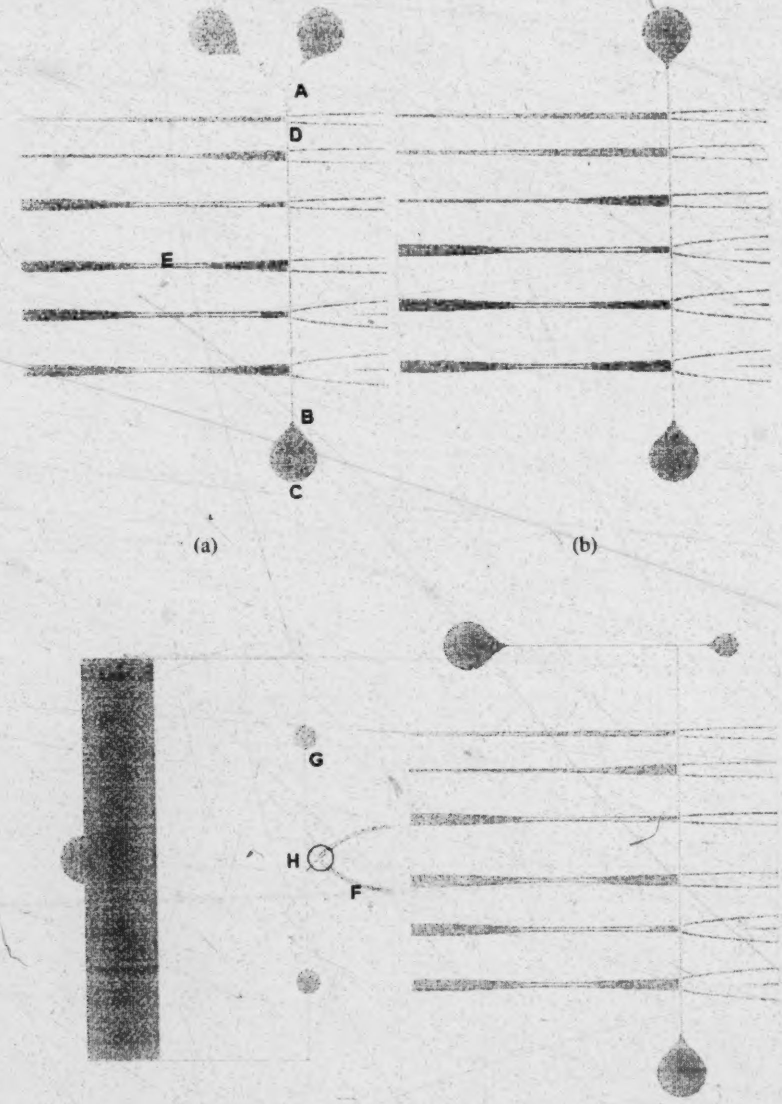

(a) (b)

(c) (d)

Figure 3.12: *Different chip designs on the mask (a) Y-shape channel and intersecting waveguides, (b) straight channel and intersecting waveguides, (c) for continuous electroosmotic flow, and (d) t-shape channel and intersecting waveguides.*

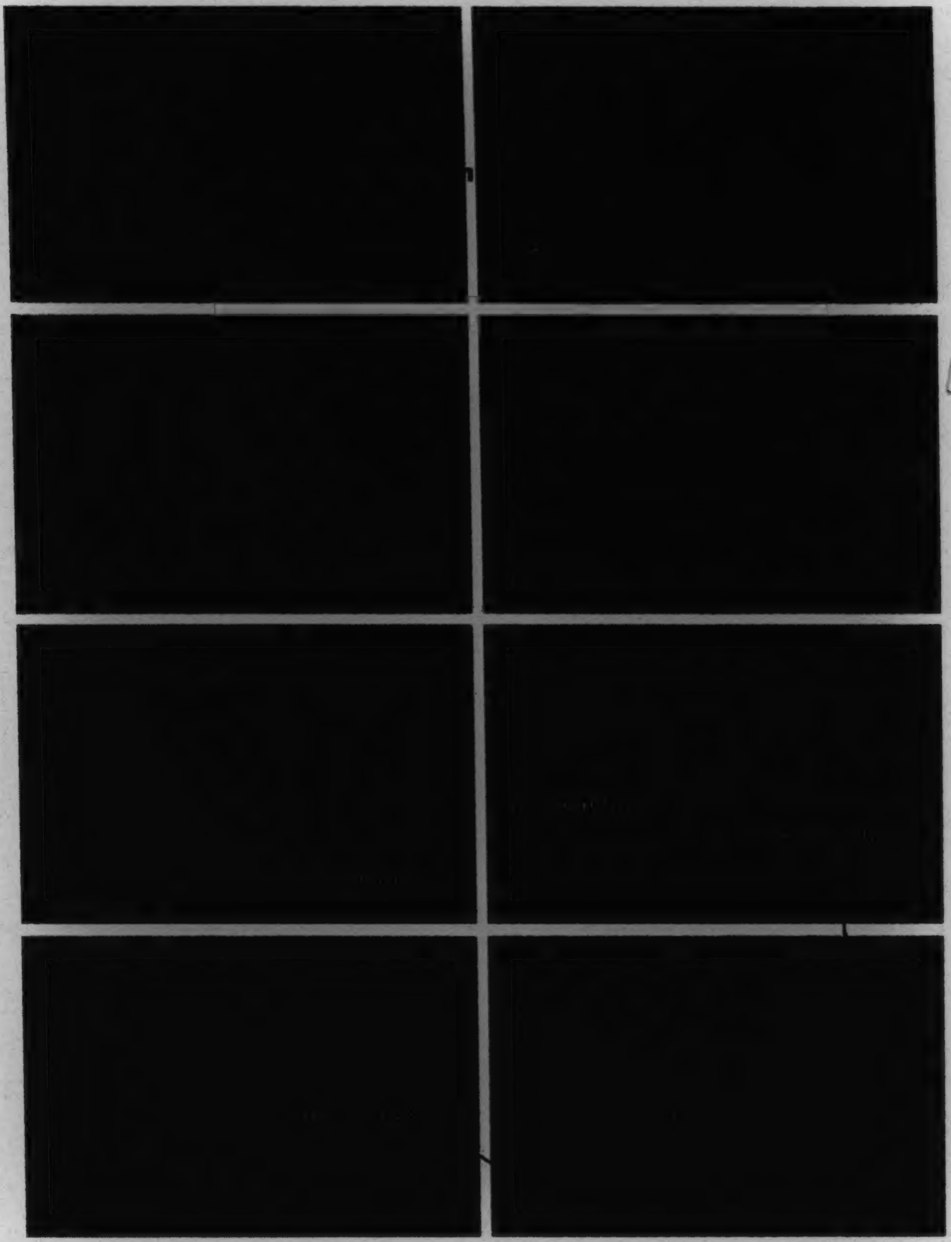

Figure 3.13: *Different parts of Biochip fabricated by SU-8 on glass as described in the text below and represented on the chip in Figure 3.12.*

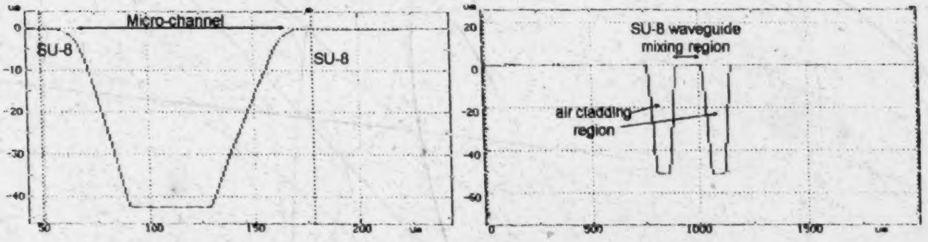

(a) Microchannel with SU-8 walls.

(b) The mixing waveguide region with air cladding as shown in Figure 3.13 (E).

Figure 3.14: *Picture showing the scan taken by a contact profilometer on glass substrate with SU-8.*

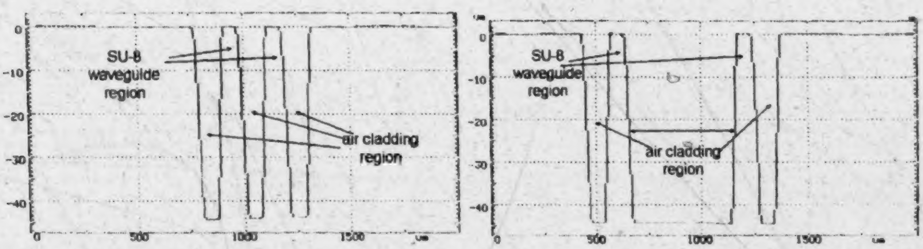

(a) Center-to-center distance, 400 μm as shown in Figure 3.13 (D).

(b) Center-to-center distance, 600 μm

Figure 3.15: *Picture showing the scan taken by a contact profilometer of two input waveguides in SU-8 with air cladding.*

This picture shows non-vertical sidewalls although it is not possible to get a clear sidewall shape using a contact profilometer due to the limitations of the instrument. The dimensions of the mixing regions (Figure 3.13 (E)), are shown in Figure 3.14(b). Figure 3.15(a) and Figure 3.15(b) show the dimensions of two input waveguides with air cladding with center-to-center distance equal to 400 μm (similar to Figure 3.13 (D)) and 600 μm respectively. With proper care during SU-8 processing and following proper procedures (Appendix D), the desired depth and structures were achieved.

Chapter 4

Optical Detection I - Microcapillary, Ion-exchanged and PDMS biochips

Detection methods in microsystems are essential to identify and quantify cells or chemical species that are being analyzed. A high-performance detection system is very important due to many fluidic functions and biochemical protocols being implemented on a small platform. A detection system should be chosen based on factors such as sensitivity, sample volumes and scalability to dimensions comparable to the microchips for miniaturization of the whole device [23, 56].

The study to track and measure the velocity of microparticles within flowing streams is of great interest and importance in industrial, medical and biological systems. Some of their applications are in the measurement of the effect of various interventions on regional blood flow and the study of fuel injection in combustion engines [101, 102].

Different techniques have been used to investigate flow of fluids in systems including microchannels. A common technique to measure particle velocity is based on the Doppler shift [103]. Particle Image Velocimetry (PIV) is another well established technique used to measure fluid velocity fields in both macroscopic and microscopic flow systems [104]. For velocity measurements of fluorescent microspheres in microfluidic channels the Shah Convolution Fourier Transform Detection (SCOFT) has been used [105].

In this chapter, fluorescent particle detection experiments in a microcapillary and a glass biochip are described. In the first approach, a plastic optical fiber launch-and-detect tip was devised. The velocity of microparticles was measured by knowing the spatial response of the tip and the dynamic response of moving microparticles (in a pressure-driven flow) in a glass capillary. In glass biochips with ion-exchanged waveguides, the input waveguide excites light at the two points in the microchannel. This double-peak in the fluorescence signal from each moving particle (in electroosmotic flow) is used to measure their velocities.

4.1 Optical Detection in Glass Capillary by Plastic Optical Fiber [1]

A photomultiplier tube (PMT) detection system was used to optically detect fluorescence microparticles in a micropipette (see Section 1.3.3). This system uses commercially available 1 mm plastic optical fiber to transport probe light to the biochip and return the fluorescence emitted to a computer-controlled PMT.

4.1.1 Launch and Detect Tip using Plastic Optical Fiber

At first, to deliver light to the microparticles, laser light was focused directly onto the microchannel and the collecting fiber positioned nearby. This method was abandoned as two alignments are required and there is a possibility for laser light directly entering the fiber and adding to the background signal in the PMT.

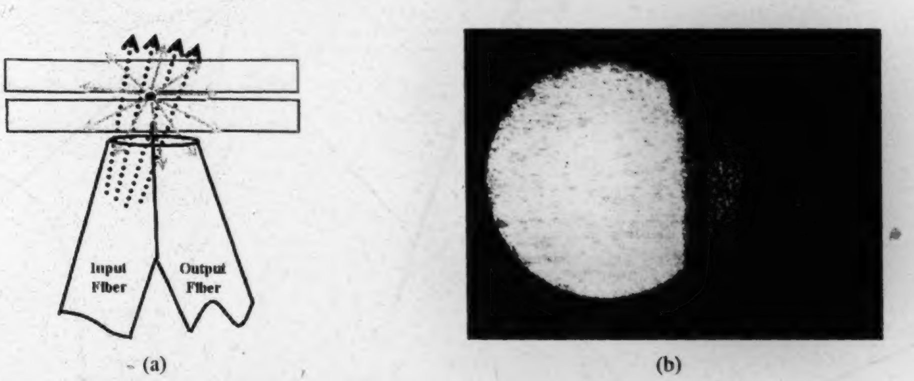

(a) (b)

Figure 4.1: *(a) Schematic of the launch-and-detect plastic optical fibers head, and (b) Incoming and outgoing light from a launch-and-detect tip.*

---

[1] The work presented in this section has been published in an earlier paper [64].

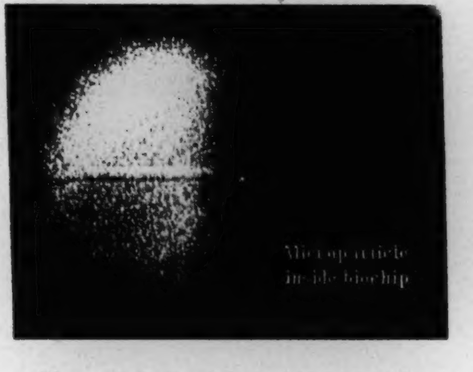

Figure 4.2: *Particle inside a biochip.*

In a more convenient method, a launch-and-detect tip was made by grinding and polishing the sides of two plastic optical fibers (POFs) at a small angle (10^o) to expose their cores with 1mm diameter. This tip physically connects both fibers as shown schematically in Figure 4.1(a). used in the detection of microparticle fluorescence. The exposed cores of the fibers were placed in contact and the POFs were inserted into a plastic syringe tip to hold them together. The tip was trimmed so as to be flush with the ends of the fibers and the exposed core ends were polished. The dotted arrows in Figure 4.1(a) indicate probe light, and the gray arrows indicate fluorescence from the microparticle (black dot).

The input fiber illuminates a region of the microchannel approximately 1 mm in size and the output fiber collects emissions from the same region. In this arrangement, only one spatial alignment on the order of 100 μm is necessary. An advantage is that laser light does not shine directly on the pick-up fiber and only light that is emitted from the microchannel enters the detection system. Figure 4.1(b) shows the incoming and outgoing light from a launch-and-detect tip. The bright semicircular patch on the left is laser light emanating from the tip and the dark receiving half of the tip is visible on the right.

The spatial response of the POF tip was characterized by measurements of fluorescence from stationary microparticle at a fixed position in a biochip. The microparticles used were 15 μm scarlet $FluoSpheres^{TM}$ from Molecular Probes [70] that have an absorption maximum at 651 nm and emission maximum at 680 nm. The optical filters used were thin film interference filters with a 10 nm pass band centered at 700 nm. The launch-

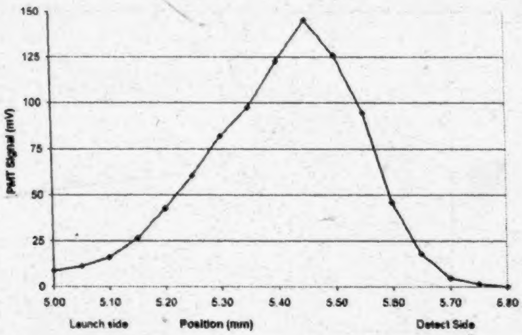

Figure 4.3: *Spatial response of the POF with stationary particle in the biochip.*

and-detect (POF) tip, placed under the biochip, emits light from the laser (0.5 mW, 630 nm semiconductor laser) and captures fluorescence from the stationary microparticle. A photograph of the assembly placed under a biochip carrying the microparticle (the white dot) is shown in Figure 4.2. After coupling losses, attenuation, and reflections at the biochip, the measured optical power at the top of the biochip was approximately 0.2 mW. Assuming that this is the power in the center of the biochip at the level of the microparticle and that the excitation beam is approximately 1 mm in diameter, the power incident on the microsphere is approximately 50 μW.

The background signal from ambient light with no laser illumination was approximately 15 mV. When no particle is present but the laser illuminates the biochip, the background signal (including scattered light from the laser) increases to approximately 45 mV. To find the spatial response of the POF, the biochip and microparticle were moved a distance of 0.8 mm in 0.05 mm steps an dthe received power was recorded as shown in Figure 4.3. The maximum response from a single microparticle is approximately 150 mV after the background signal is removed, well above the noise level of a few mV, and a typical response measured with this setup.

4.1.2 Application to Velocity Measurement of Microparticles

To demonstrate how the detection system may be used for the velocity measurement, the fluorescent emissions from microparticles in a laminar flow were detected and their

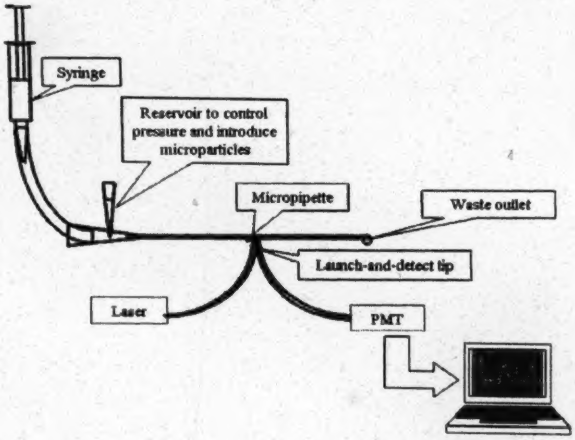

Figure 4.4: *Schematic of experiment to detect microparticles in flow through a micropipette.*

velocities calculated from the data. A cylindrical micropipette (200 μm diameter) was used as the channel and the flow was driven by gravity as shown schematically in Figure 4.4. The volume of flow and therefore the flow velocity in the pipette is proportional to the height of the liquid in the reservoir (syringe tip). The height of the reservoir (and the flow velocity) can be changed using the syringe attached to one side of the cylindrical micropipette[64].

A PMT scan of moving microparticles, at a gain of 10^7, over 30 seconds is shown in Figure 4.5. In this figure, the signal is based on averages taken after every 200 samples (0.02 s). There are 16 full particles with various velocities observed in this window.

Figures 4.6 shows the details of the responses above the background for the particles recorded at 19.7s and 22.0s. These two particles excite responses in the PMT of similar shape but on different time scales and are clearly moving at different velocities, the one at 19.7s moving approximately four times as fast as the one at 22.0s. The velocities of these particles was calculated by taking the ratio of the root-mean-square (RMS) pulse width in millimeters for the detector response in Figure 4.3 to the root-mean-square pulse duration in seconds of the particles derived from the sample data.

Let S(z) be the net signal above the background, where "position" z can be distance traveled (as in Figure 4.3) or time (as in Figure 4.6). First, a subset of data pairs $[z_i, S(z_i), i = 1, N]$ were selected corresponding to the signal from one particle and then

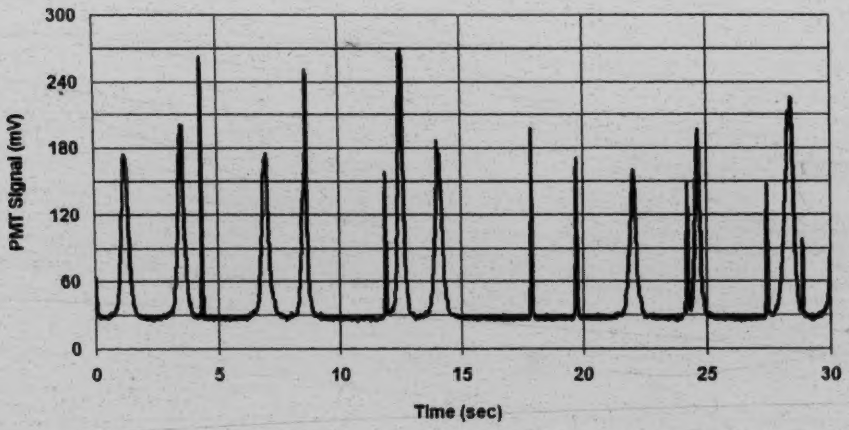

Figure 4.5: *Full PMT scan over 30 seconds for moving fluorescent microparticles in the micropipette. Each value shown is the average of 200 raw samples taken at 10 000 samples per second. There are 16 particles with various velocities observed in this window.*

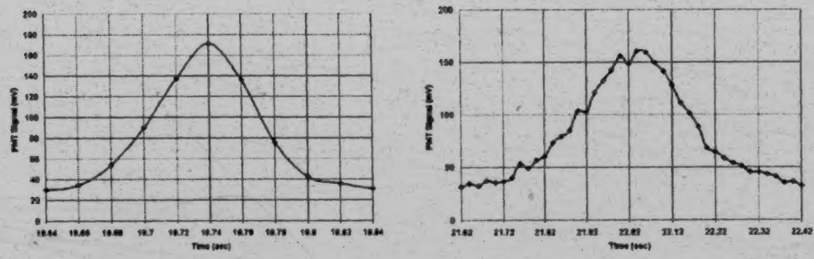

(a) Detail of the particle observed at 19.7s (b) Detail of the particle observed at 22.0s

Figure 4.6: *Detail of the different particles (not on scale).*

the values were normalized so that

$$\sum_{i=1}^{N} S(z_i) = 1 \tag{4.1}$$

The mean position of the pulse the mean-square duration of the pulse are defined as

$$\langle z \rangle = \sum_{i=1}^{N} z_i S(z_i), \tag{4.2}$$

$$\langle \sigma_z^2 \rangle = \sum_{i=1}^{N} (z_i - \langle z \rangle)^2 S(z_i). \tag{4.3}$$

From Figure 4.3, we find the RMS particle size in the detector to be 0.127 mm. The RMS pulse durations for the particles at 19.7s (Figure 4.6(a)) and 22.0s (Figure 4.6(b)) were 0.0302 s and 0.130s respectively. The corresponding particle velocities are 4.2 mm/s and 0.98 mm/s respectively.

4.2 Microparticles Detection in Ion-Exchanged Opto-Biochips [2]

4.2.1 Fluorescence from Dye in the Microchannel

Opto-biochips with ion-exchanged waveguides [60] were used to detect fluorescence from a dye and from microparticles. Propagation of light in one opto-biochip is shown in Figure 4.7(a). This opto-biochip has a 2 cm long microchannel and two reservoirs. One waveguide, splitting into two parts is able to shines light at two point of the microchannel. Light (0.50mW) from a 630 nm laser is launched at the entrance of waveguide through a microscope objective (visible at the bottom part of Figure 4.7(a)). The light was split into two waveguides and intersected with straight microchannel at two points, A and B. The separation between these two points is 5 mm.

---

[2] The work presented in this section has been published in an earlier paper [61].

This biochip was used to observe the fluorescence signal from the Nile Blue dye (Nile Blue 690 from Exciton Inc., Dayton, OH). This dye has an absorption peak at 628 nm and an emission peak at 660 nm. The dye was injected into the microchannel through one reservoir and flows into the channel by capillary action. The emitted fluorescence was captured by a 1 mm plastic optical fiber positioned on top of the chip and delivered to the PMT. The pickup fiber was moved along the microchannel across the two intersections, A and B.

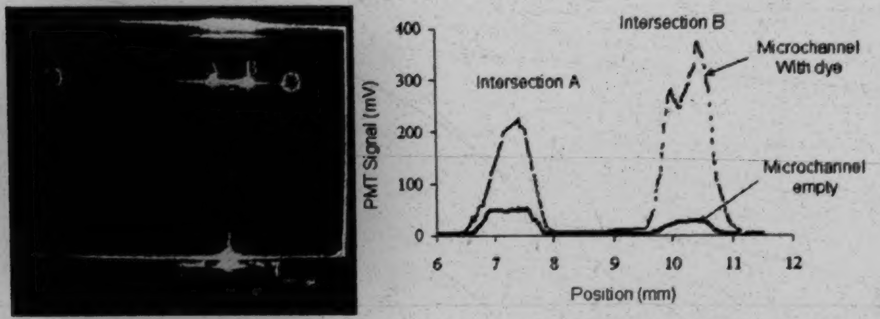

(a) Light guidance inside an ion-exchanged opto-biochip having a microchannel with an intersecting waveguide splitter.

(b) PMT signal from empty and dye-filled microchannel.

Figure 4.7: *Propagation of light through the waveguide splitter and PMT signal scattered from microchannel.*

Figure 4.7(b) shows the variation of the intensity of the light (PMT signal) emitted from the channel. The maximum PMT signal from the empty microchannel was approximately 50 mV. After the dye solution was injected, the PMT signals were increased approximately 5-10 times. The difference in peak signal at intersection points is due to the fast evaporation of dye at intersection B, which is closer to the reservoir.

4.2.2 Anomalous Etching of the Ion-Exchanged Glass

The details of the fabrication of field-assisted ion-exchange waveguides in glass substrates have been reported previously [58, 59]. An anomaly in the microchannel etching process caused the waveguides to be deformed at the waveguide-channel interface resulting in the formation of irregularly shaped side-channels. A SEM image of one such intersection, before bonding the glass cover plate, is shown in Figure 4.8(a). These etched side-channels have a significant effect on the delivery of light into the channel. This will be discussed in Section 4.2.3.

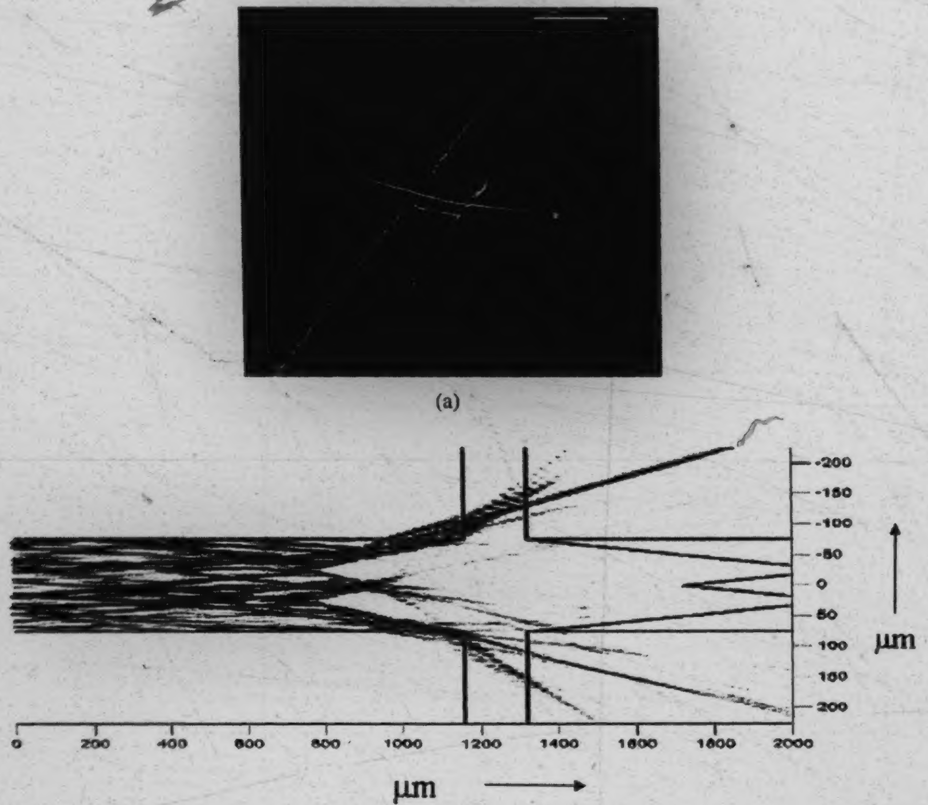

(a)

(b)

Figure 4.8: *(a) SEM image before bonding of the glass cover plate, and (b) Two-dimensional beam propagation simulation showing the split of waveguide light into two distinct beams in the microchannel.*

Figure 4.7(b) indicate strong coupling between the waveguides and the channel despite the anomalous etching of the ion-exchanged glass. A two-dimensional (2D) multimode beam propagation method (BPM) simulations were carried out to verify how the irregular shape and optical index profile of the waveguides and side-channels behave. Figure 4.8(b) shows a plot of the 2D intensity pattern of the light as it propagates first along the waveguide and then through the side-channel and main channel. The splitting of the light into two distinct beams in the channel on either side of the intersection is clearly visible. This demonstrates how the anomalous etching of the glass could produce a double peak effect, which will be discussed in the following section.

4.2.3 Electroosmotic flow, Microparticle Detection and Velocity Measurement

Electroosmotic flow (Section 2.1.2) of microparticles was observed in a laminar flow inside a biochip fabricated by ion-exchange method by Hong Qiao (MSc 2003) [60] (Section 1.3.3). Figure 4.9 shows the schematic of the experiment conducted to see electroosmotic flow in a 2 cm long and 157 μm wide microchannel.

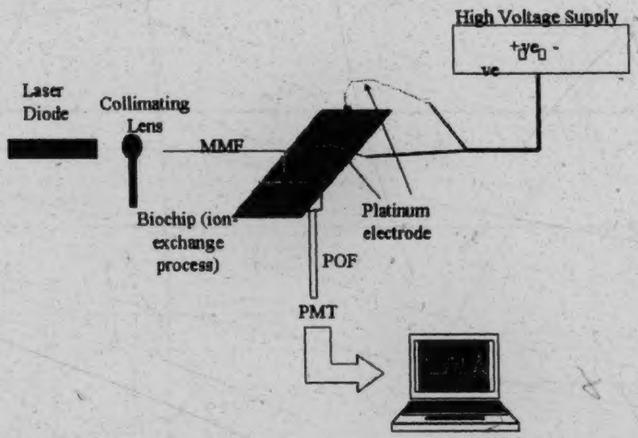

Figure 4.9: *Schematic of experiment to move and detect microparticles by electroosmotic flow inside biochip*

Light from a laser diode was launched at one end of the waveguide through a 50 μm core multimode fibers. Two platinum electrodes, connected to a high voltage power supply, were used to apply an electric field along the microchannel. Figure 4.8(a) shows the SEM image of the waveguide. When a fluorescent particle passes the intersection it emits two bursts of light intensities as discussed next. Movement of microparticles due to EOF can be seen even at voltages as low as 20 V.

Determination of Velocity of Moving Particle

In the present method, the velocity of the particles was measured by fluorescence detection in the PMT. By analyzing video sequences taken through a microscope, the velocity of the flow was measured and the distance between the double peaks of light intensities was determined. The velocity in subsequent experiments was determined by measuring the time taken by particle in flowing between double peaks.

Figure 4.10 shows eighteen frames spaced 1/3 s apart taken from a video sequence of a downward-moving microparticle passing the intersection under a driving voltage of 50 V. The particle lights up just before it reaches the intersection, turns off and lights up again just after leaving the intersection. This sequence is taken from the first part of a video that records two particles that pass the intersection downward, then again upward after the polarity of the 50 V driving voltage is reversed. This procedure was repeated for driving voltages of 100 V, 200 V, 300 V, 400 V and 500 V.

Figure 4.11(a) is a screenshot of the LABView program 15 seconds signal window based on averages that were taken after every 150 samples (0.015 s). Details of the PMT signal (at a gain of 10^7) net responses above the background from two particles that pass through the intersection in both directions are shown in Figure 4.11(b). Each particle produces two peaks as it passes thorough the intersection in one way movement which can be explained if the laser light has two intensity peaks near the waveguidechannel intersection. When both particles have two way movement, corresponding to one voltage we get eight peaks. The graph for six different voltages is shown in the Figure 4.11.

An expanded view of the double passing of two microparticles at 50 V is shown in Figure 4.12. This double peak can be used to measure the flow velocity.

Determination of Velocity of Moving Particle by Captured Video

While capturing the signal with the PMT, the video was recorded. By analyzing the video sequences, the speed of the flow can be measured and the distance between the peaks can be determined in the following manner. This was done first converting the video corresponding to one particular voltage to a sequence of frames. The time difference

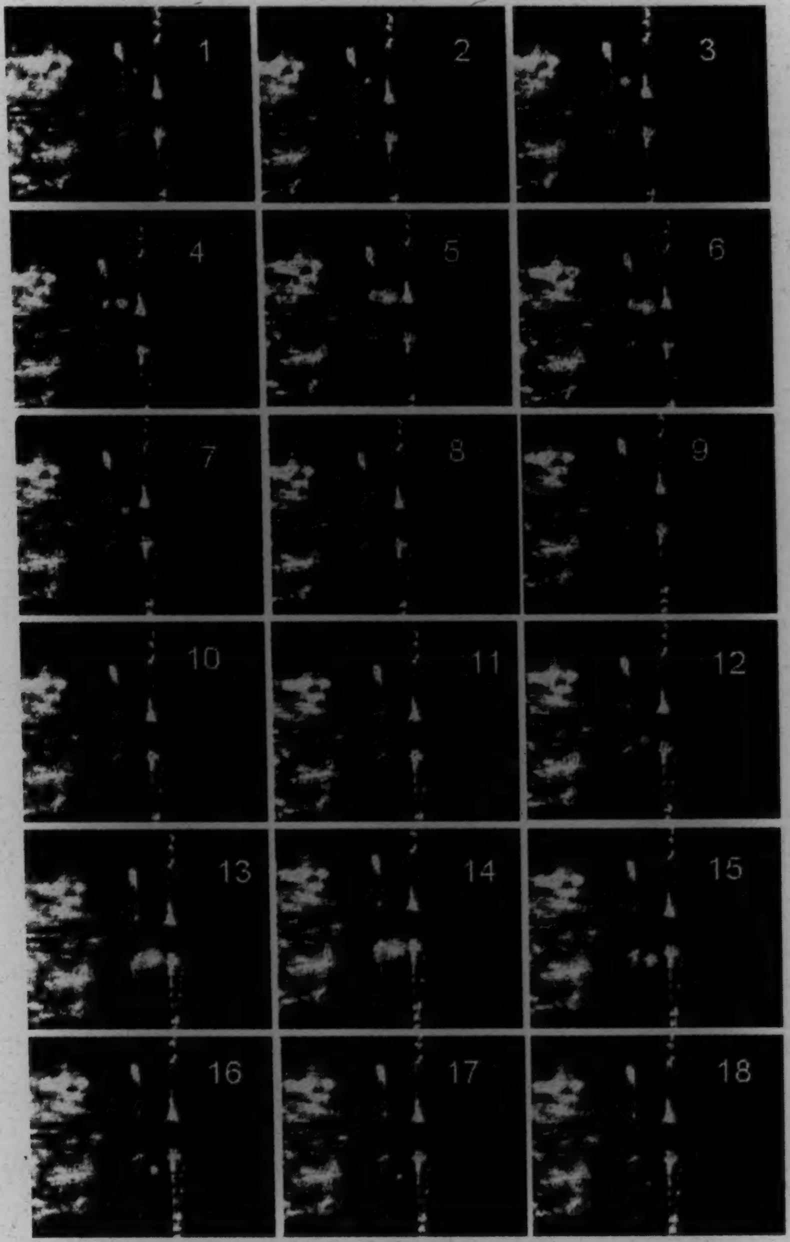

Figure 4.10: *18 frames showing movement of one fluorescent microsphere in a electroosmotic flow at 50V. Frames in this picture are 1/3 s apart. Laser light from the waveguide on the left illuminates the microchannel. The fluorescence is brightest in frames 6 and 14.*

(a) A computer screenshot of LABView program.

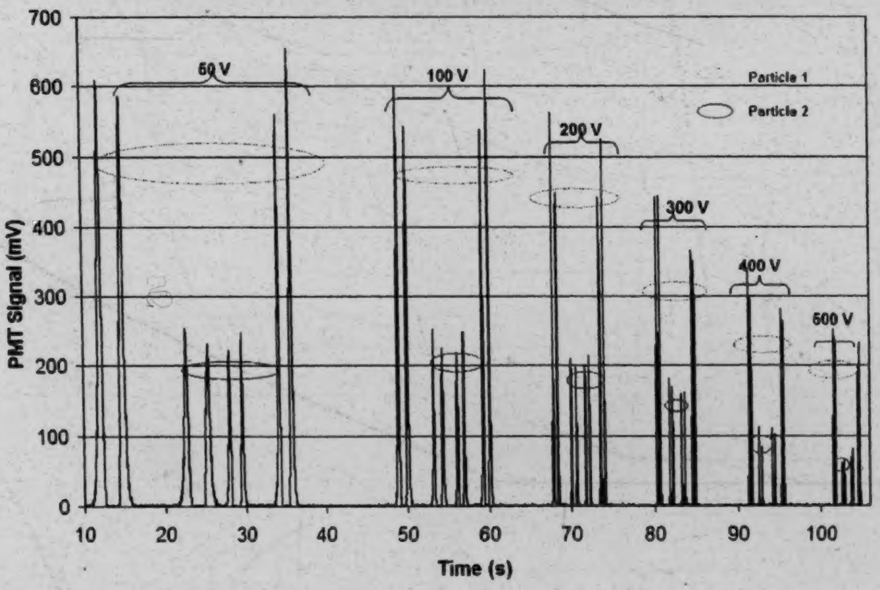

(b) PMT signal at different voltages.

Figure 4.11: *Detection of two particles in two direction at different voltages passing through microchannel-waveguide intersection.*

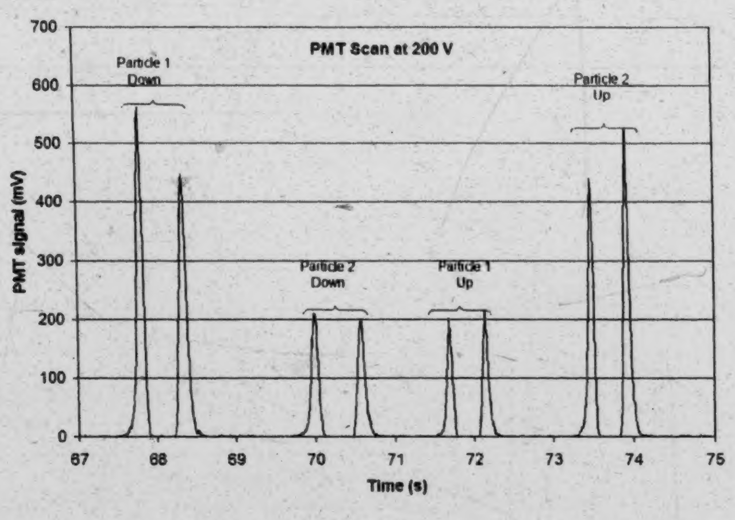

Figure 4.12: *Scan through the PMT at 200V showing movement of two particles.*

between each frame was 1/30 s. Knowing this, number of frames taken while going between two points in the channel can be found. This way we could find the velocity of particles related to a certain voltage. The velocity of two particles related to different voltages show a linear graph, which is shown in Figure 4.13(a).

Determination of Velocity of Moving Particle by PMT Scan

After finding the velocity by a sequence of frames, the velocity at 50 V was used for the calibration. The velocity at 50 V was assumed to be most accurate. This is because there are more frames captured at 50 V due to slow movement of particle which lead to less error in determining the time taken in moving between two points in the microchannel. From the PMT data graphs, we can find the time taken in passing two peaks at 50 V. This way, we calculate the distance traveled between the peaks in the PMT signals.

Another way to calculate the distance traveled by microparticles is to measure the width of the microchannel by a microscope and using this width as a scale to measure distance traveled by microparticle. The width was found to be 157 μm, so the change in the position of the first particle over a 250 frame period, or 250/30 s, was found to be 418 μmm for a velocity of 49 μm/s. Similarly, the second particle traveled a distance of 267 μm in 170

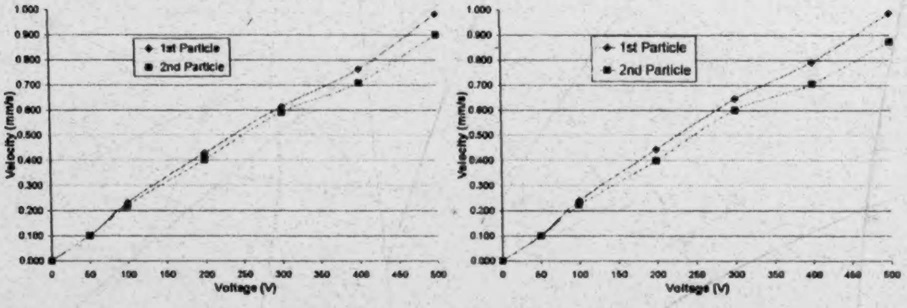

(a) (b)

Figure 4.13: *Graphs showing the variation of two particles velocity with applied voltage. (a) by video frames (b) by PMT scan.*

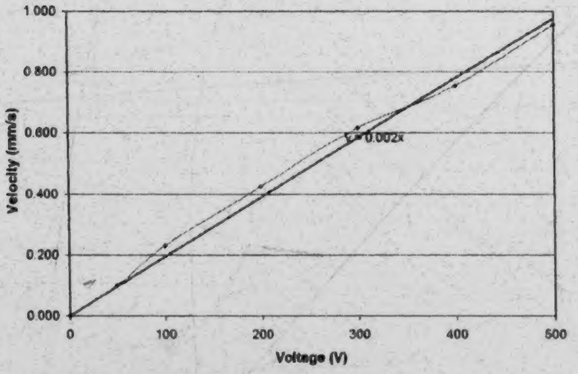

Figure 4.14: *Graph showing the variation of velocity with applied voltage. Here, velocity is the average of the velocities of two particles measured by the two different methods.*

frames with a a velocity of 46 μm/s. From the PMT signal data as shown in Figure 4.11(b), the times between peaks for these two particles were 2.80 and 2.77 s respectively, giving an average value of the distance between peaks of 136μm. The uncertainty in this calibration is estimated to be approximately 15% due mainly to the uncertainty in measuring the microchannel width from the image retrieved from the video sequence and the positions of the microparticle at the start and end of the sequence.

After calculating the distance between peaks, the velocity at subsequent voltages can be immediately determined by using the distance between peaks and the time taken by particles in passing two peaks. Figure 4.13(b)shows an approximate linear graph of the velocity of two particles related to different voltages. The average of the velocities of both particles by two different methods as described above is given in figure 4.14. The velocity for this microchannel has been calculated using equation 2.19, and was found to be 174 $\mu m/sec$ at 200 V, which is less than the velocity measured from the above method. This can be due to a possible hydrostatic pressure difference due to the liquid in the reservoirs. From equation 2.16, it is clear that even a 1 mm pressure difference, can produce a maximum velocity of approximately 150 $\mu m/sec$ at the center of a 50 μm deep microchannel. The existence of the hydrostatic pressure difference can lead to a higher velocity of the moving microparticles [74].

Figure 4.14 shows a linear relation between velocity and applied voltage as reported in [106], within the estimated 15% uncertainty. This method measures the particle velocity, not the true fluid velocity as measured in [106]. The particle velocity may be different if there is a surface charge on the microparticle which would lead to an electrophoretic drift relative to the background fluid [68, 74].

4.3 PDMS Biochips

PDMS biochips were fabricated by casting PDMS on a laser-written master. Later, the PDMS layer was peeled off and irreversibly sealed on a plain microscope glass (Section 3.2.3). As discussed in Section 3.2.3, the PDMS has surface properties similar to glass so the electroosmotic flow can be done [45].

4.3.1 Electroosmotic Flow

The experimental setup to observe the electroosmotic flow in the PDMS biochip is shown in Figure 4.15. This biochip has a T-shaped microchannel with total length of 3 cm (from point A to B through the T-junction). The microparticles were injected from reservoir A and flow towards reservoir B. This direction of the flow of the microparticles can be reversed by reversing the polarity of voltage applied between two reservoirs.

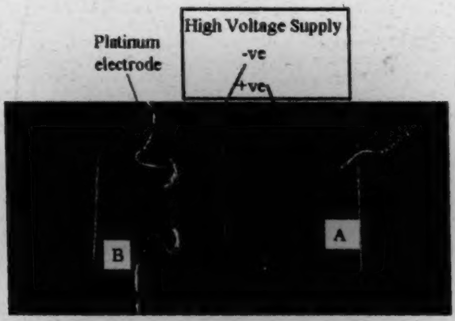

Figure 4.15: *Experimental setup for observing the electroosmotic flow (between reservoirs A and B) in the PDMS biochip.*

Figure 4.16 shows different frames captured from a video during the motion of one microparticle due to electroosmotic flow at 200V. In this figure the frames are 1/3 s apart. Figure 4.17 and Figure 4.18 show the frames captured at 500V and 1000V respectively. The position of the microparticle is encircled in all the frames.

The width of the microchannel was measured using the microscope and verified to be 100μm, the same as the master (Section 3.2.2). Now, the distance traveled by the particle during one frame (1/3 s) or several frames can be measured approximately and compared to the width of the microchannel. This was accomplished by choosing two points in the microchannel on the computer screen and measuring the distance between them with a simple ruler. This ruler measurement can be converted to a distance by comparing with the ruler width of the microchannel on the screen. The velocity can be determined by dividing the distance by time between frames between this particular distance.

From these figures, an observation of the position of the particle when the voltage is

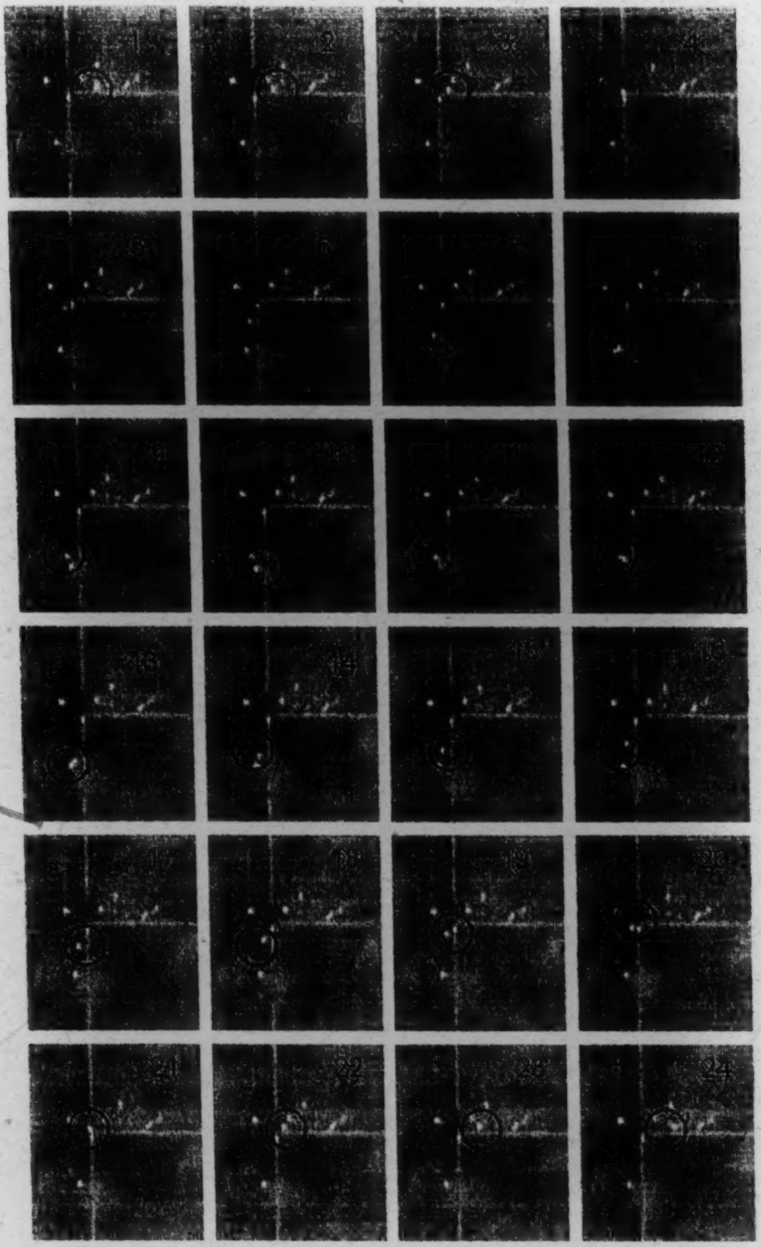

Figure 4.16: *24 frames showing movement of one fluorescent microsphere in a electroosmotic flow at 200 V. Each frame is 1/3 s apart. The particle position is indicated by a circle.*

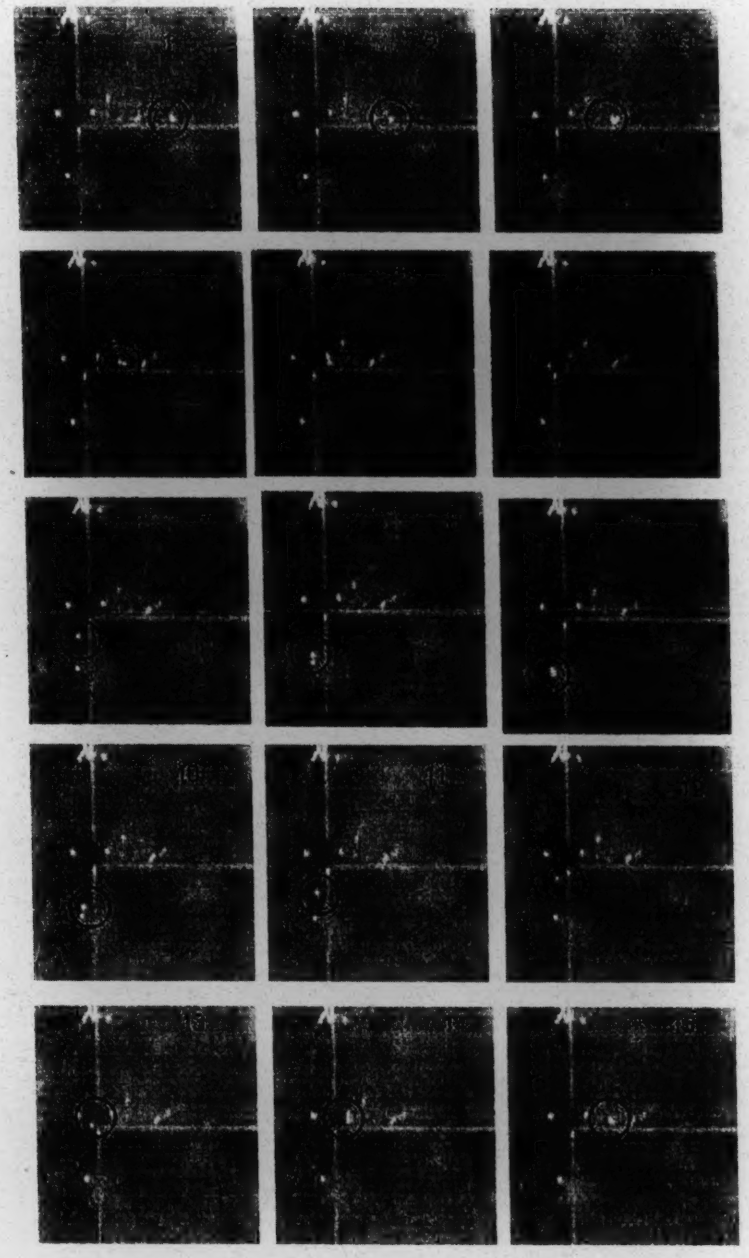

Figure 4.17: *15 frames showing movement of one fluorescent microsphere in a electroosmotic flow at 500 V. Each frame is 1/3 s apart. The particle position is indicated by a circle.*

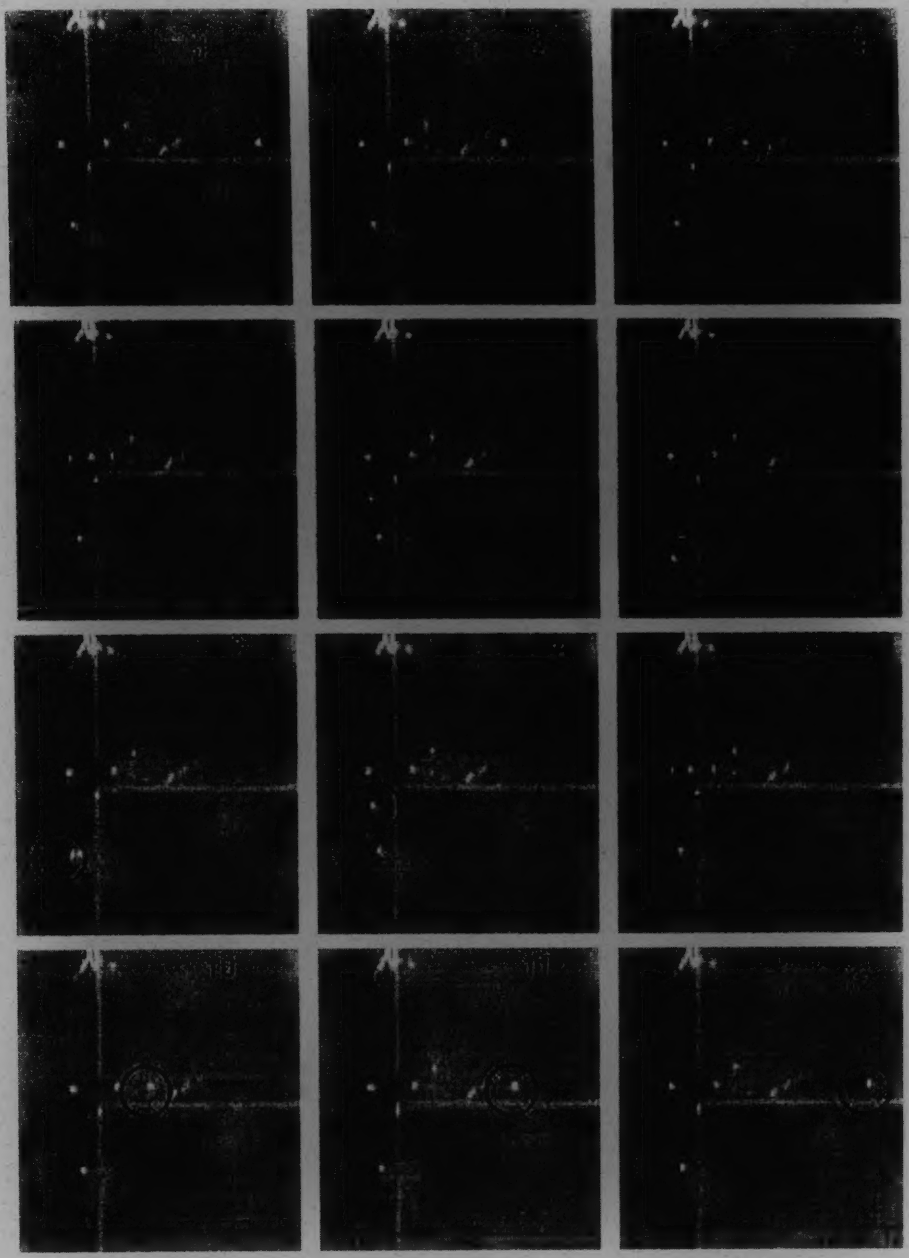

Figure 4.18: *12 frames showing movement of one fluorescent microsphere in a electroosmotic flow at 1000 V. Each frame is 1/3 s apart. The particle position is indicated by a circle.*

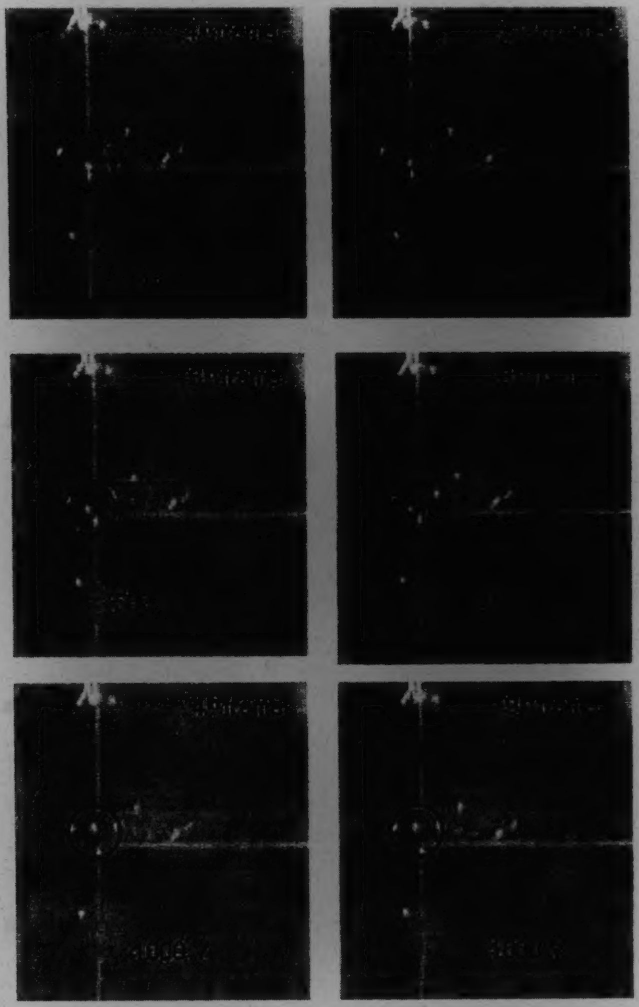

Figure 4.19: *Different frames showing movement of one fluorescent microsphere in a electroosmotic flow for different voltages around the corner. The bead position is indicated by a circle.*

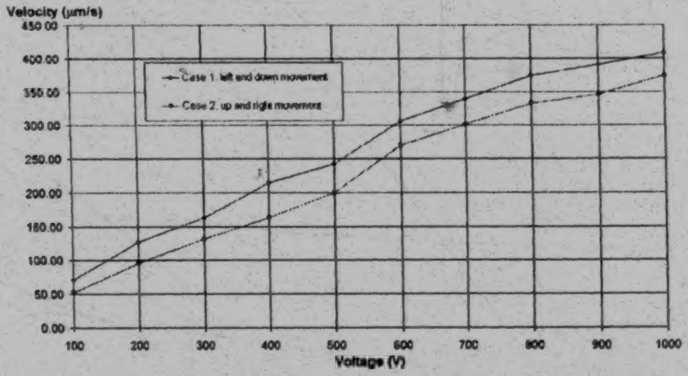

Figure 4.20: *Graph showing the variation of velocity with applied voltage in PDMS biochip.*

changed can be made. When the particle arrives at the T-junction, it moves further away from the corner when the applied voltage is increased. This can be seen from different frames in Figures 4.16(4th frame), 4.17 (6th frame) and 4.18 (4th frame) and in Figure 4.19. A similar effect can be observed for the cases when the flow of the particle is reversed. This is shown in different frames in Figures 4.16(21th frame), 4.17(13th frame) and 4.18 (9th frame) and in Figure 4.19. This can be explained by the fact that the velocity of the particle increases when the applied voltage is increased. When the velocities of the particles increase, there may be a dynamical effect due to centrifugal force away from the corner around which the particle turns [67] since these microparticles are denser than the background electrolyte [70].

Figure 4.20 shows the variation of the velocity of microparticle under EOF at different applied voltages due to the motion in two directions as in the glass biochips with ion-exchanged waveguides. The velocity is proportional to the applied voltage, which is clear from the equation 2.18. The velocity inside this microchannel (3 cm long) has been calculated using equation 2.19, and was found to be 110 $\mu m/sec$ at 200 V. The velocity in two directions were found to be different. This may be due to an additional component of pressure driven flow due to a difference in fluid depth in the reservoirs.

4.3.2 Electroosmotic Flow Switching

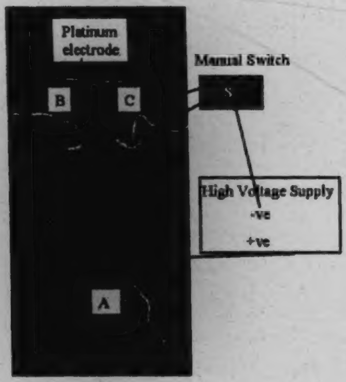

Figure 4.21: *Experimental setup for observing the switching of the electroosmotic flow in PDMS biochip.*

A similar experiment as shown in Section 4.3.1 was performed to observe the switching of the microparticle from main microchannel to the microchannels on the two arms of the T. The experimental setup is shown in Figure 4.21 where the microparticle is switched from A to either B or C by changing the negative polarity of the applied voltage from B to C using a manual switch S. The microparticles flow in reverse direction is observed by disconnecting the reservoirs from the high voltage supply and connecting the voltage by changing the polarity of the voltage in two reservoirs.

Figure 4.22 shows 9 frames of the video recorded while observing the switching of the microparticle at 500 V. These frames are 2s apart. Each frame shows the position of the microparticle and the polarity of the applied voltage. During frames 1, 2 and 3, the particles flows from side A to C and its flow is reversed by during frames 4 and 5. Now the negative voltage is applied at reservoir on the side B which makes the particle to flow from A to B (frames 6 and 7). The particle flows back towards A after reversing the voltage. This was the flow of the particle was switched from A to either B and C.

This way, the switching of the flow of the microparticles flowing in an electroosmotic flow was demonstrated. The switching is a critical element for a cell-sorter as described in Section 1.1.2.

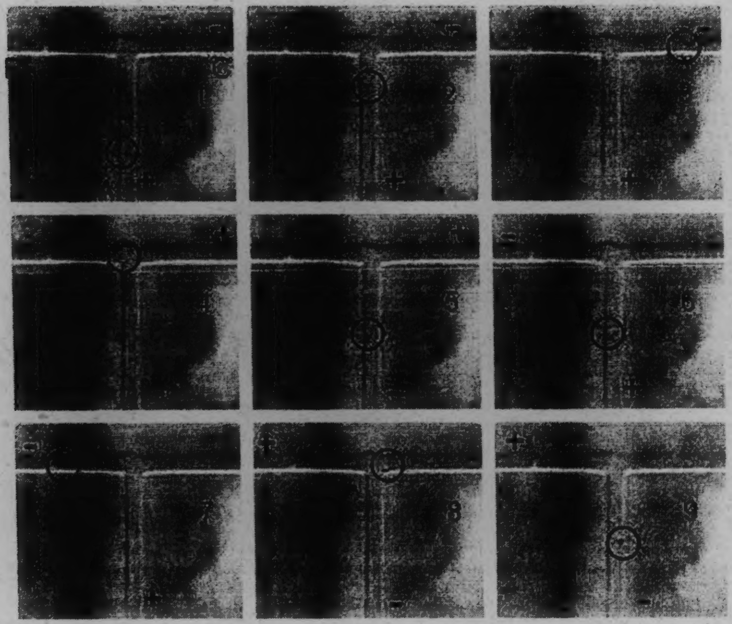

Figure 4.22: *9 frames showing the switching of fluorescent microsphere in a electroosmotic flow at 500 V. Each frame is 2 s apart. The bead position is indicated by a circle.*

Chapter 5

Optical Detection II - SU-8 Opto-Biochips

Realization of an optical detection system integrated with biochips is a current topic in μTAS research (Chapter 1). A few systems based on integrated waveguides have already been discussed in the previous chapter (Chapter 4). Although these methods provide a platform for optical detection and microchannel on same device, difficulty in fabrication and material selection was one of the major obstacles in achieving an opto-biochip. For the glass biochips with ion-exchanges waveguides the fabrication process was a two-step process and generated anomalous etching of the microchannel in the waveguide region. The PDMS biochips do not have potential to be used as a dielectric waveguide. One way to achieve waveguiding feature in PDMS biochips is guiding light in a hollow PDMS microchannel [107], however such hollow waveguides in dielectrics are too lossy. The hollow PDMS microchannels yields waveguides of low optical quality.

Researchers have been using polymers as a functional material for waveguides due to ease of fabrication and compatibility with basic microfluidic platforms [23, 56]. SU-8 is one such material which is already used extensively in fabricating microfluidic devices [45, 79, 83, 108]. Using SU-8 as an optical waveguiding element was first reported by Curtis *et al.* [109] and later used in different micro-optical applications [110].

This chapter presents the characterization of an opto-biochip, in which both a fluidic system as well as optical waveguides are fabricated on glass in one processing step [111]. The fabrication process is shown in Appendix D and was discussed in Section 3.2.4. The devices can be fabricated, packaged and tested in half a day.

5.1 Design Motivation

One of the major considerations for flow switching (Section 1.1.2) is achieving the exact time of switching, which can be measured by finding out the velocities of moving microparticles. Here we employed a similar method used in our earlier research [61, 64], discussed in Section 4.2. There, the velocity was measured using the double peak formed by anomalous etching at the waveguide-microchannel intersection. The double peak formed by this method was unexpected from the initial design but provided a way to measure velocity. While this method provides a simple and accurate method to measure velocity, it has the drawbacks of a cumbersome fabrication process, and an unpredictable peak-to-peak distance which depends on the etching process of the microchannels.

In the present work, we have designed waveguide-microchannel intersections such that a double peak is formed with pre-decided peak-to-peak distance. Also, light of two different wavelengths can be propagated in these biochips to detect two microparticles having emission spectra corresponding to these wavelengths. Velocities of the moving microparticles can be measured directly from the spacings of the captured fluorescence signals.

Two different types of light propagation systems are designed in this work, with different dimensions as shown in Figure 5.1. In the first system (Figure 5.1 (a)), the input section of the waveguide splits into two waveguides which shine light at two points of the microchannel. The input section in the second system, called the "mixer-splitter section", consists of two different input waveguides (1 and 2), combining (at point A) and then splitting (at point B) into two waveguides shining light at two points of the microchannel. This allows two wavelengths to travel along the waveguide at the same time (Figure 5.1 (b)). The microchannel and waveguide widths were chosen to be 100 μm and 50 μm respectively. The white region is the core (SU-8) and the dark region is air which acts as the cladding of the waveguides on the microchannel. For the output section of the waveguide, the cladding is made in a parabolic shape to improve the amount of fluorescence that is captured from moving microparticles. Figure 5.1 (b) is broken into three parts in Figure 5.2, which shows different dimensions of the mixer-splitter waveguide. The mixer-splitter region (Figure 5.2 (c)) consists of sections with different dimensions. The first

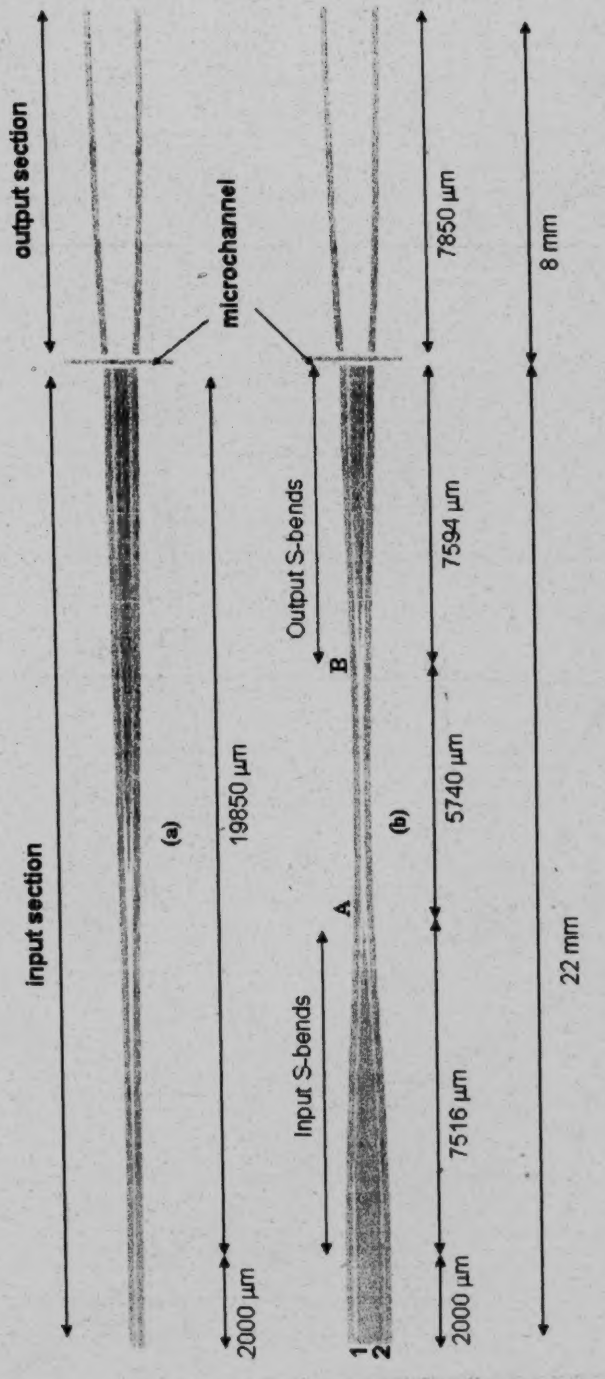
output section
input section
microchannel
(a)
19850 µm
2000 µm
Output S-bends
Input S-bends
B
A
(b)
1
2
7850 µm
7594 µm
5740 µm
7516 µm
2000 µm
8 mm
22 mm

Figure 5.1 : Two SU-8 waveguide designs.

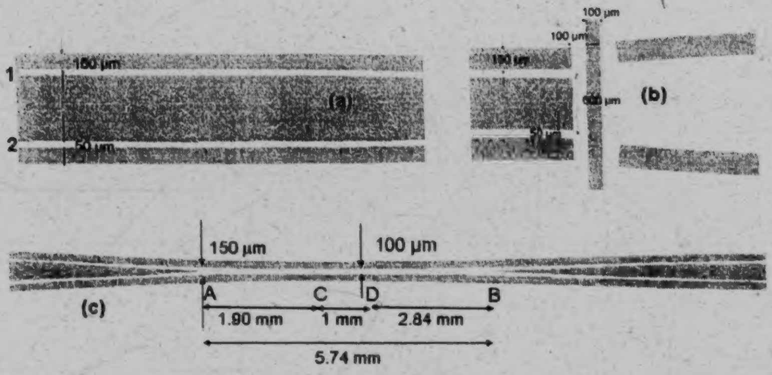

Figure 5.2: *Dimensions of different points of the waveguide microchannel combination. The white region is the core (SU-8) and the dark region is the cladding of the waveguides. (a) Start region, (b) Intersection region, where the two waveguides shine light on two points of the microchannel, (c) Middle region, where the two waveguides join together and again split into two waveguides.*

set of S-bends (starting in the right side as shown in Figure 5.2 (a)) end at point C and another set of S-bends start at point D. The waveguide width at points A and B is 150 μm which becomes 100 μm between straight section of waveguide between points C and D. The outer air cladding of the input section of the waveguide was 150 μm wide and the separation between microchannel and waveguide edge was 100 μm in the above cases.

5.2 Propagation Loss Measurements

The propagation loss in the SU-8 waveguides was determined by measuring the scattered light as a function of the position. Here, we have assumed that the scattering is proportional to the local intensity of the propagating light. Figure 5.3 shows the experimental setup used to study the optical performance of SU-8 waveguides. The loss measurements were carried out using the second type of waveguide as discussed in Section 5.1 and shown in Figure 5.1 (b).

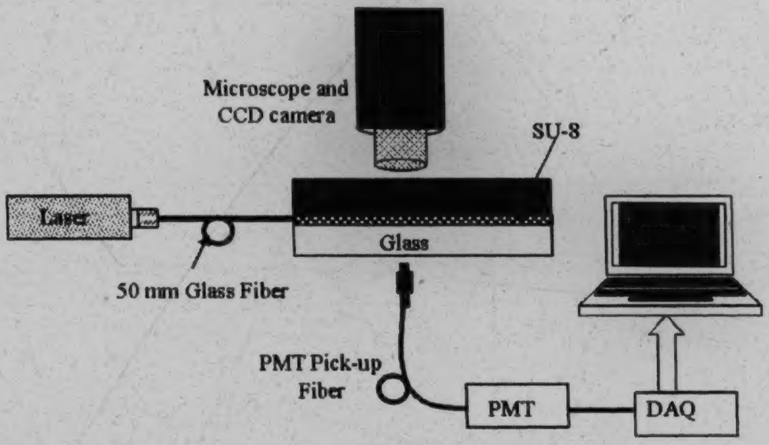
Microscope and CCD camera
SU-8
Laser
Glass
50 mm Glass Fiber
PMT Pick-up Fiber
PMT
DAQ

Figure 5.3: *Schematic diagram of the experimental set-up to measure loss in SU-8 biochip.*

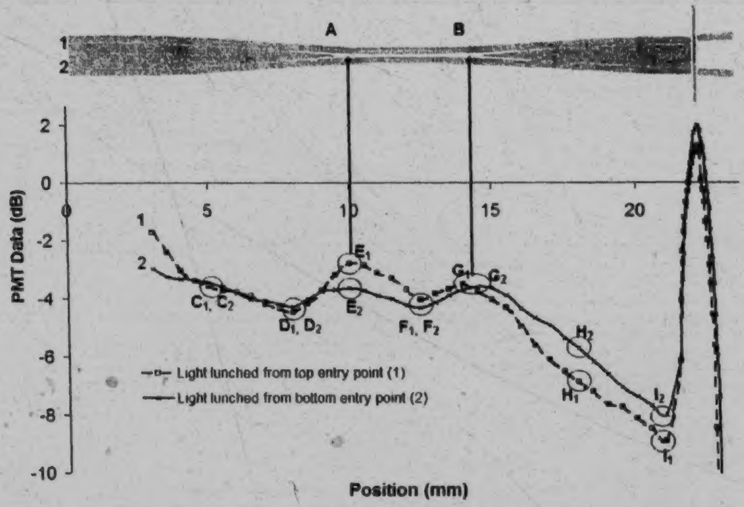

Figure 5.4: *Plot of the measurement of the scattered light at 635 nm from different points of the SU-8 waveguide. Two plots correspond to the launching of input light from two waveguide entrances. Different points on this graph are discussed in Figure 5.5*

5.2.1 Loss Measurement at 635 nm

A multimode fiber with 50μm core diameter was used to deliver 200 mW of 635 nm laser light to one of the entry points (Point 1 in Figure 5.2 (a)) of the long waveguide. The signal from different parts of the waveguide was captured by a 1 mm core diameter fiber which delivers the signal to the PMT. Contrary to the previous work (Section 4.1 and Section 4.2), a Schott glass RG665 long pass filter with a cutoff at 665 nm was placed inside the PMT [62]. The scattered light was measured by scanning with the pick-up fiber at 0.5 mm intervals along the waveguide. The complete system can be visualized by a CCD camera mounted on a microscope. The PMT pick-up fiber was positioned under the chip so that the set-up can be viewed properly through the microscope. The scattered light from the other waveguide was measured moving the input fiber to point 2 in Figure 5.2 (a)).

Figure 5.4 shows the variation of PMT signal with respect to the scattered light from different points of the waveguide. As expected the scattered light decreases as we move away from the light entry point until the intersection point. The excess scattering arises at the two points where the waveguide splitting and mixing take place (points A and B). Due to the scattering from the coupling region between S-bends and straight waveguides, more light is scattered at these two places. The scattered light at different points of the waveguide is compared in Figure 5.4 by changing the launching conditions from the waveguide 1 to the waveguide 2. The PMT signal in mV is proportional to the optical power, so that $10log_{10}(PMTsignal)$ is equal to the optical power in dB with an offset. As expected, at the intersection point, the scattered reflection from microchannel wall increases abruptly. Different points as displayed on Figure 5.4 are used to measure loss and discussed in Figure 5.5.

Figure 5.5 shows different extremum points as displayed in Figure 5.4. The loss was calculated by fitting a straight line between points C, D, H and I for both waveguides. The loss was found to be 3.1 dB/cm and 2.5 dB/cm for launching the light into inputs 1 and 2 respectively.

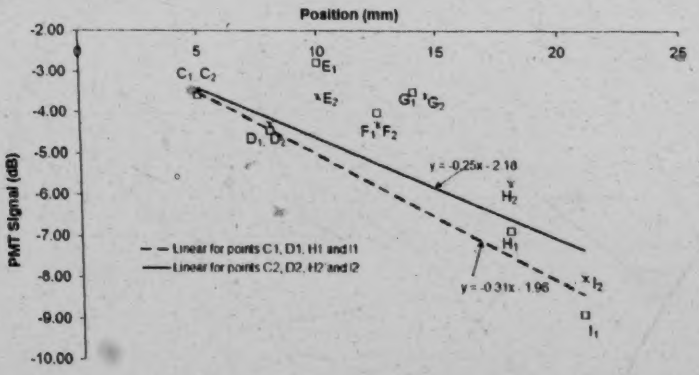

Figure 5.5: *Measurement of loss at 635 nm from between points C, D, H and I of the two SU-8 waveguides. The loss was found to be 3.1 dB/cm and 2.5 dB/cm corresponding to the launching of input light from two waveguides.*

5.2.2 Loss Measurement at 530 nm

The propagation loss of SU-8 waveguides was measured at 530 nm, using a similar method as discussed in Section 5.2.1. Figure 5.6 shows the plots of the variation of the PMT signal (in dB at gain of 10^6) from different points of the waveguide by changing the launching conditions from the waveguide 1 to the waveguide 2. As discussed in the previous section, at points A and B, the PMT signal increases. Different points as displayed on Figure 5.6 were used to measure loss and discussed in Figure 5.7. Figure 5.7 shows different extremum points as displayed in Figure 5.6. The loss was calculated by fitting a straight line between points C, D, H and I for both waveguides. The loss was found to be 5.2 dB/cm and 6.1 dB/cm for launching the light into the inputs 1 and 2 respectively.

Different groups have presented the measurement of the propagation loss in SU-8 waveguides. Integrated microfluidic devices developed by Mogensen *et al.* [112] resulted in a propagation losses of 1.4 dB/cm at 633 nm and 3 dB/cm at 530 nm. Lee *et al.* [113] reported a loss of 4 dB/cm at 630 nm, while the loss from the work of Ruono *et al.* [114] was found to be 1.1 dB/cm at 633 nm. Compared to the value of propagation loss as cited by Mogensen *et al.*, the loss of the SU-8 waveguides in the present work is higher. The range of published losses are an indication that losses depend on how the waveguides are

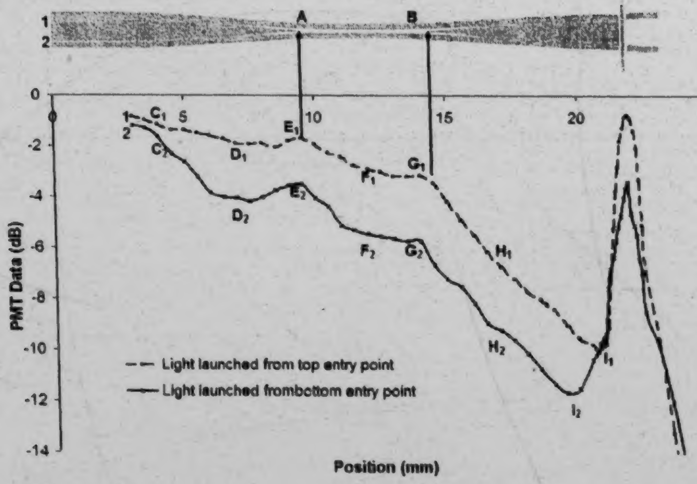

Figure 5.6: *Plot of the measurement of scattered light at 530 nm from different points of SU-8 waveguide. Two plots correspond to the launching of input light from two waveguide entrances. Different points on this graph are discussed in Figure 5.7*

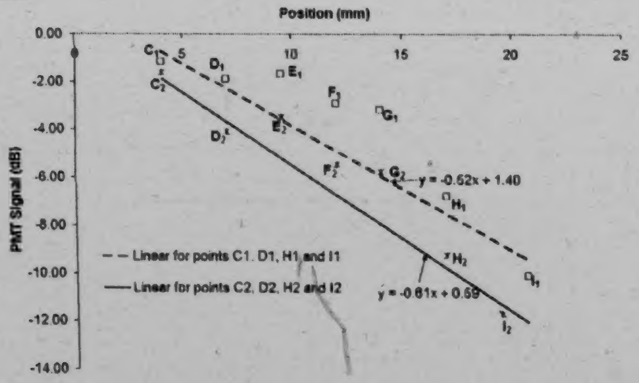

Figure 5.7: *Measurement of loss at 530 nm from between points C, D, H and I of the two SU-8 waveguides. The loss was found to be 5.2 dB/cm and 6.1 dB/cm corresponding to the launching of input light from two waveguides.*

fabricated. One possible reason for the higher propagation loss may be the roughness of the waveguide walls. Despite the higher losses, there is ample power to detect particles.

5.3 Optical Detection and Velocity Measurement of Microparticles

The device described in the Section 5.1 was tested to determine the feasibility of fluorescence detection of microparticles and measurement of their velocities. This was carried out by collecting signals directly with the PMT pick-up fiber directly underneath the intersections and also butt-coupling the PMT fiber to the exit point of output SU-8 waveguide. The experimental set-ups for these two cases are shown in Figure 5.8(a) and Figure 5.8(b) respectively. The microparticles are polystyrene scarlet $FluoreSpheres^{TM}$ from Molecular Probes [70]. These particles have a uniform diameter of approximately 15 μm and absorption and emission peaks at 645 nm and 680 nm respectively [70].

The microparticles, diluted in de-ionized water, were injected into a micropipette connected to one of the reservoirs. Thus, the microparticles were injected into the microchannel by hydrodynamic pressure from the high pressure reservoirs (the reservoir with the pipette tip) to the lower pressure reservoirs (the reservoir without the pipette tip). The velocity of the microparticles will be proportional to the height of the liquid in the pipette tip and can be changed by changing the height. For a 2 cm height of the water level in the syringe tip, the volume of the water is approximately 200 μL, which can be calculated either by knowing the volume of the liquid injected in the syringe tip or by measuring the inside volume of the syringe tip up to the liquid level. So, for a $50\mu m \times 100\mu m$ channel size and a flow velocity of 200 $\mu m/sec$, it will take approximately 2 days for the syringe tip to empty. It is clear that even a small height of water level in the syringe tip will generate a continuous flow in the microchannel for a long time and the flow velocity will be nearly constant for the duration of an experiment.

As the biochip is capped with PDMS, the flow of microparticles cannot be initiated by just hydrodynamic-pressure and capillary action due to hydrophobic nature of the PDMS surface (Section 3.2.3). Therefore, at the start a reverse pressure was applied to the low pressure reservoir so that flow starts building up, which continues due to hydrodynamic

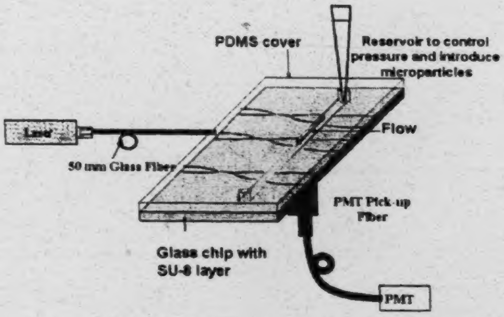
PDMS cover
Reservoir to control pressure and introduce microparticles
Laser
Flow
50 mm Glass Fiber
PMT Pick-up Fiber
Glass chip with SU-8 layer
PMT

(a) The PMT pickup fiber was underneath the chip.

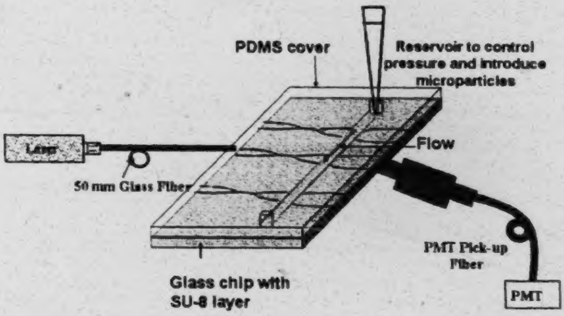
PDMS cover
Reservoir to control pressure and introduce microparticles
Laser
Flow
50 mm Glass Fiber
PMT Pick-up Fiber
Glass chip with SU-8 layer
PMT

(b) SU-8 waveguide is butt-coupled with plastic pick-up fiber at the other end.

Figure 5.8: *The schematic of the experimental setup used for fluorescence detection of microparticles in SU-8 biochip. The syringe tip is used to control the flow of microparticles.*

pressure. A 635 nm laser launched light on the entrance of the SU-8 waveguide using a 50 μm multimode fiber. Light from the input waveguide splits into two parts and shines light at two points of the microchannel which can be collected by a PMT. The PMT signal is collected by the computerized data acquisition (DAQ) system which is controlled by a custom designed $LabView^{TM}$ program. A microscope and a CCD camera are used to visualize and record the experiment.

5.3.1 Detection with Plastic Fiber Below the Intersection

The fluorescence from the microparticles was collected using the plastic optical fiber placed underneath the microchannel-waveguide intersection point on the chip. The schematic view

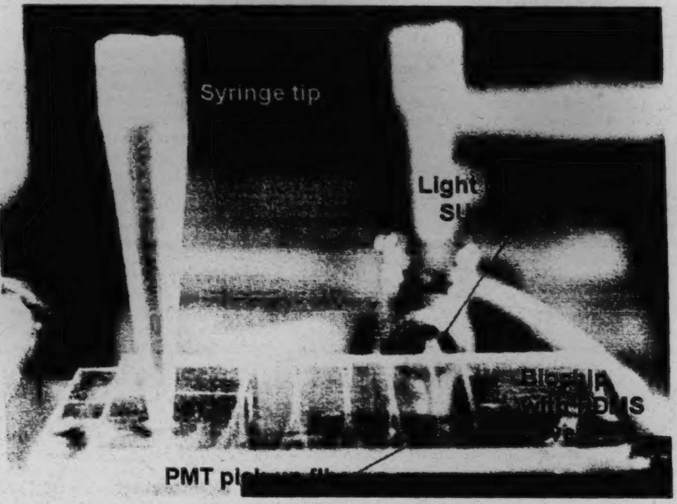

Figure 5.9: *An image of the experimental set-up used for optical detection of microparticles in SU-8 biochip. The laser light is launched from the multimode fiber connecter at the far side and the PMT fiber is underneath the chip.*

of the experimental set-up is demonstrated in Figure 5.8(a) and a picture of the experiment is shown in Figure 5.9. As the distance between two points is 200μm, the PMT pickup fiber with core diameter of 1 mm will easily capture the signal from both points at the same time.

A video sequence with 30 frames per second of the flow of microparticles under pressure-driven flow was recorded. Figure 5.10 shows 12 frames with 1/6 s spacing of one fluorescent microparticle moving from right to the left. The center-to-center distance between the waveguides intersecting the microchannel is 200 μm. It is clear from the figure that the particle is visible only in frames 1 to 3 and 9 to 12. This microparticle lies exactly in the intersection corresponding to frame 2 and frame 11. For this particle, it takes roughly 1.5 s to travel the distance of 200 μm between the two intersection points for an average velocity of approximately 133 μm/sec.

The estimated velocity, by measuring the time between two intersection points, is not very accurate, because the minimum time spacing between frames is only 1/30 seconds. A more accurate time between peaks was measured from the PMT data, which was captured

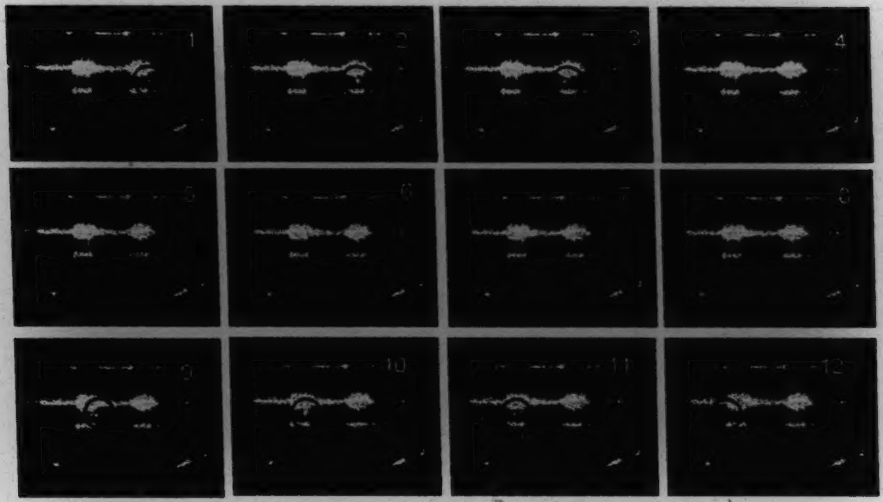

Figure 5.10: *12 frames showing movement of one fluorescent microsphere in a pressure-driven flow. The frames in this picture are 1/6 s apart. The bead position is indicated by a circle.*

while recording the same video sequence as shown in Figure 5.10. The video sequence and PMT data were recorded for a total of 100 seconds as shown in Figure 5.11(a). The LabView VI samples the PMT signal and stores in a raw file. PMT data was averaged using another VI file and stored in another file.

There was a time lag of approximately 3 seconds between the time on the video file on the computer and data recorded by the PMT, which is due to the limitation of the capturing software. The software stops capturing the video if a user hits any key which limits the user to first start the LabView program to capture data before the video capture software.

As the particles move from right to left (Figure 5.10), there is a high probability for two particles to be in intersection regions at the same time when the density of particles flowing in the microchannel is high. This can be easily seen from the data between 32 and 68 seconds as shown in Figure 5.11(a). During 100 seconds of total recorded video, clear evidence of six individual particles in the detection region was observed between 68 and 100 seconds as seen in Figure 5.11(b). It is also clear that no particle is flowing during first 30 s of the recorded data.

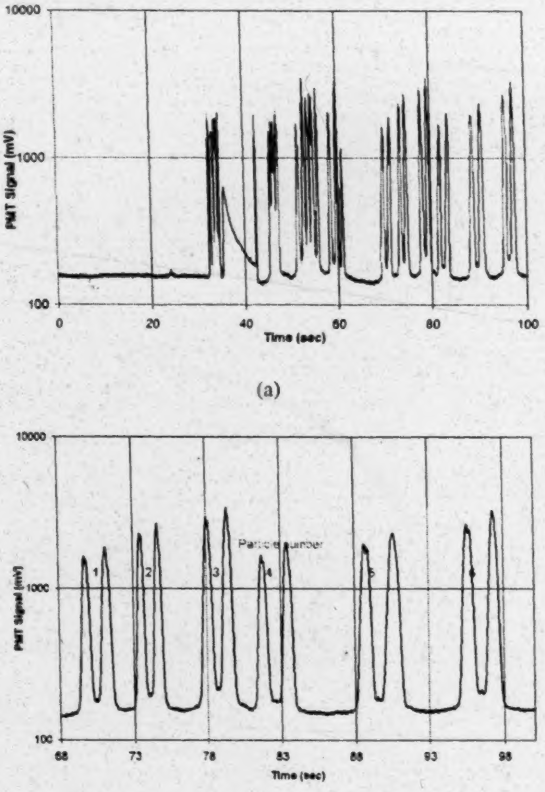

(a)

(b) PMT signal

Figure 5.11: *(a) Plot of 10, 000 points over 100 s PMT signal, and (b) PMT response (mV) from 6 particles as a function of the time (seconds).*

From 320,000 samples taken during the last 32 s interval of the experiment, 3200 averages were taken from each group of 100 consecutive samples. Figure 5.11(b) is a plot of these 3200 points within 32 seconds representing passing of 6 particles. The video frames in Figure 5.10 correspond to the first particle in Figure 5.11(b). The exact time interval between two peaks corresponding to each particle can be calculated from this graph. From this time interval, the velocity of each moving microparticle has been calculated and tabulated in Table 5.1. The velocity was calculated by video frames and PMT data and is compared in the table. These velocities are closely related to the velocities measured by video frames within 3-5 % difference.

Table 5.1: Velocity measurement in SU-8 biochips with the PMT fiber under the intersection points. The distance between the intersection points is 200 μm.

Particle Number	Velocity from video frames			Velocity from PMT data	
	Frames	Time between peaks (s)	**Velocity (μm/sec)**	Time between peaks (s)	**Velocity (μm/sec)**
1	45	1.50	**133**	1.43	**140**
2	35	1.17	**171**	1.20	**167**
3	40	1.33	**150**	1.37	**146**
4	50	1.67	**120**	1.74	**115**
5	55	1.78	**109**	1.78	**112**
6	55	1.75	**109**	1.75	**114**

From the measured velocity of different particles, the position of the particle in the microchannel at the time of arriving at the intersection can be assumed. As discussed before, this is due to the fact that the velocity profile under pressure-driven flow is nearly parabolic (as discussed in Section 2.1.2). Therefore, it may be assumed that faster particles are traveling near the center o fthe microchannel than slower particles. Therefore, the second particle travels more towards the center, followed by the third and the first particles. Other particles (fourth, fifth and sixth) travel more towards the walls in comparison to first three particles.

5.3.2 Collecting Fluorescence from the SU-8 Output Waveguide

Figure 5.8(b) is a schematic of the set-up used to detect fluorescence from moving microparticles by the SU-8 output waveguide. This set-up is similar to the one discussed in the previous section except the PMT pick-up fiber is butt-coupled with the output SU-8 waveguide. The picture of the experiential set-up is shown in Figure 5.12. In this case, the center-to-center distance between two waveguide-microchannel intersection points is 600μm.

The output SU-8 waveguide has a parabolic shaped air cladding with 50 μm width

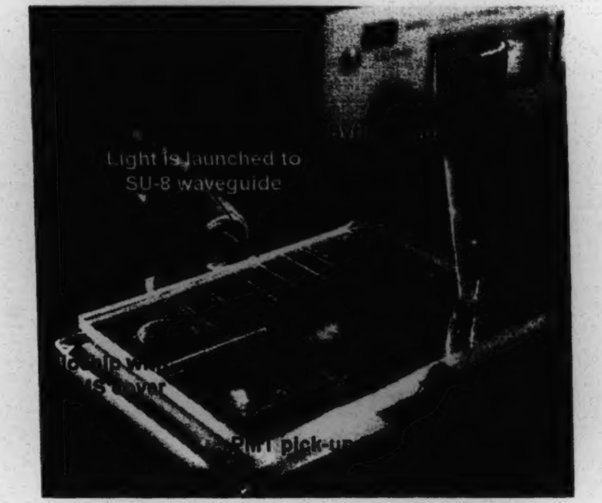

Figure 5.12: *The picture of the experimental setup as shown in Figure 5.8(b)*

(Figure 5.2 (b)). The parabolic shape was designed to increase the amount of fluorescence light that can be collected by the output waveguide. As before, a syringe tip full of de-ionized water mixed with microparticles works as a reservoir to supply the microparticles in the microchannel. The velocity of the microparticles can be adjusted by changing the height of the liquid column in the syringe tip.

A method similar to the one discussed in Section 4.2 and Section 4.3 was used to record video sequence and captured data from PMT and measure the velocity of moving microparticles. The time between peaks was measured using captured PMT data to achieve a more accurate measurement of time. A 100 second PMT signal was recorded and averages were calculated after every 100 samples (0.01 s). As the PMT signal was sampled by LabView VI, a 100 seconds signal generated 10,000 points after averaging over a group of 100 consecutive samples. Figure 5.13 is a plot of 10,000 points over 100 s PMT signal. It can be observed from the plot that there are more than 60 peaks within the span of 100 s which indicates more than 30 particles passed by in 100 s. It is also observed that the background light with noise also changes by approximately 6-7 % in the span of 100 s. This change might be due to the change in laser power or the movement of the launching

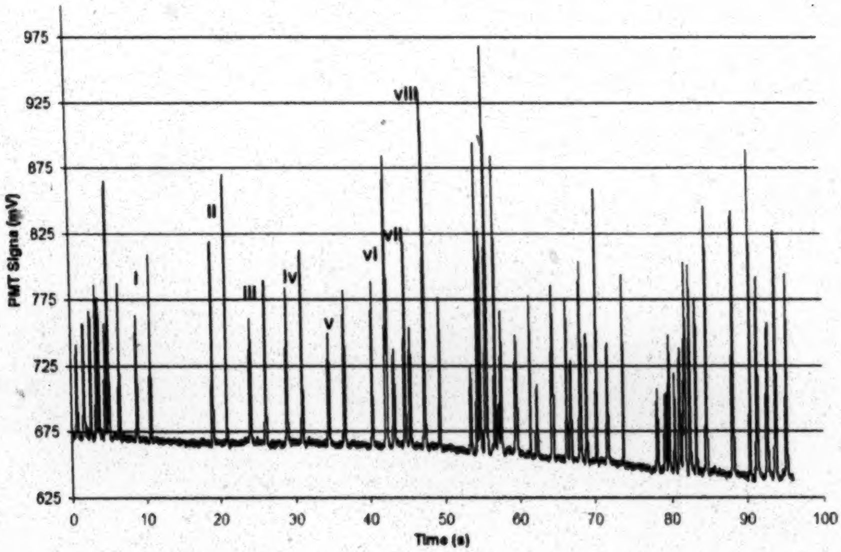

Figure 5.13: *Plot of 10, 000 points over 100 s PMT signal. There are more than 60 peaks within the span of 100 s, indicating the movement of more than 30 particles in 100 s. Eight particles represented here are shown in Figure 5.14.*

or pick-up fiber.

The PMT scan was analyzed to distinguish particles with clearly defined peaks. After scanning through all the peaks it was found that between 7 and 49 seconds there was a very clear indication of the movement of eight particles. The PMT scan between 7th and 49th second is shown in Figure 5.14 where 16 peaks are indicated by corresponding the particle number.

Figure 5.15 shows the details of the response of two peaks for each particle. The shape of the PMT response was studied for both peaks for each particle. The first and the second peaks for all the particles have a similar shape which validates our assumption of identifying eight particles. As can be seen in Figure 5.13 and Figure 5.15, the strength of the signal from each microparticle is different which may be explained by the fact that each particle moves in different parts of the flow where the light intensity is different. The difference between the strength of the signal of each microparticle from both intersection points can be observed from Figure 5.15. This might be due to different

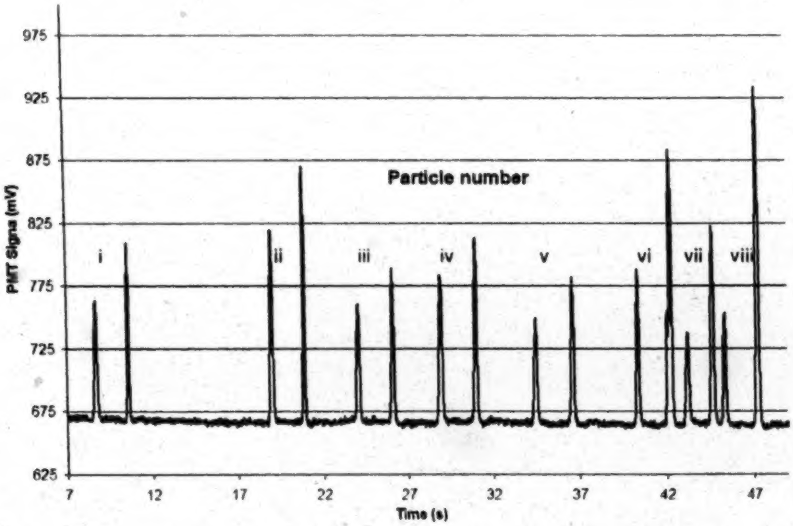

Figure 5.14: *The PMT scan between 7th and 49th second showing the movement of 8 particles.*

amounts light propagating in the two incoming waveguides. The time between peaks for different particles is different which clearly shows that each particle moves with a different velocity. As these particles were moving under pressure-driven flow, their unequal velocities indicates they were moving in different parts of the microchannel (Section 2.1.2). The video show that particles travel in different parts of the channel.

From the shape of two peaks for eight microparticles, peaks for other microparticles can be identified. Figure 5.16 describes 4 of such identified microparticles. From Figure 5.16(a), it is clear that the first and second peaks correspond to the particle (ix) and the third and fourth peaks correspond to particle (x). Similarly from Figure 5.16(b) particle (xi) and (xii) were identified. From Figure 5.16(a), a discrepancy can be seen for particle (ix) for which the width (in terms of time) for the two peaks is not the same. This may be explained by considering a possible variation of the light pattern at the intersections and non-uniformity of the dye in the microparticle. Also, it is possible that there is an increment in particle velocity while going from one intersection to the another, which would lead to a

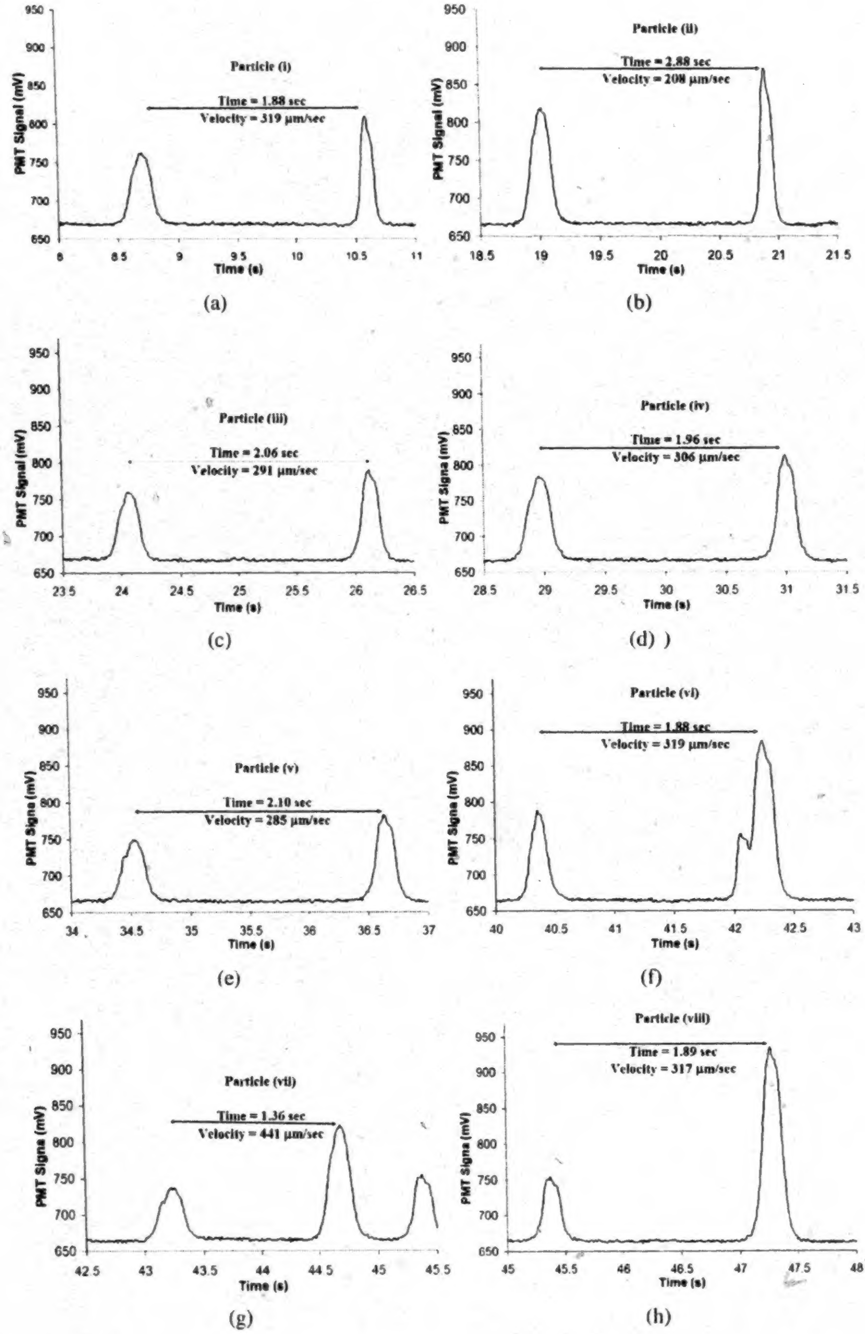

(a) (b)

(c) (d))

(e) (f)

(g) (h)

Figure 5.15: *Details of the PMT signal corresponding to eight particles as shown in Figure 5.14.*

Table 5.2: Velocity measurement in SU-8 biochips. The PMT fiber is butt-coupled with the output waveguide. The distance between the intersection points is 600 μm.

Particle Number	**Corresponding Figure**	**Time between peaks (s)**	**Velocity (μm/sec)**
i	Figure 5.15(a)	1.88	319
ii	Figure 5.15(b)	2.88	208
iii	Figure 5.15(c)	2.06	291
iv	Figure 5.15(d)	1.96	306
v	Figure 5.15(e)	2.10	286
vi	Figure 5.15(f)	1.88	319
vii	Figure 5.15(g)	1.36	441
viii	Figure 5.15(h)	1.89	317
ix	Figure 5.16(a)	1.89	317
x	Figure 5.16(a)	2.04	294
xi	Figure 5.16(b)	2.32	259
xii	Figure 5.16(b)	2.45	245

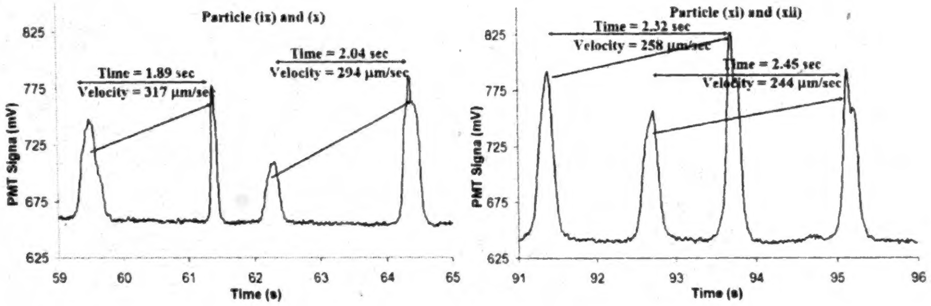

(a) (b)

Figure 5.16: *Details of the PMT signal corresponding to four particles. From the relative size of the plots as described in Figure 5.15, the peaks related to these four particles are recognized.*

difference in the widths for the two peaks.

There may be a problem in velocity determination and sorting when peaks are close to each other which can affect how each particle is sorted. Sheath flow is one way to reduce this problem, which is used in conventional cell-sorters as described in Section 1.1.

Velocities of all twelve microparticles identified during 100 seconds from PMT signal can be measured by calculating the time between peaks to travel to travel the distance of 600 μm. The time between peaks and velocity of each particles is shown in Figure 5.15, Figure 5.16 and Table 5.2.

5.4 BPM Simulation

Beam propagation method (BPM) simulations were undertaken to understand the nature of the light propagation in the structure with waveguides and microchannels as shown in Figure 5.1 (b). These simulations were carried out using in-house software previously developed [115] that is based on a traditional split diffraction-refraction method [116].

The dimensions of the structure are given in Figure 5.17. The regions labeled WG, S, M and V represent SU-8 (index 1.59) and are the core regions of the waveguides and the walls of the microchannel. The remaining part, except the filled microchannel (shaded with index 1.33) is assumed to be a material with index 1.5. Therefore, the cladding of the waveguide will have an index of 1.5 contrary to the fabricated opto-biochip as shown in Figure 5.1(b). This was due to limitations in BPM simulations. As discussed in Section 5.1, the depth of all the parts of the present structure is equal to the height of the SU-8 layer, 50 μm. Two input waveguides, WG1 and WG2 (part A), combine to the mixer region, M (part C), by two S-bends, S_{11} and S_{21} (part B), where the light from two waveguides can mix. The straight waveguide, M, splits into two waveguides by two S-bends, S_{12} and S_{22} (part D), that deliver light to two points, I_1 and I_2 of the microchannel (part F). The output waveguide WG3 (part H) captures signal from both intersection points. Part E and G are the channel walls.

This model assumes that all the light is confined within a slab of thickness H = 50 μm, the approximate depth of the waveguides and microchannels. The equations of the S-bends were written as a sinusoidal function and the lengths and offsets of the S-bends were chosen

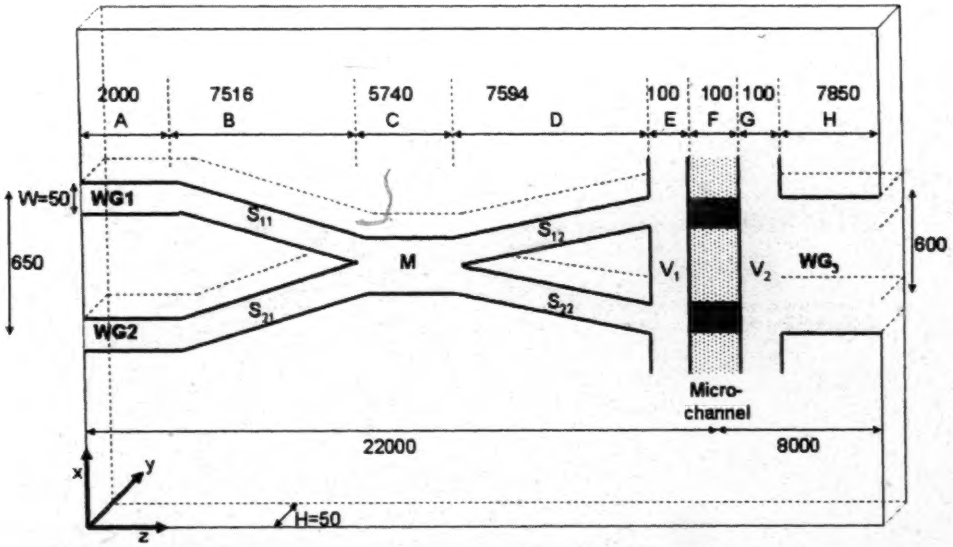

Figure 5.17: *Dimension of a structure with waveguide and microchannel as shown in Figure 5.1 (A). All the numbers are in micrometers. The core of the waveguide is of index 1.59, the index of the the microchannel is 1.33 and remaining part is considered with index 1.5 due to the limitation in BPM simulations.*

according to the fabricated design. As shown in Figure 5.17, the z-axis is the propagation direction, the x-axis is the the microchannel flow direction and the y-axis is out of the plane. The equation of a S-bend with length L and offset D is,

$$x = D\frac{z}{L} - \frac{D}{2\pi}\sin\left(\frac{2\pi z}{L}\right). \tag{5.1}$$

For the present simulation, superposition of sinusoidal fields with random phase to emulate the output of a multimode fiber were considered. The offsets of two sets of S-bends are 300 μm (for S_{11} and S_{21}), and 275 μm (S_{12} and S_{22}) respectively. The center-to-center distance between waveguides intersecting the microchannel is 600 μm. For 8192 grid points along the x-direction, and a spacing $\Delta x = 0.2\mu m$, the difference between each point along x-direction in the plot (Figure 5.18) will be 3.2 μm. On the y-axis, points are spaced with a difference of 1 μm on the plot. Here, a random laser beam is considered.

5.4.1 Flux Flow

Figure 5.18 shows the plot of the 2-dimensional power flow pattern of the 635 nm light launched at WG1 (Figure 5.18(a)) and WG2 (Figure 5.18(b)). The light combines in the mixing region, M, and then splits into the two waveguides of Section D. Figure 5.19 shows the flux propagation profile in the waveguide from a different angle.

Figure 5.20 describes the variation of the laser power across the microchannel (center of region F in the Figure 5.17). It is clear from the Figure 5.20 that the peak power is approximately the same at two intersections even if the launching point is changed from A (Figure 5.20(a)) to point B (Figure 5.20(b)). From the simulation results, as described in Figure 5.19 and Figure 5.20, the power at the center of the microchannel is averaged over every 15 points (approximately 48 μm) to get these plots. Contrary to this, in the actual PMT data in Figure 5.14, the second peak (peak on right side) is higher than the first peak (the peak on the left side). In the PMT data, the light is launched into the input waveguide right across from the first peak.

Figure 5.21 shows CCD camera pictures of two microchannel-waveguide intersections I_1 and I_2 (Figure 5.1). When the light is launched at two points it is converted to an intensity matrix and plotted as shown in Figure 5.22. As can be seen from the intensity profile in Figure 5.22, it is clear that the peak intensity at the intersections is approximately same even after changing the launching condition from point A to point B. Therefore, the intensity profiles agree well with the intensity distribution achieved by BPM simulation as shown in Figure 5.20.

In this section, a scheme for simulating light propagation in SU-8 waveguides has been described and the light at two intersections in the microchannels is demonstrated. The powers from the BPM simulation and Matlab intensity plots are found to be equally divided at two intersections, I_1 and I_2. There are approximations in the values obtained by these different methods. In the BPM simulations, the dimensions of the structure (Figure 5.17) in region M were slightly different from the dimensions of the fabricated opto-biochip (Figure 5.2). Also, the cladding index is assumed to be 1.50, contrary to 1 (air) in the fabricated opto-biochip. The BPM simulations do not take surface roughness and index fluctuations into account. The pictures in Figure 5.21, were taken using a CCD colored

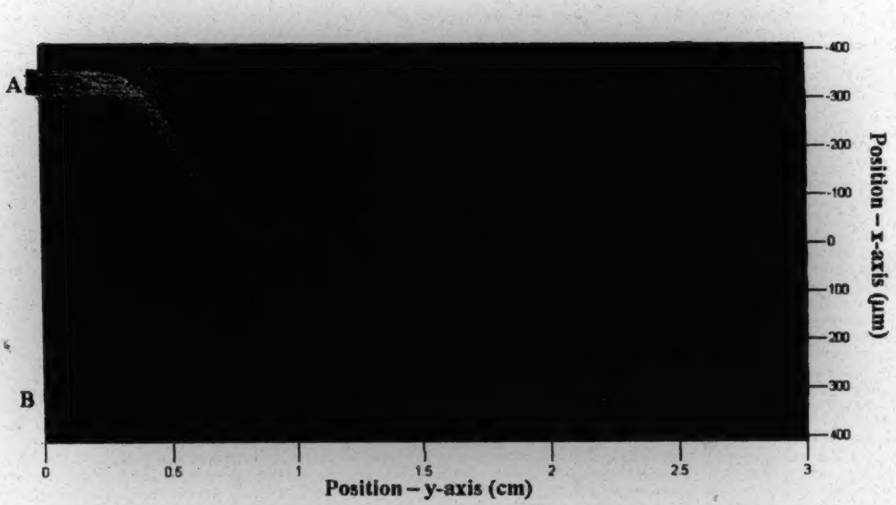

(a) Light is launched at point A

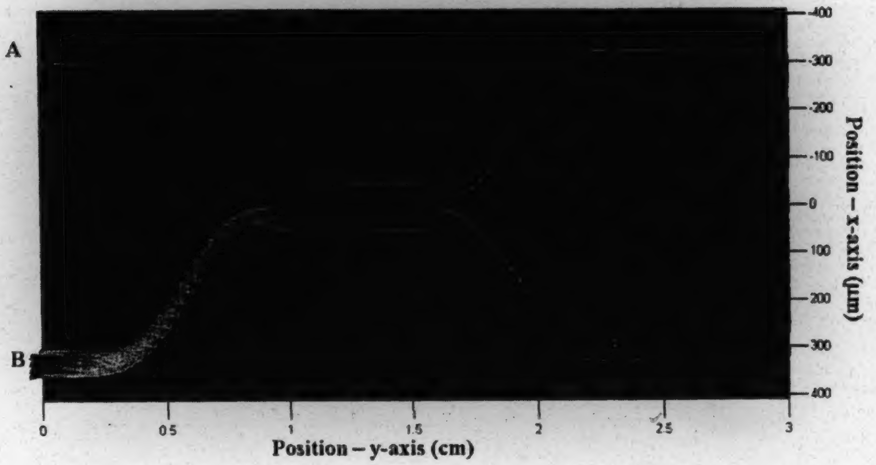

(b) Light is launched at point B

Figure 5.18: *Laser beam propagating into the waveguide consisting of straight sections and S-bends.*

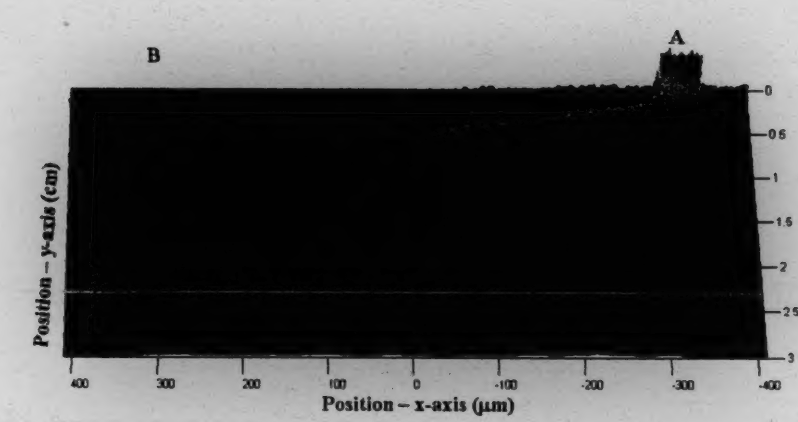

(a) Light is launched at point A

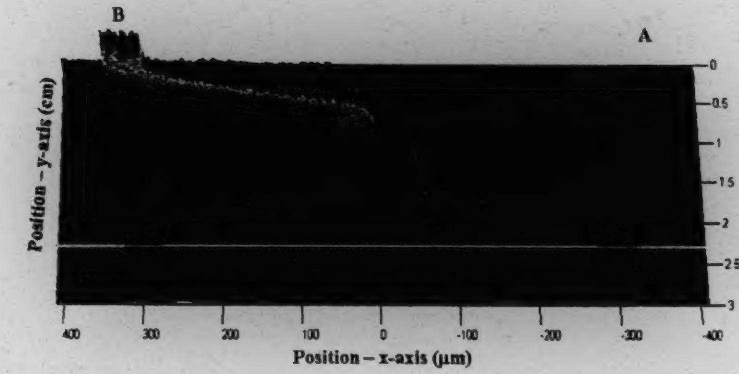

(b) Light is launched at point B

Figure 5.19: *Laser beam propagating into the waveguide consisting of straight sections and S-bends from a different angle.*

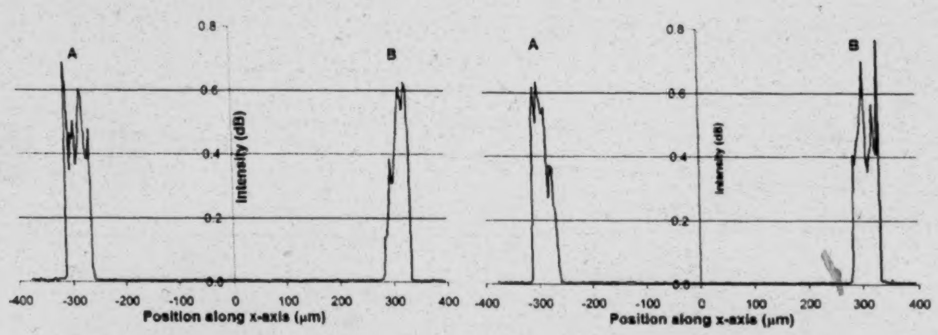

(a) Light is launched at point A (b) Light is launched at point B

Figure 5.20: *Variation of the power of laser beam in the microchannel. The graphs show that the power at the two intersections is distributed almost equally even after changing the entry point of the incident laser light.*

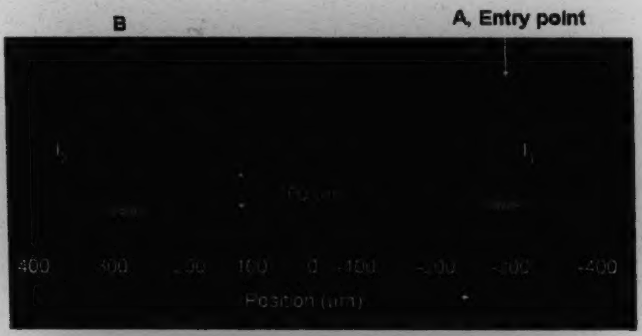
B
A, Entry point
100 μm
400
300
200
100
0
-100
-200
-300
-400
Position (μm)

(a) Light is launched at the entry point A.

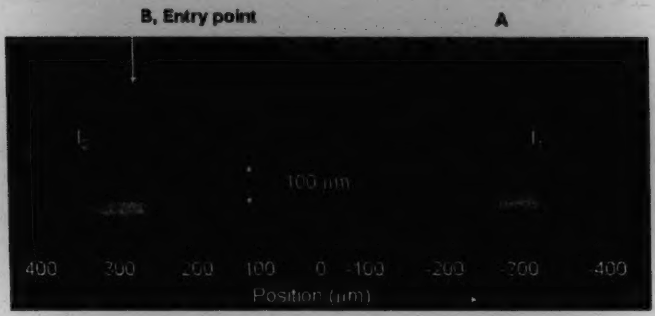
B, Entry point
A
100 μm
400
300
200
100
0
-100
-200
-300
-400
Position (μm)

(b) Light is launched at the entry point B.

Figure 5.21: *Picture of the two waveguide-microchannel intersections when the entry point of the incident light is changed.*

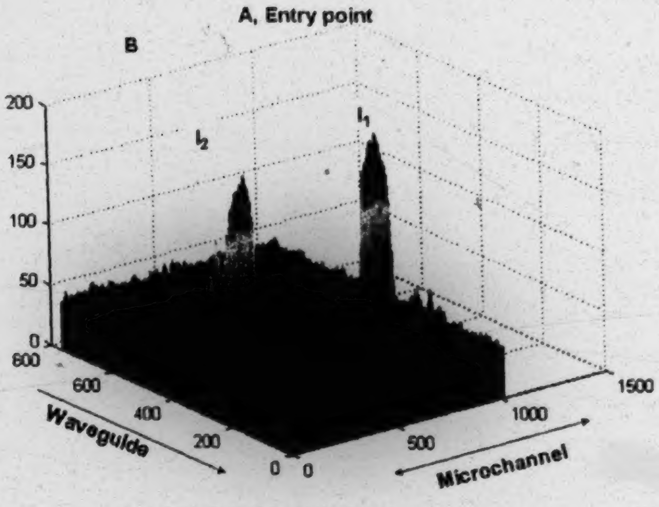

(a) Light is launched at the entry point A.

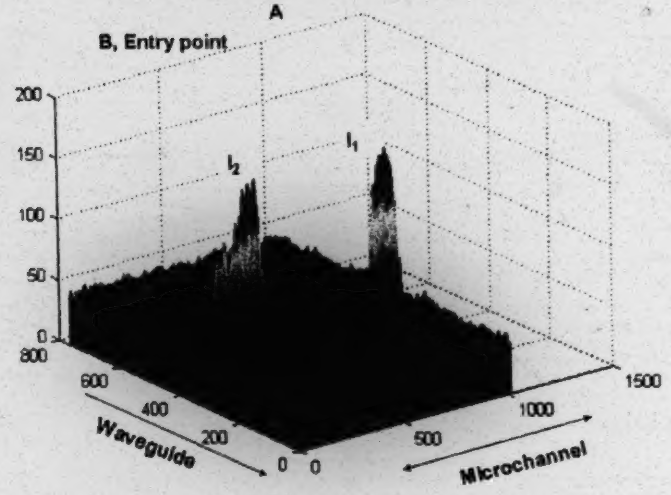

(b) Light is launched at the entry point B.

Figure 5.22: *Intensity profile using inside a microchannel as shown in Figure 5.21, all values are in* μm.

camera and converted to Matlab intensity plots by averaging over every seven pixels.

In this chapter, the fluorescence detection in microfluidic channels integrated with multimode waveguides has been presented. Here, the process involved only a single mask step (Section 3.2.4) and the chips are bonded with PDMS. A propagation loss of 2.8 dB/cm at 633 nm and 5.7 dB/cm nm at 530 nm was achieved. The input waveguide excites light at the two points in the microchannel and generated double-peaks. The velocity of the microparticles has been measured by measuring the fluorescence signal from the double-peaks. BPM simulation provides a mechanism to visualize the light propagation in the SU-8 waveguides can be used to predict the intensity distribution in the microchannel of fabricated opto-biochips of various designs.

The design of the device can be improved by exploring a way so that the waveguides emit different intensities at the microchannel intersections. This way, the fluorescence from the microparticles from one waveguide can be identified. Future developments of the devices involve investigations of remaining parts to achieve cell-sorting in these devices. These include to explore a method to switch the pressure-driven flow between two output reservoirs and to investigate the possibility of electroosmotic flow in these opto-biochips [117].

Chapter 6

Conclusion

As mentioned in the introduction, the main focus of this research has been the feasibility of realizing a cell-sorter based on integrated optics, fluorescence detection, velocity measurement and flow switching. The contribution of the present work can be broken down into two broad parts. The first part is the fabrication of the devices using different materials, and the second part is the optical detection and velocity measurement in different devices. A lesser contribution is the switching of electroosmotic flow in PDMS biochips. The following is a chapter-by-chapter summary of the content and results obtained along with suggestions for future work.

6.1 Summary of the Results

1. **Chapter 2:** General principles of microfluidics and integrated optics were discussed in this chapter. First, different physical phenomena affecting microfluidics were discussed. Two different mechanisms to develop flow- pressure-driven flow and electroosmotic flow were discussed and compared. The velocity due to pressure-driven flow was found to behave parabolically, where velocity at the center is maximum, and the velocity due to electroosmotic flow is constant throughout the channel for high concentration of the electrolyte solution. The advantages and disadvantages of the two types of flows and their applications while studying flow in different systems were discussed. Light propagation in the waveguides due to total internal reflection and the requirements to achieve integrated optics in the present research were discussed in this chapter.

2. **Chapter 3:** Different fabrication approaches were described in this Chapter. The direct-laser writing process was used to fabricate microchannel wall and microchannel on UV-curable polymer in one-step. To fabricate devices in the polymer, a master with inverse pattern was fabricated by two different techniques. The first one was the direct laser-writing using a UV-curable polymer and the second was using lithography and a dry plasma etching to generate structure of desired depth. The laser-writing process is time efficient, but lithography produces a smoother pattern. Hot embossing on PMMA and PDMS casting were used to achieve a final device by replicating the master. Although PDMS casting resulted in very smooth pattern of microchannels, hot embossing on PMMA generates a bent PMMA plate and broken master. The PDMS biochip was irreversibly bonded using oxygen plasma to support electroosmotic flow. A single-step process to fabricate an opto-chip on glass using SU-8 was presented. These biochips do not support the electroosmotic flow but support pressure-driven flow fairly well.

3. **Chapter 4:** Optical detection of the fluorescent microparticles in a glass microcapillary, glass biochip with ion-exchanged waveguides and PDMS biochips were discussed in Chapter 4. A plastic-optical fiber was used to shine light and capture signal from the moving microparticles under the pressure-driven flow. The velocity of the microparticles was calculated by analyzing the fluorescence spectra. In the glass biochip with ion-exchanged waveguides, the electroosmotic flow was generated and the signal was collected by a plastic fiber, and fed to the PMT. The anomaly in the microchannel etching process resulted in a double intensity peak at the waveguide-microchannel intersection. This was used to measure the velocities of the microparticles in the ion-exchanged opto-biochips. The electroosmotic flow initiates the movement of the microparticles in the PDMS biochip. The velocities of the microparticles in biochips with ion-exchanged waveguides and PDMS biochips were measured by counting number of video frames passed between two points in the microchannel. Flow of the microparticles was switched between the two output reservoirs in the PDMS biochip.

4. **Chapter 5:** The SU-8 opto-biochips were used to detect the fluorescence from microparticles and measure their velocities. First, the loss from SU-8 waveguides was measured at two different wavelengths, 635 nm and 530 nm. The pressure-driven flow was used to observe a continuous flow of microparticles. The velocity of the microparticles was found by analyzing the PMT signal. The simulations based on beam propagation method demonstrate the uniformity of the waveguide splitters and the coupling of the light at the microchannel-waveguide intersection and. The rapid and efficient fabrication process of SU-8 opto-biochips provides a solution to realize an integrated biochip analysis system for cell-sorting.

6.2 Recommendations for Future Work

There are many ways in which the research in fabrication and detection, presented here can be improved and built upon for the future. A few ways are mentioned here:

1. **SU-8 device capping:** In the present work, the SU-8 opto-biochips are capped with the PDMS. During the experiments, the sealing between the PDMS and the SU-8 does not remain strong while observing a continuous pressure-driven flow. There is a need to improve the adhesion of SU-8 with glass and sealing the top layer. The sealing can be performed by spin-coating a separate SU-8 layer with lower index of refraction on a Pyrex wafer and manually sealing with the bottom glass wafer with high index SU-8 layer [118]. The index of refraction of SU-8 can be changed by changing the hard-bake time [119].

2. **Laser-writing process**

   In this research, a direct UV laser-writing was one of the techniques used to fabricate the complete device (section 3.2.1). Although it was possible to fabricate the microchannel and waveguide in a single-step writing process, these devices could not be used in microfluidic applications due to the limitation in sealing with a top layer.

   A possible variation could be to use a suitable material which is optically transparent, thick and can work as a UV curable positive photoresist to provide waveguide core

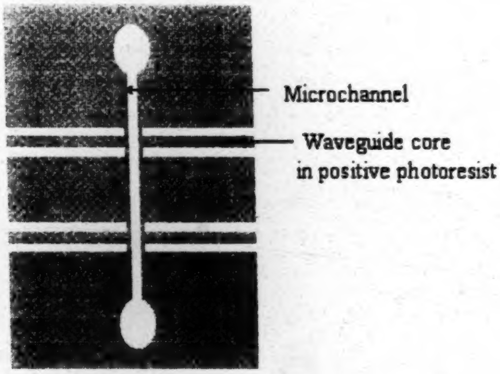

Figure 6.1: *A schematic of a proposed device after laser-writing. The white part is air where laser-writing will takes place and rest part will have photoresist.*

and a fluidics layer. Figure 6.1 shows the proposed design of the final device by laser-writing on a positive photoresist. A suitable material should be explored to cap this device (Section 3.2.2). After spin-coating this resist on a substrate, the resist will be removed wherever laser-writing will take place (white part of the Figure). This way, the removed parts of the resist will work as microchannel and the cladding of the waveguide.

3. **Electroosmotic flow in SU-8 microchannels:**

   SU-8 has a simple fabrication method to achieve opto-biochips and observe pressure-driven flow. However, the inability to support electroosmotic flow limits its uses in many microfluidic applications. Recently, Sikanen et. al. [117] reported a method to observe electroosmotic flow in SU-8 microchannels. Observing electroosmotic flow in SU-8 opto-biochip is one of the recommendations of future research. An opto-biochip with circulating microchannel (Figure 3.12(c) (c)) should be used to observe a continuous flow and detect microparticles.

4. **Cell-sorting**

   Based on the different units of a cell-sorter as described in Section 1.1.2, the following improvements would have to be made to achieve cell-sorting in SU-8 opto-biochips.

- *Detecting different kinds of particles-* Experiments should be performed to detect different kinds of microparticles simultaneously. This should be done by using the SU-8 waveguide design as discussed in Figure 5.1(b). The fluorescence from different microparticles can be detected by combining two PMTs to an output fiber butt-coupled to the SU-8 output waveguide.
- *Real-time velocity measurement-* The LabView software, can be updated so that the velocity of the microparticles can be determined as soon as the microparticles hit both the waveguide-microchannel intersections.
- *Flow switching-* The flow of the microparticle can be switched by knowing the time required for the particle to travel from intersection point to the point it needs to be switched. If pressure-driven flow is driving the microparticles, a valve can be used to switch the flow from one output reservoir to another. If the flow is electroosmotic, then a LabView controlled electronic switch will be able to switch the flow. This switch has already been developed in our lab by another researcher.

Combining the fabricated opto-biochip, updated software and an automated switch, this research could potentially lead to a unique sorting technique.

Bibliography

[1] Dongeun Huh, Wei Gu, Yoko Kamotani, James B Grotberg1, and Shuichi Takayama. 'Microfluidics for flow cytometric analysis of cells and particles.' *Physiological Measurement*, vol. 26: pp. R73–R98 [2005]. `http://dx.doi.org/10.1088/0967-3334/26/3/R02`.

[2] Paul K. Horan and L. Wheeless Jr. 'Quantitative Single Cell Analysis and Sorting.' *Science*, vol. 198: pp. 149–157 [1977].

[3] L. A. Kamentsky, M. R. Melamed, and H. Derman. 'Spectrophotometer: New Instrument for Ultrarapic cell analysis.' *Science*, vol. 150: pp. 630–631 [1965]. `http://www.research.ibm.com/journal/rd/411/shaw.html`.

[4] Howard M. Shapiro. 'Multistation multiparameter flow cytometry: A critical review and rationale.' *Cytometry*, vol. 3(4): pp. 227–243 [January 1983]. `http://dx.doi.org/10.1002/cyto.990030402`.

[5] J. Paul Robinson. 'Flow Cytometry.' *Encyclopedia of Biomaterials and Biomedical Engineering*, pp. 630–640 [August 2004]. `http://www.dekker.com/sdek/abstract~db=enc~content=a713554055`.

[6] Marco Rieseberg, Cornelia Kasper, Kenneth F. Reardon, and Thomas Scheper. 'Flow cytometry in biotechnology.' *Applied Microbiology and Biotechnology*, vol. 56(3-4): pp. 350–360 [August 2001]. `http://dx.doi.org/10.1007/s002530100673`.

[7] Claire L. Harding, David R. Lloyd, Caroline M. McFarlane, and Mohamed Al-Rubeai. 'Using the Microcyte Flow Cytometer To Monitor Cell Number, Viability, and Apoptosis in Mammalian Cell Culture.' *Biotechnology Progress*, vol. 16(5): pp. 800–802 [2000]. `http://dx.doi.org/10.1021/bp0000813`.

[8] Maxine A. McClain, Christopher T. Culbertson, Stephen C. Jacobson, and J. Michael Ramsey. 'Flow Cytometry of Escherichia coli on Microfluidic Devices.' *Analytical Chemistry*, vol. 73(21): pp. 5334 – 5338 [2001]. `http://dx.doi.org/10.1021/ac010504v`.

[9] G.B.J. Dubelaar and P.L. Gerritzen. 'CytoBuoy: a step forward towards using flow cytometry in operational oceanography.' *Scientia Marina*, vol. 64(2): pp. 255–265 [2000]. `http://www.icm.csic.es/scimar/642dubel.html`.

[10] N. Wedemeyer and T. Potter. 'Flow cytometry: an 'old' tool for novel applications in medical genetics.' *Clinical Genetics*, vol. 60(1): pp. 1–8 [2001]. `http://dx.doi.org/10.1034/j.1399-0004.2001.600101.x`.

[11] 'The Scripps Research Institute (TSRI) Flow Cytometry Core Facility, http://facs.scripps.edu/facslab.html.'

[12] D. Peters, E. Branscomb, P. Dean, T. Merrill, D. Pinkel, M. Van Dilla, and J. W. Gray. 'The LLNL high-speed sorter: Design features, operational characteristics, and biological utility.' *Cytometerty A*, vol. 6(4): pp. 290–301 [1985]. `http://dx.doi.org/10.1002/cyto.990060404`.

[13] Anne Y. Fu, Charles Spence, Axel Scherer, Frances H. Arnold, and Stephen R. Quake. 'A microfabricated fluorescence-activated cell sorter.' *Nature Biotechnology*, vol. 17: pp. 1109–1111 [1999]. `http://dx.doi.org/10.1038/15095`.

[14] Alberto Orfao1 and Alejandro Ruiz-Argelles. 'General Concepts About Cell Sorting Techniques.' *Clinical Biochemistry*, vol. 29: pp. 5–9 [1996]. `http://dx.doi.org/10.1016/0009-9120(95)02017-9`.

[15] Jan Kruger, Kirat Singh, Alan O'Neil, Carl Jackson, Alan Morrison, and Peter O'Brien. 'Development of a microfluidic device for fluorescence activated cell sorting.' *Journal of Micromechanics and Mciroengineering*, vol. 12: pp. 486–494 [2004]. `http://dx.doi.org/10.1088/0960-1317/12/4/324`.

[16] A. Wolff, I. R. Perch-Nielsen, U. D. Larsen, P. Friis, G. Goranovic, C. R. Poulsen, J. P. Kutter, and P. Telleman. 'Integrating advanced functionality in a microfabricated high-throughput fluorescent-activated cell sorter.' *Lab on a chip*, vol. 3: pp. 22–27 [2003]. `http://dx.doi.org/10.1039/b209333b`.

[17] B. H. Weigl and K. Hedine. 'Lab-on-a-chip based separation and detection technology for life science applications.' *American Biotechnology Laboratory megazine*, pp. 28–30 [2002]. `http://www.iscpubs.com/articles/acl/c0203wei.pdf`.

[18] Otto Leistiko and Peter Friis Jensen. 'Integrated bio/chemical microsystems employing optical detection: the clip-on.' *Journal of Micromechanics and Microengineering*, vol. 8: pp. 148–150 [1998]. `http://dx.doi.org/10.1088/0960-1317/8/2/026`.

[19] E. Verpoorte and N. F. De Rooij. 'Microfluidics meets MEMS.' *Proceedings of the IEEE*, vol. 91(6): pp. 930–953 [June 2003]. `http://dx.doi.org/10.1109/JPROC.2003.813570`.

[20] N. I. Maluf, D. A. Gee, K. E. Petersen, and G. T. A. Kovacs. 'Medical applications of MEMS.' *Proceedings of the IEEE*, (6): pp. 300–306 [November 1995]. `http://dx.doi.org/10.1109/WESCON.1995.485295`.

[21] D. B. Tuckerman and R. F. W. Pease. 'High-performance heat sinking for VLSI.' *IEEE Electron Devices Letters*, vol. 2(5): pp. 126–129 [May 1981].

[22] Dmitri V. Vezenov, Brian T. Mayers, Daniel B. Wolfe, , and George M. Whitesides. 'Integrated fluorescent light source for optofluidic applications.' *Applied Physics Letters*, vol. 86(041104) [January 2005]. `http://dx.doi.org/10.1063/1.1850610`.

[23] Elisabeth Verpoorte. 'Chip vision-optics for microchips.' *Lab Chip*, vol. 3: pp. 42N–52N [2003]. `http://dx.doi.org/10.1039/b307927a`.

[24] David J. Beebe, Glennys A. Mensing, and Glenn M. Walker. 'Physics and applications of microfluidics in Biology.' *Annual Review of Biomedical Engineering*, vol. 4: pp. 261–286 [2002]. `http://dx.doi.org/10.1146/annurev.bioeng.4.112601.125916`.

[25] P Gravesen, J Branebjerg, and O S Jensen. 'Microfluidics-a review.' *Journal of Micromechanics and Microengineering*, vol. 3: pp. 168–182 [1993]. `http://dx.doi.org/10.1088/0960-1317/3/4/002`.

[26] Paolo Dario, Maria Chiara Carrozza, Antonella Benvenuto, and Arianna Menciassi. 'Micro-systems in biomedical applications.' *Journal of Micromechanics and Microengineering*, vol. 10: p. 235244 [2000]. `http://dx.doi.org/10.1088/0960-1317/10/2/322`.

[27] Richard Barry and Dimitri Ivanov. 'Microfluidics in biotechnology.' *Sensors and Actuators B*, vol. 2(2) [March 2004]. `http://dx.doi.org/10.1186/1477-3155-2-2`.

[28] David Erickson and Dongqing Li. 'Integrated Microfluidic Devices.' *Analytica Chimica Acta*, vol. 507: pp. 11–26 [2004]. `http://dx.doi.org/10.1016/j.aca.2003.09.019`.

[29] Darwin R. Reyes, Dimitri Iossifidis, Pierre-Alain Auroux, and Andreas Manz. 'Micro Total Analysis Systems. 1. Introduction, Theory, and Technology.' *Analytical Chemistry*, vol. 74(12): pp. 2623 – 2636 [2002]. `http://dx.doi.org/10.1021/ac0202435`.

[30] Pierre-Alain Auroux, Dimitri Iossifidis, Darwin R. Reyes, and Andreas Manz. 'Micro Total Analysis Systems. 2. Analytical Standard Operations and Applications.' *Analytical Chemistry*, vol. 74(12): pp. 2637–2652 [2002]. `http://dx.doi.org/10.1021/ac020239t`.

[31] H. M. Widmer. 'Trends in industrial analytical chemistry.' *Trends in Analytical Chemistry*, vol. 2(1): pp. VIII–X [1983]. `http://dx.doi.org/10.1016/0165-9936(83)87062-9`.

[32] A. Manz, J. C. Fettinger, E. Verpoorte, H. Ludi, H. M. Widmer, and D. J. Harrison. 'Micromachining of monocrystalline silicon and glass for chemical analysis systems A look into next century's technology or just a fashionable craze?' *Trends in Analytical Chemistry*, vol. 10(5): pp. 144–149 [May 1991]. `http://dx.doi.org/10.1016/0165-9936(91)85116-9`.

[33] D. Jed Harrison, Karl Fluri, Kurt Seiler, Zhonghui Fan, Carlo S. Effenhauser, and Andreas Manz. 'Micromachining a Miniaturized Capillary Electrophoresis-Based Chemical Analysis System on a Chip.' *Science*, vol. 261(5123): pp. 895–897 [August 1993].

[34] Torsten Vilkner, Dirk Janasek, and Andreas Manz. 'Micro Total Analysis Systems. Recent Developments.' *Analytical Chemistry*, vol. 76(12): pp. 3373 – 3386 [2004]. `http://dx.doi.org/10.1021/ac040063q`.

[35] Tuan Vo-Dinh. 'Development of a DNA biochip: principle and applications.' *Sensors and Actuators B*, vol. 51(1-3): pp. 52–59 [August 1998]. `http://dx.doi.org/10.1016/S0925-4005(98)00182-8`.

[36] Alison M. Skelley, Frank J. Grunthaner, Jeffrey L. Bada, and Richard A. Mathies. 'Mars Organic Detector III: a versatile instrument for detection of bio-organic signatures on Mars.' *SPIE*, vol. 4878(12): pp. 59–67 [2003]. `http://dx.doi.org/10.1117/12.520580`.

[37] Aris Persidis. 'Biochips.' *Nature Biotechnology*, vol. 18(5397): pp. IT43–IT44 [2000]. `http://dx.doi.org/10.1038/80082`.

[38] H. John Crabtree, Michael Finot, Jennifer J. Lukomskyj, and Vicky Walker. 'Microfabrication at Micralyne: evolution of MEMS and microfluidics from exploration to commercialisation.' *Lab on a chip*, vol. 1(2): pp. 30N–40N [2001]. `http://dx.doi.org/10.1039/b110057m`.

[39] Jesus M. Ruano, Andrew Glidle, Alison Cleary, Adrian Walmsley, J. Stewart Aitchison, and Jonathan M. Cooper. 'Design and fabrication of a silica on silicon integrated optical biochip as a fluorescence microarray platform.' *Electrophoresis*, vol. 18(1-3): pp. 175–184 [March 2003]. `http://dx.doi.org/10.1016/S0956-5663(02)00170-7`.

[40] Holger Becker and Laurie E. Locascio. 'Polymer microfluidic devices.' *Electrophoresis*, vol. 56(2): pp. 267–287 [February 2002]. `http://dx.doi.org/10.1016/S0039-9140(01)00594-X`.

[41] 'Breakthrough of the year: Runners-Up, Booms in Biochips.' *Science*, vol. 282(5397): pp. 2157–2161 [1998]. `http://dx.doi.org/10.1126/science.282.5397.2157`.

[42] Inc. Fuji-Keizai USA. 'The Worldwide Biochips & Equipments Market Biochips Business Roadmap: Technology Update, Market, Business Trends and Directions.' [June 2005].

[43] Andrew E. Kamholz. 'Proliferation of microfluidics in literature and intellectual property.' *Lab on a Chip*, vol. 4(2): pp. 16N – 20N [2004]. http://dx.doi.org/10.1039/b400810n.

[44] M. Heckele, W. Bacher, and K. D. Muller. 'Hot Embossing The molding technique for plastic microstructure.' *Microsystem Technologies*, vol. 4: pp. 122–124 [1994]. http://dx.doi.org/10.1007/s005420050112.

[45] David C. Duffy, J. Cooper McDonald, Olivier J. A. Schueller, , and George M. Whitesides. 'Rapid Prototyping of Microfluidic Systems in Poly(dimethylsiloxane).' *Analytical Chemistry*, vol. 70: pp. 4974–4984 [1998]. http://dx.doi.org/10.1021/ac980656z.

[46] J. Cooper McDonald, David C. Duffy, Janelle R. Anderson, Daniel T. Chiu, Hongkai Wu, and Olivier Schueller. 'Fabrication of microfluidic systems in poly(dimethylsiloxane).' *Electrophoresis*, vol. 21(1): pp. 27–40 [2000]. http://dx.doi.org/10.1002/(SICI)1522-2683(20000101)21:1⟨27::AID-ELPS27⟩3.0.CO;2-C.

[47] Wayne F. Patton. 'A thousand points of light: The application of fluorescence detection technologies to two-dimensional gel electrophoresis and proteomics.' *Electrophoresis*, vol. 21(6): pp. 1123–1144 [April 2000]. http://dx.doi.org/10.1002/(SICI)1522-2683(20000401)21:6⟨1123::AID-ELPS1123⟩3.0.CO;2-E.

[48] Beno H. Kunst, Arjen Schots, and Antonie J. W. G. Visser. 'Detection of Flowing Fluorescent Particles in a Microcapillary Using Fluorescence Correlation Spectroscopy.' *Analytical Chemistry*, vol. 74(20): pp. 5350–5357 [2002]. http://dx.doi.org/10.1021/ac0256742.

[49] Jorg Hubner, Klaus B. Mogensen, Anders M. Jorgensen, Peter Friis, Pieter Telleman, and Jorg P. Kutter. 'Integrated Optical Measurement System for fluorescent spectroscopy in microfluidic channels.' *Review of Scientific Instruments*, vol. 72(1): pp. 229–233 [2001]. http://dx.doi.org/10.1063/1.1326929.

[50] K. E. Sapsford, Y.S. Shubin, J.B. Delehanty, J.P. Golden, C. R. Taitt, L. C. Shriver-Lake, and Ligler F.S. 'Fluorescence-based array biosensors for detection of biohazards.' *Journal of Applied Microbiology*, vol. 96(1): pp. 47–58 [January 2004]. http://dx.doi.org/10.1046/j.1365-2672.2003.02115.x.

[51] Gregor Ocvirk, Thompson Tang, and D. Jed Harrison. 'Optimization of confocal epifluorescence microscopy for microchip-based miniaturized total

analysis systems.' *Analyst*, vol. 123(7): pp. 1429–1434 [1998]. `http://dx.doi.org/10.1039/a800153g`.

[52] Evan Thrush, Ofer Levia, Wonill Ha, Ke Wang, Stephen J. Smith, and Jr. James S. Harris. 'Integrated bio-fluorescence sensor.' *Journal of Chromatography A*, vol. 21(1-2): pp. 103–110 [September 2003]. `http://dx.doi.org/10.1016/S0021-9673(03)01361-X`.

[53] E. Verpoorte, A. Manz, H. Ludi, A. E. Bruno, F. Maystre, B. Krattiger, and H. M. Widmer. 'A silicon flow cell for optical detection in miniaturized total chemical analysis systems.' *Sensors and Actuators B*, vol. 6(1-3): pp. 66–70 [January 1992]. `http://dx.doi.org/10.1016/0925-4005(92)80032-S`.

[54] Michael L. Chabinyc, Daniel T. Chiu, J. Cooper McDonald, Abraham D. Stroock, James F. Christian, Arieh M. Karger, , and George M. Whitesides. 'An Integrated Fluorescence Detection System in PDMS for microfluidic Applications.' *Analytical Chemistry*, vol. 73(8): pp. 4491–4498 [2001]. `http://dx.doi.org/10.1021/ac010423z`.

[55] Bryan G. Splawn and Fred E. Lytle. 'On-chip absorption measurements using an integrated waveguide.' *Analytical and Bioanalytical Chemistry*, vol. 373(7): pp. 519–525 [August 2002]. `http://dx.doi.org/10.1007/s00216-002-1316-9`.

[56] Klaus B. Mogensen, Henning Klank, and Jorg P. Kutter. 'Recent developments in detection for microfluidic systems.' *Electrophoresis*, vol. 25: pp. 3498–3512 [2004]. `http://dx.doi.org/10.1002/elps.200406108`.

[57] J. N. McMullin. 'Laser fabrication of integrated microfluidic/micro-optic systems.' vol. 4087, pp. 1050–1055. SPIE [2000]. `http://dx.doi.org/10.1117/12.406347`.

[58] H. Qiao, Sanket Goel, A. Grundmann, and J. N. McMullin. 'Biochips with integrated optics and fluidics.' vol. 5062, pp. 873–878. SPIE [2003]. `http://dx.doi.org/10.1117/12.514731`.

[59] H. Qiao, Sanket Goel, A. Grundmann, and J. N. McMullin. 'Fabrication of micro-optical/microfluidic biochips.' vol. 4833, pp. 54–59. SPIE [2003]. `http://dx.doi.org/10.1117/12.474893`.

[60] Hong Qiao. 'Fabrication of biochips with integrated micro-optics and microfluidics.' Master's thesis, University of Alberta, Edmonton, AB, Canada [2003].

[61] J. N. McMullin, Hong Qiao, Sanket Goel, Carolyn L Ren, and Dongqing Li. 'Integrated optical measurement of microfluid velocity.' *Journal of Micromechanics and Microengineering*, vol. 15(10): pp. 1810–1816 [2005]. `http://dx.doi.org/10.1088/0960-1317/15/10/004`.

[62] Dean Spicer. 'Multi-Layer Biochip with Integrated Hollow Waveguides.' Master's thesis, University of Alberta, Edmonton, AB, Canada [2005].

[63] Armin Grundmann. 'Detecting Fluorescent Microparticles with the Computer-Controlled Photomultiplier Tube.' Tech. rep., University of Alberta [2001].

[64] J. N. McMullin, H. Qiao, Sanket Goel, and A. Grundmann. 'Optical detection system for biochips using plastic fiber optics.' *Review of Scientific Instruments*, vol. 74(9): pp. 4145–4149 [2003]. `http://dx.doi.org/10.1063/1.1602944`.

[65] Paul C. Hiemenz and Raj Rajagopalan. *Principle of Colloid Scence and Surface Chemistry*. Marcel Dekker, Inc., New York, third edn. [1997].

[66] Carl Hansen and Stephen R Quake. 'Microfluidics in structural biology: smaller, faster better.' *Current Opinion in Structural Biology*, vol. 13(5): pp. 538–544 [2003]. `http://dx.doi.org/10.1016/j.sbi.2003.09.010`.

[67] Nam-Trung Nguyen and Steven Y. Wereley. *Fundamentals and applications of microfluifics*. Microelectromechanical Series. Artech House, Boston [2002].

[68] Dongqing Li. *Electrokinetics in Microfluidics*, vol. 2 of *Interface Science and Technology*. Elsevier Academic Press, first edn. [2004].

[69] Brian J. Kirby and Ernest F. Hasselbrink Jr. 'Zeta potential of microfluidic substrates: 1. Theory, experimental techniques, and effects on separations.' *Electrophoresis*, vol. 25(2): pp. 187–202 [2004]. `http://dx.doi.org/10.1002/elps.200305754`.

[70] Molecular Probes. `http://probes.invitrogen.com/`.

[71] Yandong Hu, Carsten Werner, and Dongqing Li. 'Influence of Three-Dimensional Roughness on Pressure-Driven Flow Through Microchannels.' *Journal of Fluids Engineering*, vol. 125(5): pp. 871–879 [2003]. `http://dx.doi.org/10.1115/1.1598993`.

[72] Qu Weilin, Gh. Mohiuddin Mala, and Li Dongqing. 'Pressure-driven water flows in trapezoidal silicon microchannels.' *International Journal of Heat and Mass Transfer*, vol. 43(3): pp. 353–364 [2002]. `http://dx.doi.org/10.1016/S0017-9310(99)00148-9`.

[73] David Erickson, David Sinton, and Dongqing Li. 'Joule heating and heat transfer in poly(dimethylsiloxane) microfluidic systems.' *Lab on a Chip*, vol. 3(3): pp. 141–149 [2003]. `http://dx.doi.org/10.1039/b306158b`.

[74] David Sinton and Dongqing Li. 'Electroosmotic velocity profiles in microchannels.' *Colloids and Surfaces A*, vol. 222(1-3): pp. 273–283 [July 2003]. `http://dx.doi.org/10.1016/S0927-7757(03)00233-4`.

[75] Eugene Hecht. *Optics*. Addison Wesley Publishing Company, third edn. [1997].

[76] H. Kogelnik. 'An Introduction to Integrated Optics.' *IEEE Transactions on Microwave Theory and Techniques*, vol. 23(1): pp. 2–16 [January 1975].

[77] Bhaa E. A. Saleh and Malvin C. Teich. *Fundamentals of Photonics*. John Wiley & Sons, Inc. [1991].

[78] Gerd Keiser. *Optical Fiber Communications*. The McGraw-Hill Companies, third edn. [1999].

[79] Che-Hsin Lin, Gwo-Bin Lee, Bao-Wen Chang, and Guan-Liang Chang. 'A new fabrication process for ultra-thick microfluidic microstructures utilizing SU-8 photoresist.' *Journal of Micromechanics and Microengineering*, vol. 12: pp. 590–597 [January 2002]. `http://dx.doi.org/10.1088/0960-1317/12/5/312`.

[80] J. N. McMullin, H. Qiao, Sanket Goel, S. A. McColman, and A. Grundmann. 'Lab-on-a-chip optical detection system using plastic fiber optics.' *Applications of Photonic Technology 6*, vol. 5260(1): pp. 114–118 [2003]. `http://dx.doi.org/10.1117/12.543333`.

[81] Klaus B. Mogensen, Nickolaj J. Petersen, Jorg Hubner, and Jorg P. Kutter. 'Monolithic integration of optical waveguides for absorbance detection in microfabricated electrophoresis devices.' *Electrophoresis*, vol. 22(18): pp. 3930–3938 [October 2001]. `http://dx.doi.org/10.1002/1522-2683(200110)22:18<3930::AID-ELPS3930>3.0.CO;2-Q`.

[82] Ewan H Conradie and David F Moore. 'SU-8 thick photoresist processing as a functional material for MEMS applications.' *Journal of Micromechanics and Microenginering*, vol. 12: pp. 368–374 [2002]. `http://dx.doi.org/10.1088/0960-1317/12/4/303`.

[83] H. Lorenz, M Despont, N Fahrni, N LaBianca, P Renaud, and P Vettiger. 'SU-8: a low-cost negative resist for MEMS.' *Journal of Micromechanics and Microengineering*, vol. 7: pp. 121–124 [September 1997]. `http://dx.doi.org/10.1088/0960-1317/7/3/010`.

[84] S. C. Terry, J. H. Jerman, and J. B. Angell. 'A gas chromatographic air analyzer fabricated on a silicon wafer.' *IEEE Transactions on Electron Devices*, vol. 26(12): pp. 1880–1886 [December 1979].

[85] K. E. Petersen. 'Fabrication of an integrated, planar silicon ink-jet structure.' *IEEE Transactions on Electron Devices*, vol. 26(12): pp. 1918–1920 [December 1979].

[86] Carlo S. Effenhauser, Andreas Manz, and H. Michael Widmer. 'Glass chips for high-speed capillary electrophoresis separations with submicrometer plate heights.'

Analytical Chemistry, vol. 65(19): pp. 2637–2642 [1993]. `http://dx.doi.org/10.1021/ac00067a015`.

[87] Stephen C. Jacobson, Alvin W. Moore, and J. Michael Ramsey. 'Fused Quartz Substrates for Microchip Electrophoresis.' *Analytical Chemistry*, vol. 67(13): pp. 2059–2063 [1995]. `http://dx.doi.org/10.1021/ac00109a026`.

[88] Stephen C. Jacobson and J. Michael Ramsey. 'Microchip electrophoresis with sample stacking.' *Electrophoresis*, vol. 16(1): pp. 481–486 [December 2005]. `http://dx.doi.org/10.1002/elps.1150160179`.

[89] Peter Friis, Karsten Hoppe, Otto Leistiko, Klaus Bo Mogensen, rg bner, and rg P. Kutter. 'Monolithic integration of microfluidic channels and optical waveguides in silica on silicon.' *Applied Optics*, vol. 40(34): pp. 6246–6251 [2001]. `http://ao.osa.org/abstract.cfm?id=66787`.

[90] Stephen R Quake and Axel Scherer. 'From micro- to nanofabrication with soft materials.' *Angewandte Chemie International Edition*, vol. 290(5496): pp. 5796–5799 [2000]. `http://dx.doi.org/10.1126/science.290.5496.1536`.

[91] P. M. Martin, D. W. Matson, W. D. Bennett, Y. Lin, and D. J. Hammerstrom. 'Laminated plastic microfluidic components for biological and chemical analysis.' *Journal of Vacuum Science and Technology A*, vol. 17(4): pp. 2264–2269 [1999]. `http://dx.doi.org/10.1116/1.581758`.

[92] Jong Soo Ko, Hyun C. Yoon, Haesik Yang, Hyeon-Bong Pyo, Kwang Hyo Chung, Sung Jin Kim, and Youn Tae Kim. 'A polymer-based microfluidic device for immunosensing biochips.' *Lab on a chip*, vol. 3: pp. 106–113 [2003]. `http://dx.doi.org/10.1039/b301794j`.

[93] Norland Products. `http://www.norlandprod.com/`.

[94] Younan Xia and George M. Whitesides. 'Soft Lithography.' *Angewandte Chemie*, vol. 37: pp. 550–575 [1998]. `http://dx.doi.org/10.1002/(SICI)1521-3773(19980316)37:5<550::AID-ANIE550>3.0.CO;2-G`.

[95] Jason P. Rolland, Erik C. Hagberg, Ginger M. Denison, Kenneth R. Carter, and Joseph M. De Simone. 'High-Resolution Soft Lithography: Enabling Materials for Nanotechnologies.' *Angewandte Chemie International Edition*, vol. 43(43): pp. 5796–5799 [2004]. `http://dx.doi.org/10.1002/anie.200461122`.

[96] M. Unger, H. Chou, T. Thorsen, A. Scherer, and S. Quake. 'Monolithic microfabricated valves and pumps by multilayer soft lithography.' *Science*, vol. 288: p. 113116 [2000]. `http://dx.doi.org/10.1126/science.288.5463.113`.

[97] Samuel K. Sia and George M. Whitesides. 'Microfluidic devices fabricated in poly(dimethylsiloxane) for biological studies.' *Electrophoresis*, vol. 24: p. 35633576 [2003]. `http://dx.doi.org/10.1002/elps.200305584`.

[98] K. B. Albaugh, P. E. Cade, and D. H. Rasmussen. 'Mechanisms of anodic bonding of silicon to pyrex glass.' vol. 4, p. 109110 [1988]. `http://dx.doi.org/10.1109/SOLSEN.1988.26450`.

[99] MicroChem Corp., Newton, MA. *Nano^{TM}SU-8 2000 Mannual* [2004]. `http://www.microchem.com/`.

[100] J. M. Shaw, J. D. Gelorme, N. C. LaBianca, W. E. Conley, and S. J. Holmes. 'Negative photoresists for optical lithography.' *IBM Journal of Research and Development*, vol. 41(1/2): pp. 81–94 [1997].

[101] Joshua B. Edel, Elisabeth K. Hill, and Andrew J. de Mello. 'Velocity measurement of particulate flow in microfluidic channels using single point confocal fluorescence detection.' *Analyst*, vol. 11: p. 19531957 [2001]. `http://dx.doi.org/10.1039/b106559a`.

[102] Shankar Devasenathipathy, Juan G. Santiago, and Kohsei Takehara. 'Particle Tracking Techniques for Electrokinetic Microchannel Flows.' *Analytical Chemistry*, vol. 74(15): pp. 3704–3713 [2002]. `http://dx.doi.org/10.1021/ac011243s`.

[103] Zhongping Chen, Thomas E. Milner, Digant Dave, and J. Stuart Nelson. 'Optical Doppler tomographic imaging of fluid flow velocity in highly scattering media.' *Optics Letters*, vol. 22(1): pp. 64–67 [1997]. `http://ol.osa.org/abstract.cfm?id=35907`.

[104] J. G. Santiago, S. T. Wereley, C. D. Meinhart, D. J. Beebe, and R. J. Adrian. 'A particle image velocimetry system for microfluidics.' *Experiments in Fluids*, vol. 25: p. 316319 [1998]. `http://dx.doi.org/10.1007/s003480050235`.

[105] Yien C. Kwok, Nicholas T. Jeffery, and Andreas Manz. 'Velocity Measurement of Particles Flowing in a Microfluidic Chip Using Shah Convolution Fourier Transform Detection.' *Analytical Chemistry*, vol. 73: pp. 1748–1753 [2001]. `http://dx.doi.org/10.1021/ac0013047`.

[106] David Sinton, Carlos Escobedo-Canseco, Liqing Ren, and Dongqing Li. 'Direct and Indirect Electroosmotic Flow Velocity Measurements in Microchannels.' *Journal of Colloid and Interface Science*, vol. 254(1): pp. 6246–6251 [2002]. `http://dx.doi.org/doi:10.1006/jcis.2002.8584`.

[107] Fred E. Lytle and Bryan G. Splawn. 'Performance of sumillimeter square hollow waveguide.' *Applied Optics*, vol. 31(5): pp. 6660–6665 [2002]. `http://ao.osa.org/abstract.cfm?id=70357`.

[108] S. K. Sampath, L. St. Clair, Wu Xingtao, D. V. Ivanov, Q. Wang, C. Ghosh, and K. R. Farmer. 'Rapid MEMS prototyping using SU-8, wafer bonding and deep reactive ion etching.' *Proceedings of IEEE*, vol. 2001: pp. 158–161 [June 2001]. http://dx.doi.org/10.1109/UGIM.2001.960320.

[109] Philip D Curtis, Stavros Iezekiel, Robert E Miles, and Christopher R Pescod. 'SU-8 as a material for the integrated all-optical microwave filters.' *Microwave Engineering*, vol. 103(1-2): pp. 165–170 [August 2001]. http://img.cmpnet.com/edtn/europe/mwee/pdf/Curtis.pdf.

[110] Lin Pang, Wataru Nakagawa, and Yeshaiahu Fainman. 'Fabrication of optical structures using SU-8 photoresist and chemically assisted ion beam etching.' *Optical Engineering*, vol. 42(10): p. 29122917 [2003]. http://dx.doi.org/10.1117/1.1604399.

[111] J. El-Ali, K.B. Mogensen, I.R.P Nielsen, J.P. Kutter, P. Telleman, and A. Wolff. 'Integration of polymer waveguides for optical detection in biochemical microsystems.' *Proceedings of the Micro total analysis system, 2002*, pp. 260–262 [2002].

[112] K. B. Mogensen, A. Wolff J. El-Ali, and J. P. Kutter. 'Integration of polymer waveguide for optical detection in microfabricated chamical analysis system.' *Applied Optics*, vol. 42(19): pp. 4072–4079 [2003]. http://ao.osa.org/abstract.cfm?id=72841.

[113] Gwo-Bin Lee, Che-Hsin Lin, and Guan-Liang Chang. 'Micro flow cytometers with buried SU-8/SOG optical waveguides.' *Sensors and Actuators A*, vol. 103(1-2): pp. 165–170 [January 2003]. http://dx.doi.org/10.1016/S0924-4247(02)00305-9.

[114] J. M. Ruano, M. Aguirregabiria, M. Tijero, M. Arroyo, J. Garcia, J. Berganzo, I. Aramburu, F. J. Blanco, and K. Mayora. 'Monolithic integration of microfluidic channels and optical waveguides using a photodefinable epoxy.' *Proceedings of IEEE*, vol. 2004: pp. 121–124 [2004]. http://dx.doi.org/10.1109/MEMS.2004.1290537.

[115] J. N. McMullin. 'Propagating beam method simulation of planar multimode optical waveguides.' vol. 1389, pp. 621–629. SPIE [1991]. http://dx.doi.org/10.1117/12.25563.

[116] M. D. Feit and Jr. Fleck J. A. 'Light propagation in graded-index optical fibers.' *Applied Optics*, vol. 17(24): pp. 3990–3998 [1978]. http://www.opticsinfobase.org/abstract.cfm?URI=ao-17-24-3990.

[117] Tiina Sikanen, Santeri Tuomikoski, Raimo A. Ketola, Risto Kostiainen, Sami Franssilab, and Tapio Kotiaho. 'Characterization of SU-8 for electrokinetic

microfluidic applications.' *Lab on a chip*, vol. 5: pp. 888–896 [2005]. http://dx.doi.org/10.1039/b503016a.

[118] B Bilenberg, T Nielsen, B Clausen, and A Kristensen. 'PMMA to SU-8 bonding for polymer based lab-on-a-chip systems with integrated optics.' *Journal of Micromechanics and Microengineering*, vol. 14: pp. 814–818 [April 2004]. http://dx.doi.org/10.1088/0960-1317/14/6/008.

[119] J.M. Ruano-Lopez, M. Aguirregabiria, M. Tijero, M.T. Arroyo, J. Elizalde, J. Berganzo, I. Aranburu, F.J. Blanco, and K. Mayora. 'A new SU-8 process to integrate buried waveguides and sealed microchannels for a Lab-on-a-Chip.' *Sensors and Actuators B* [article in press]. http://dx.doi.org/10.1016/j.snb.2005.05.011.

Appendix A

Material Properties

Some of the material properties which are useful to know in the present work are, the index of refraction, the glass transition temperature, coefficient of thermal expansion and the capability to support the electroosmotic flow (EOF). The properties are summarized in Table A.1.

Refractive Index

The value of the index of refraction of a material gives an idea weather a material can be used as a waveguiding material on a substrate (Section 2.2.1). For example, SU-8 can be used as a waveguiding material on a glass because it has a higher index than glass.

Glass Transition Temperature

The glass transition temperature is a temperature at which the behavior of a material changes from elastic to brittle. Fused silica, with a very high glass transition temperature, makes it difficult to mould into simple polymers. Materials with low glass transition temperatures, such as PMMA are used for hot embossing. A very low T_g of PDMS allows it to have exceptional mobility and orientation.

Coefficient of Thermal Expansion

The coefficient of thermal expansion measures the shrinkage when cooling down a material. When a material of a coefficient of thermal expansion, C, cools down from a high temperature, T_1, to a low temperature, T_2, its shrinkage is C(T1 - T2). For example, the thermal expansion coefficient of PDMS is much higher than that of silicon. Therefore, during the cooling process, they tend to shrink by different rates. Due to their different shrinking degrees, when PDMS and silicon cool down together, the PDMS may stretch the silicon while the silicon may compress the PDMS.

Support to Electroosmotic Flow

To support electroosmotic flow, a material should carry surface charges when in contact with an aqueous solution. The glass is a very good material to support EOF because its surface becomes negatively charged when in contact with water. By oxidizing a PDMS layer in plasma, the surface is negatively charged and supports EOF. SU-8 can support EOF by modifying the surface of the SU-8 microchannel walls [117].

Table A.1: Properties of different materials used in the present work

Material	**Refractive Index (n)**	**Glass transition temperature T_g (^{o}C)**	**Coefficient of thermal expansion C (/^{o}C)**	**Possibility of EOF**
Soda lime glass	1.51	300	8.4×10^{-5}	Yes
Silicon	3.42	1300	2.7×10^{-6}	No
PMMA	1.49	105	6.0×10^{-5}	No
PDMS	1.40	-120	3.1×10^{-4}	Yes
NOA 63	1.56	120	1.6×10^{-4}	No
SU-8	1.59	50	5.2×10^{-5}	Yes

Appendix B

Procedure for Fabricating Master by Lithography (Positive photoresist)

The overall fabrication process for fabricating masters on silicon was carried out at NanoFab, University of Alberta. The first step to fabricate a silicon master by lithography is to make a mask that can be used to fabricate masters in silica/glass. Different microchannel patterns are designed in LEdit (Figure B.1 (a)) in order to study the flow in microchannels with various dimensions and shapes.

Later, the design is exported to the pattern generator, which transformed this design to a glass substrate, by a laser writing process. After this, the mask is developed on positive quartz and a chromium layer is patterned. The final mask is shown in Figure B.1 (b). The soft lithography process to make master is shown schematically in Figure B.

After generating the photomask the following process is used to fabricate masters as shown in Figure B:

1. Wafer Cleaning

   Silicon wafers with thickness of 500 μm are pre-cleaned with Piranha solution $H_2O_2 : H_2SO_4$=1:3.

2. Thermal Oxidation of Silicon-dioxide

   Silicon wafers are then oxidized at high temperatures (1050^oC) for 6 hours to get the oxide thickness of 0.6 μ. The process of oxidation and diffusion are achieved in the Mini-Brute furnace.

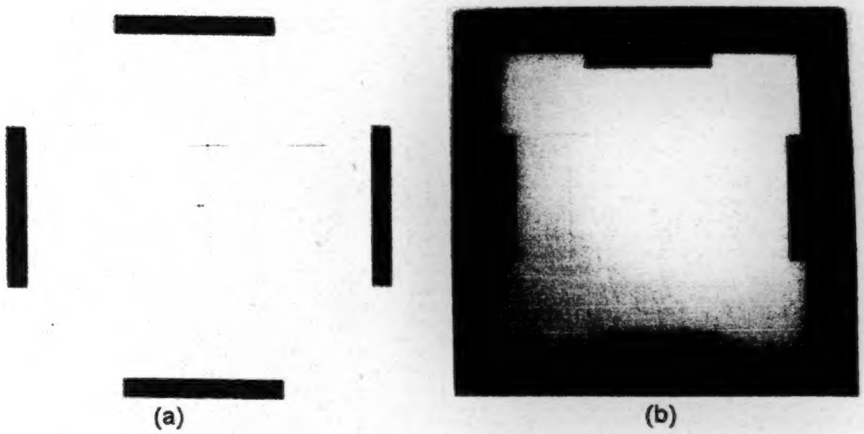

Figure B.1: *(a) LEdit design to make the mask, and (b) actual mask after developing.*

The wafers are placed in quartz boats which are supported by fused silica paddles inside the process tube. The oxidizing steam then enters the process tube through its source end, subsequently diffusing to the wafers where the oxidation occurs.

3. HMDS Treatment

   To improve the adhesion of photoresist, the silicon wafer is treated with HMDS (YES oven) for 17 minutes.

4. Spin-coat photoresist HPR 504

   The spreading of for 10 seconds at 500 rpm and spinning for 40 seconds at 4000 rpm gives a thickness of 1.5 μm.

5. Soft Bake

   The softbake is done to drive off any remaining solvent thus setting up the resist for exposure. This is done on a Solinet vacuum hotplate at 115°C for 90 seconds. Wafer should be cooled down to room temperature prior to exposure.

6. UV Exposure

The wafer should be aligned on mask aligner (AB-M Inc., San Jose, CA). The wafer is exposed using the 365 nm UV source at a power of 21 mW/cm^2 for 4 seconds.

7. Develop Photoresist

   The photoresist is developed by immersing the wafer in MicroDeposit 354 for 25 seconds. This is immediately followed by a DI water rinse.

8. Buffered Oxide Etching (BOE)

   A standard NanoFab protocol is used to etch away the unexposed oxide with an etch rate of 550 Å/min, BOE is carried out for 10 minutes to etch away 0.6 μm.

9. ICPRIE

   Plasma etching is very useful to achieve vertical side walls. It can even etch some materials, like SiN, that are difficult to etch using chemical etching. The drawback, however, comes from the fact that for an element to be etchable using plasma chemistry, the reaction by products must be a volatile gas, such as fluorine, bromine or chlorine.

   The ICPRIE system consists of an inductively coupled plasma (ICP) source and reactive-ion etching (RIE) source. ICP source produces many more ions and radicals which are generated by electrons accelerated in magnetic field compared to a simple capacitive plasma source.

   The primary technology is based on "Bosch process" where two different gas compositions are alternated in the reactor. The first gas composition creates a polymer on the surface of the substrate, and the second gas composition etches the substrate. The second gas uses two steps - SF_6 etches Si isotropically, a polymer (C_4F_8) anisotropically in these two steps. One complete step takes about 1 minute with etch rate of 1 μm/cycle. The process can be repeated until the desired depth is achieved and can easily be used to etch completely through a silicon substrate. So, this process is repeated for 50 cycles. The depth of the silicon was inspected by using contact profilometer after every 10 cycles.

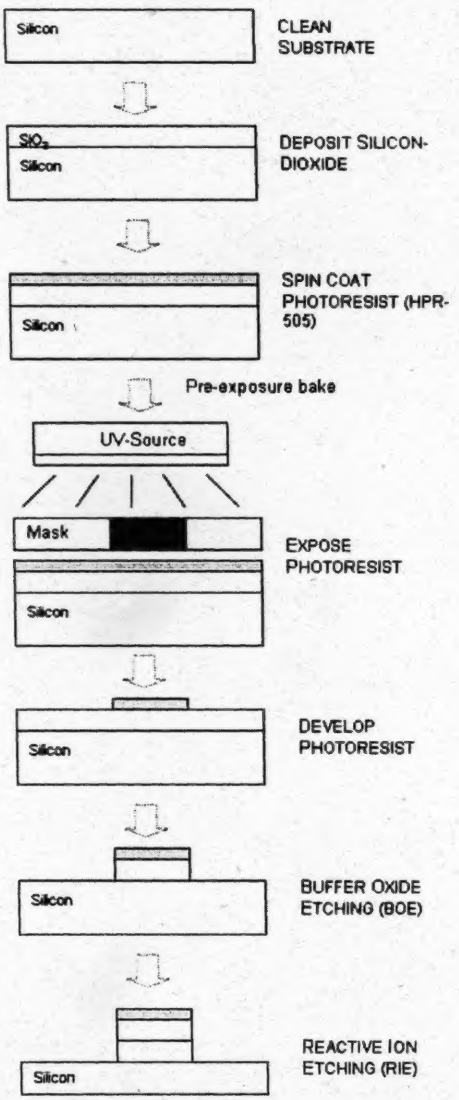
Silicon
CLEAN SUBSTRATE
SiO$_2$
Silicon
DEPOSIT SILICON-DIOXIDE
Silicon
SPIN COAT PHOTORESIST (HPR-505)
Pre-exposure bake
UV-Source
Mask
Silicon
EXPOSE PHOTORESIST
Silicon
DEVELOP PHOTORESIST
Silicon
BUFFER OXIDE ETCHING (BOE)
Silicon
REACTIVE ION ETCHING (RIE)

Figure B.2: *Process steps for fabricating silicon master with positive photoresist and deep reactive-ion etching.*

Appendix C

PDMS Casting and Bonding

PDMS Casting and Baking

- A silicon wafer (4 inch diameter from Corning) is pre-cleaned with Piranha solution $H_2O_2 : H_2SO_4$=1:3. This is followed by DI water rinse. Wafer should be completely dried (specs).
- To improve the chances of peeling off the cured PDMS, the silicon wafer is treated with HMDS.
- To achieve a PDMS layer of 2 mm, 11 grams of PDMS solution is needed when cast over a 4 - inch wafer placed in the NanoFab PDMS apparatus ("jig"). This jig has a rubber o-ring and upper plate to tighten the wafer between the bottom plate and the o-ring. For this, 10 grams of base agent and 1 gram of curing agent are mixed together.
- PDMS is degassed in the vacuum oven at room temperature until the bubbles are removed (30 minutes).
- Then, the silicon wafer is placed in the NanoFab PDMS jig and tightened. Next, PDMS solution is poured over the wafer.
- The the jig and wafer are placed in the vacuum oven at 80°C for 2 hours under a vacuum of 10 inches of Hg.

- After removing out the jig from the oven, the wafer with PDMS is removed and cooled down to room temperature. The PDMS layer is peeled off from the wafer and blue tape is applied to both sides of the PDMS and the side in contact with the wafer is marked.

Hole Punching

- The PDMS layer with blue tape is cut into a piece fit on the chip.
- Using the chip as a guide, holes for the reservoirs are made with a 1.5 mm punch.

Bonding with the SU-8 Chip

A reactive ion etcher is used to bond the PDMS and on glass with SU-8.

Cleaning the Chamber

- Vent the RIE chamber to check if it is empty.
- Close the chamber and apply high vacuum.
- Apply 80 % of O_2, 150 mTorr of pressure and 75 % of RF for 10 minutes.
- Vent the chamber.

RIE the PDMS and Wafer

- Place the wafers and PDMS pieces. PDMS piece should be placed after removing the blue tape from the top side (the side facing Si wafer while casting PDMS). The top side should face up.
- Close the chamber and apply high vacuum.
- Apply 25 % of O_2, 200 mTorr of pressure and 33.3 % of RF for 30 seconds.
- Vent the chamber.

Bonding

- Place the PDMS piece on a flat and clean surface in the same way it is placed in the RIE chamber.
- Place the glass wafer on top of the PDMS piece with the SU-8 facing the PDMS. The reservoirs should align with the holes in the PDMS.
- Apply some pressure by hand.

Appendix D

Procedure for Fabricating Biochips by Lithography (SU-8, Negative Photoresist)

As outlined in Section 3.2.4, the overall fabrication process for fabricating optobiochip on glass is described in this appendix. The whole process was carried out at the NanoFab, University of Alberta. After generating the photomask, the following process is used to fabricate masters as shown in figure D.1 [99]:

1. Wafer Cleaning

   The glass substrate must be properly cleaned in hot piranha to remove organic residues from the substrate. A glass microscope slide from corning (3 X 4 $inch^2$) is pre-cleaned with Piranha solution $H_2O_2 : H_2SO_4$=1:3. This is followed by DI water rinse. The wafer should be completely dried. It should be ensured that the moisture does not remain on the substrate while drying it.

2. Wafer Dehydration

   Prior to use of this wafer, it is dehydrated on a contact hot plate at 200°C for 5 minutes and brought down to room temperature after removing it from the hot plate.

3. Spin-coat Photoresist

   SU-8 2050 (MicroChem Corp., Newton, MA) produces low defect coating over a very broad range of film thickness. The spin speed should be adjusted to achieve a

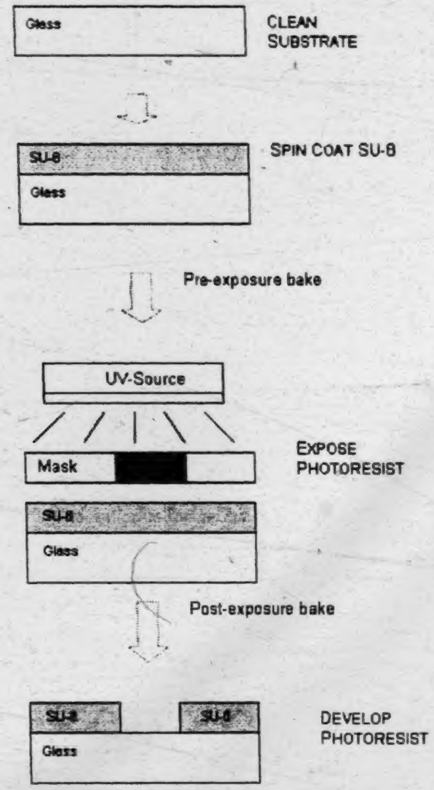
Glass
CLEAN SUBSTRATE
SU-8
Glass
SPIN COAT SU-8
Pre-exposure bake
UV-Source
Mask
EXPOSE PHOTORESIST
SU-8
Glass
Post-exposure bake
SU-8
SU-8
Glass
DEVELOP PHOTORESIST

Figure D.1: *Process steps involved to fabricate opto-biochips with SU-8.*

thickness of 50 μm. SU-8 should be dispensed so as to make sure that the complete wafer is covered before spinning. The dispensing might produce some bubbles, so we should wait for 5 minutes before starting spinning. First the resist should be spread on a low speed to allow the resist to cover the entire surface, then the final spin cycle should start at desired speed. First, the SU-8 is ramped to 500 rpm at 100 rpm/second acceleration. This is maintained for 5 seconds. Then, it is ramped to final spin speed of 3000 rpm with an acceleration of 300 rpm/second. The spn cycle should be maintained for 30 seconds.

4. Pre-exposure Bake

The wafer is soft baked to evaporate the solvent and densify the film. The glass transition temperature T_g of unexposed SU-8 is approximately 50°C. So it should be heated on a higher temperature for solvent evaporation. The wafer is soft baked on a hot plate by ramping and stepping the hot plate temperature.

First, the wafer with resist is kept on the center of the hot plate at 65°C for 3 minutes. Then, keeping the wafer on hot plate, the temperature is ramped to 95°C (2 minutes) and hold for 6 minutes. Ramping or stepping the soft bake temperature is done to get better results. The solvent evaporates out of the film at a more controlled rate at lower initial bake temperatures, which results in better coating results, reduced edge bead and better resist-to-substrate adhesion.

5. UV Exposure

Exposing is a very important step in SU-8 processing. SU-8 is virtually transparent and insensitive above 400nm but has high absorption below 350nm. Excessive dose below 350nm results in over exposure of the top portion of the resist film, resulting in exaggerated negative sidewall profiles. The optimal exposure dose is proportional to the film thickness and depends on process parameters.

The wafer with SU-8 is aligned on a mask aligner (AB-M Inc., San Jose, CA). As the size of the wafer is such as to fit either designs A and B or designs C and D, care should be taken to make sure that one set of layouts lies within the boundary of the wafer. The wafer is exposed using 365 nm UV source with optimal power of 21 mW/cm^2. The total UV is turned on for 20 seconds to provide a required dose 420 mJ/cm^2. When SU-8 is exposed to UV light, strong acid is formed during the exposure process.

6. Post-exposure Bake

To get cross-linking of the unexpose part of SU-8, post-exposure baking (PEB) step is required. As discussed above, T_g of unexposed SU-8 is approximately 50°C. T_g value of SU-8 begins to grow rapidly with the increase of the number of crosslinks thus dramatically decreasing the acid diffusion rate. For fully crosslinked SU-8 T_g exceeds 200°C.

2

The post exposure bake is also performed ramping and stepping the hot plate temperature. First, the wafer with resist is kept on the hot plate at 65°C for 1 minute. Then, keeping the wafer on hot plate, the temperature is ramped to 95°C (2 minutes) and hold for 4 minutes. To minimize resist stress, wafer bowing and resist cracking, a slow ramp contact hot plate process is used.

7. Develop Photoresist

After the post-exposure bake, the SU-8 coated wafer is placed in SU-8 developer (from MicroChem) to remove any unexposed SU-8. Other solvent based developers such as ethyl lactate and diacetone alcohol may also be used. Developing time depends on agitation rate, temperature and resist processing parameters, so based on our method of agitation a develop time is chosen.

Two beakers are taken and one of them is filled with the SU-8 developer (MicroChem Corp., Newton, MA) and IPA so that one wafer can be immersed into the beaker. The wafer is immersed in the Developer by holding it with plastic clips and some agitation is applied to the wafer. For high aspect ratio and/or thick films, the substrate is strongly agitated. A white film on the substrate indicate that the substrate needs to be developed for more time. The wafer is rinsed in IPA solution and inspected under microscope first after 2 minutes and then for every 1 minute. If a white film is produced while rinsing the wafer with IPA, it means that the wafer has been underdeveloped. The process develop time is 4-5 minutes which depends widely as a function of agitation rate.

8. Wafer Inspection

To make sure that the SU-8 on the wafer is completely developed, the wafer is inspected under microscope and measure the thickness of the resist by contact profilometer.

9. PDMS Bonding

The PDMS curing and bonding steps are shown in Appendix C.

5